# ENGINEERING THE BANDGAP, FERMI LEVEL, ELECTRONIC AND MAGNETIC PROPERTIES OF TRANSPARENT CONDUCTING OXIDES

YONGLIANG ZHAO

NATIONAL UNIVERSITY OF SINGAPORE
2013

# ENGINEERING THE BANDGAP, FERMI LEVEL, ELECTRONIC AND MAGNETIC PROPERTIES OF TRANSPARENT CONDUCTING OXIDES

**YONGLIANG ZHAO**
**(*B.Sc*, NATIONAL UNIVERSITY OF SINGAPORE, SINGAPORE)**

**A THESIS SUBMITTED**

**TO THE DEPARTMENT OF PHYSICS**
**NATIONAL UNIVERSITY OF SINGAPORE**
**IN PARTIAL FULFILMENT FOR THE**
**DEGREE OF DOCTOR OF PHILOSOPHY IN SCIENCE**

**2013**

**DECLARATION**

I hereby declare that the thesis is my original work and it has been written by me in its entirety. I have duly acknowledged all the sources of information which have been used in the thesis.

This thesis has also not been submitted for a degree in any university previously.

Yongliang Zhao

10 Nov 2013

## ACKNOWLEDGEMENTS

The past four years have seen extreme events, rare economic crisis sweeping the world, people fighting for their freedom, lives, democracy, honors, jobs, etc. in virtually all parts of the globe. I consider myself to be very lucky and feel blessed for acquiring a Ph.D. education in NUSNNI-NanoCore, NUS during these turbulent times. I am grateful to a lot of people who have given me their selfless help, not only in actions, but also intellectually.

I have to first give my acknowledgment to my advisor, Prof. T. Venkatesan. Venky, who taught and influenced me both in research skills and my own attitude to life. I still remember my first meeting with Venky in his office. Since then, his knowledgeable, conversant and scholarly image had formed a deep impression in my mind. He never pushed me, but his enthusiasm for research always had a strong effect on me. When I made big mistakes, he criticized me severely but always gave me a chance to mend my ways. The knowledge and experience that he imparted to me in research and career will forever be supporting my pursuit of my goal. His edification and expectations will encourage me to work harder and smarter. Next I want to thank my co-advisor, Dr. Qing Wang, for his patient guidance and helpful suggestions. I spent a whole year in his lab, learning about solar cells, planning experiments under his help. Without him, I could not have become so interested in solar energy conversions, which will be the main task in my post doctor studies, and possibly in the next few years.

I should specially thank Dr. Jams Robert Jennings, Dr. Weiming Lǚ, Dr. Zhen Huang, and Dr. Sankar Dhar, for their patient listening and they never rejected any discussions or giving me assistance.

I want to thank Dr. Ariando, Dr. A. Rusydi, Dr. Haibin Su, Dr. K. Gopinadhan, Dr. S. Saha, Dr. Dongchen Qi, Dr. Hongwei Ou, and Dr. Guangwu Yang. Their tremendous help with experiments have been of great value to me.

Shengwei Zeng, Zhiqi Liu, Jianqiang Chen, Changjian Li, Feng Li, Qizhao Huang and Yeru Liu, thank you all not only for the cooperation in experiments but also for your impressive jokes.

Mallikarjunarao Motapothula, Amar Srivastava, Anil Annadi, Dr. Arkajit Roy Barman, and Tarapada Sarkar, I am really honored to be colleagues of all these

wonderful and talented guys.
I particularly need to thank Jingjing Li for his encouragement when I was at the lowest point in my life. Also, I enjoyed my life with my roommates Ling Feng, Niantao Deng and Bo Qiu. Of course, there are many more people who helped me although I cannot list them all here. I take this opportunity to thank them all and wish them happy lives.
Finally and most importantly, I want to express my love and gratitude to my wife Suzhen Zhang, my parents and sisters. Thank you for thinking of me always. Your heads and hearts are always behind me and supporting me. You are more important than my life.

## TABLE OF CONTENTS

**DECLARATION** .......... i

**ACKNOWLEDGEMENTS** .......... ii

**TABLE OF CONTENTS** .......... iv

**ABSTRACT** .......... vii

**LIST OF PUBLICATIONS** .......... ix

**LIST OF FIGURES** .......... xi

**LIST OF SYMBOLS** .......... xvii

**Chapter 1 Introduction** .......... 1

1.1 Motivation and scope of the thesis .......... 1

1.2 Brief introduction of concept of energy bandgap .......... 3

1.3 Fundamental physical and chemical properties of $TiO_2$ .......... 5

1.3.1 Crystal structures .......... 5

1.3.2 Electronic structures .......... 7

1.4 Typical applications of $TiO_2$ .......... 7

1.4.1 Transparent Conducting Oxides (TCOs) .......... 8

1.4.2 Dye Sensitized Solar Cell (DSC) and water splitting .......... 8

1.4.3 Other applications .......... 11

**Chapter 2 Basic sample preparation and characterization methods** .......... 12

2.1 Sample preparation technique: Pulsed Laser Deposition .......... 12

2.2 Structure characterization techniques .......... 13

2.2.1 X-ray diffraction .......... 13

2.2.2 Rutherford Backscattering Spectrometry and Ion Channeling .......... 14

2.2.3 Transmission Electron Microscopy & Energy-dispersive X-ray spectroscopy .......... 16

2.3 Optical bandgap and flat band potential study techniques .......... 18

2.3.1 Ultraviolet-visible Spectroscopy .......... 18

2.3.2 Electrochemical Impedance Spectroscopy .......... 18

2.4 Transport properties study technique: Physical Property Measurement System .......... 19

2.5 Magnetism and impurity characterization techniques .......... 21

2.5.1 Superconducting Quantum Interference Device-Vibrating Sample magnetometers .......... 21

2.5.2 Secondary Ion Mass Spectroscopy .......... 23

2.5.3 X-ray Absorption Spectroscopy .......... 24

**Chapter 3 Unexpected variable range hopping (VRH) mechanism observed in pure anatase $TiO_2$ thin film** .......... 25

3.1 Development of VRH theory........25
3.1.1 Mott VRH........25
3.1.2 Efros-Shklovskii (ES) VRH........26
3.2 Sample preparation and characterization........26
3.3 Transport properties and magneto-resistance (MR) studies........27
3.3.1 Theoretical mobility and MR in the range of VRH conduction........27
3.3.2 Experimental results........29
3.4 Summary........35
**Chapter 4 Tailoring the bandgap of anatase $TiO_2$ by cationic dopant Ta and study of the shift of flat band potential by applying Mott-Schottky equation........36**
4.1 Blue shift of optical bandgap of $TiO_2$........36
4.2 Mott-Schottky equation........37
4.3 Experimental section........39
4.4 Experimental results and discussion........41
4.5 Theoretical calculation results........50
4.6 Summary........54
**Chapter 5 Insulator to metal transition of anatase $TiO_2$ thin film upon low concentration of Ta doping........55**
5.1 Insulator to metal transition........55
5.2 Kondo effect........55
5.3 Weak localization........58
5.4 Experimental results........60
5.5 Summary........66
**Chapter 6 Nickel impurity mediated reversible ferromagnetism of rutile $TiO_2$ substrate upon annealing........68**
6.1 Introduction to oxide based Dilute Magnetic Semiconductors........68
6.1.1 Types of magnetism........68
6.1.2 Dilute Magnetic Semiconductors........71
6.2 Background of the experiment........72
6.3 Experimental details........73
6.4 Results and discussions........75
6.5 Summary........83
**Chapter 7 Structural, electronic and optical properties of transparent conducting $SrNbO_3$ thin films........84**
7.1 Introduction of the material........84
7.2 Experimental section........86

7.3 Results and discussions ........ 86
7.4 Summary ........ 94

**Chapter 8 Summary and outlook ........ 96**

8.1 Summary ........ 96
8.1.1Transport properties of anatase $TiO_2$ thin film ........ 96
8.1.2 Ferromagnetism of rutile $TiO_2$ substrate induced by Nickel impurity ........ 97
8.1.3 Structural, transport and optical properties of $SrNbO_3$ ........ 97
8.2 Outlook ........ 97

**BIBLIOGRAPHY ........ 99**

**Appendices ........ 111**

Appendix 1 Derivation of equation (3.7) from equation (3.6) ........ 111
Appendix 2 Values of the constants in equation (3.8) ........ 111
Appendix 3 Fitting details of Figure 3.5 (a) ........ 112
Appendix 4 The impedance spectra of 3.5%, 6.4% and 8.9% Ta-$TiO_2$ films ........ 115
Appendix 5 Zeview fitting parameters of R, R', $T_{CPE}$, $P_{CPE}$, $\omega''_{max}$ for the equivalent circuit in Fig.4.6 (c) ........ 117
Appendix 6 Transport and optical properties of $Ta_xTi_{1-x}O_2$ films with Ta concentration (x) between 20% and 30% ........ 118
Appendix 7 Transmittance spectrum of (001) $TiO_2$ substrate treated under different conditions ........ 121
Appendix 8 Comparison the magnetic property of $TiO_2$ substrates with (001) and (110) orientations annealed in the same vacuum condition ........ 122

# ABSTRACT

$TiO_2$ is a promising material for photo-catalytic water splitting and carbon dioxide reduction, both of which strongly depend on the positions of the valence and conduction band edges. Hence to modify the bandgap and also the valence and conduction band edge positions of $TiO_2$ to satisfy the energetic requirement for a photocatalytic reaction is one of the objectives of this thesis. While, pure $TiO_2$ is a semiconductor, Niobium (Nb) or Tantalum (Ta) doped (alloyed) $TiO_2$ shows metallic behavior. Hence it is important to study this transition from an insulator to a metal in detail, not only for the interesting fundamental science but also for its potential applications as transparent conducting oxides (TCOs). In addition, the magnetic property of $TiO_2$ substrate is studied as it is commercially available and is frequently used in many experiments involving dilute magnetic semiconducting oxide thin films. Besides $TiO_2$, a metallic oxide ($SrNbO_3$) with optical bandgap of 4 eV is studied for the potential application as TCOs and as photocatalyst in water splitting.

Ta doped (alloyed) $TiO_2$ thin film in anatase form is prepared by pulsed laser deposition and characterized by X-ray diffraction and Rutherford Backscattering Spectrometry. UV-visible spectroscopy shows the blue shift of the optical bandgap of the samples with increasing Ta concentration and the negative shift of the flat band potential (decrease of work function) with Ta doping (alloying) is verified by electrochemical impedance spectroscopy. By considering the changes of the optical bandgap and Fermi level, it is concluded that both the conduction and valence band edges shift negatively (the energy difference between the level and vacuum level is decreasing) with Ta concentration but with the former faster. Hence it is expected that the performance of Ta doped (alloyed) $TiO_2$ in photocatalytic experiments should improve as the electrons in the conduction band have higher energies.

Pure anatase $TiO_2$ thin film prepared under high vacuum may incorporate oxygen vacancies, which act as electron donors while the randomly distributed oxygen vacancies may introduce trapping potentials, which then reduce electrons' mobility. As a result of these, $TiO_2$ undergoes a metal-to-insulator transition at low temperatures. The transport behavior at low temperatures

may be attributed to variable range hopping showing strong coupling in magnetic field induced positive magnetoresistance. On the other hand, tuning the oxygen partial pressure during growth tunes the oxygen vacancies and compensating defects that in turn cause a resistivity-minimum, which is almost independent of the growth-temperature (within the favorable temperature range for the formation of anatase phase of $TiO_2$).

$TiO_2$ thin films with low Ta concentration (0.1% to 0.4%) are prepared for studying transport property as a function of Ta concentration. It is shown that a transition of strong to weak localizations exists at low temperatures (compared to undoped sample). Ta doping can improve the crystallinity of the sample as it can suppress the formation of oxygen vacancies, which then reduces localizations.

Reversible ferromagnetism has been found in commercially available rutile $TiO_2$ substrate by simply annealing it in high vacuum and recovering the non-magnetic state by annealing it in oxygen rich environment. It is shown that Ni impurity, which is responsible for the observed ferromagnetism, may exist in the pristine sample and can segregate to the top surface by vacuum annealing. The embedded Ni clusters in the vacuum annealed $TiO_2$ crystal near the sample surface will form a cermet structure, which exhibit a tunneling transport behavior at low temperatures.

An exciting TCO candidate $SrNbO_{3+\delta}$ film forms cubic perovskite structure on $LaAlO_3$ substrate with a lattice constant close to 4.1 Å. The optical bandgap of the film is measured as 4.0 eV and slightly decreases with oxygen partial pressure. Surprisingly, such large bandgap material prepared at $1 \times 10^{-5}$ Torr shows very low resistivity (~$1.8 \times 10^{-4}$ Ω-cm at room temperature), which is weakly dependent on the temperature. The resistivity of the film is strongly dependent on the deposition pressure where the films become insulating for the pressure $\geq 6 \times 10^{-5}$ Torr.

## LIST OF PUBLICATIONS

1) Y. L. Zhao, M. Motapothula, N. L. Yakovlev, Z. Q. Liu, S. Dhar, A. Rusydi, Ariando, M. B. H. Breese, Q. Wang, and T. Venkatesan, "*Reversible Ferromagnetism in rutile $TiO_2$ single crystals induced by nickel impurities*", Appl. Phys. Lett. **101**, 142105 (2012).

2) Y. L. Zhao, W. M. Lv, Z. Q. Liu, S. W. Zeng, M. Motapothula, S. Dhar, Ariando, Q. Wang, and T. Venkatesan, "*Variable range hopping in $TiO_2$ insulating layers for oxide electronic devices*", AIP ADVANCES **2**, 012129 (2012).

3) Y. L. Zhao, A. Roy Barman, S. Dhar, A. Annadi, M. Motapothula, Jinghao Wang, Haibin Su, M. Breese, T. Venkatesan, and Q.Wang, "*Scaling of flat band potential and dielectric constant as a function of Ta concentration in Ta-$TiO_2$ epitaxial films*", AIP ADVANCES **1**, 022151 (2011).

4) Z. Huang, X. Wang, Z. Q. Liu, W. M. Lu, S. W. Zeng, A. Annadi, Y. L. Zhao, W. L. Tan, T. Venkatesan, Ariando, "*Conducting channel at $LaAlO_3/SrTiO_3$ heterostructures*" Phys. Rev. B - Rapid Comm. (2013)– accepted, publishing.

5) A. Annadi, X. Wang, K. Gopinadhan, W. M. Lu, A. Roy Barman, Z. Q. Liu, A. Srivastava, S. Saha, Y. L. Zhao, S. W. Zeng, S. Dhar, N. Tuzla, E. Olsson, Q. Zhang, B. Gu, S. Yunoki, S. Maekawa, H. Hilgenkamp, T. Venkatesan, Ariando, "*Anisotropic two-dimensional electron gas at the $LaAlO_3/SrTiO_3$ (110) interface*" Nature Commun.**4**, 1838 (2013).

6) S. W. Zeng, X. Wang, W. M. Lu, Z. Huang, M. Motapothula, Z. Q. Liu, Y. L. Zhao, A. Annadi, S. Dhar, H. Mao, W. Chen, T. Venkatesan, Ariando, "*Metallic state in La-doped $YBa_2Cu_3O_y$ thin films with n-type charge carriers*" Phys. Rev. B **86**, 045124 (2012).

7) Z. Q. Liu, D. P. Leusink, Y. L. Zhao, X. Wang, X. H. Huang, W. M. Lü, A. Srivastava, A. Annadi, S. W. Zeng, K. Gopinadhan, S. Dhar, T. Venkatesan, Ariando, "*Metal-insulator transition in SrTiO3-x thin film induced by frozen-out carriers*", Phys. Rev. Lett. **107**, 146802 (2011).

8) Z. Q. Liu, D. P. Leusink, W. M. Lü, X. Wang, X. P. Yang, K. Gopinadhan, L. Y. Teng, Y. L. Zhao, A. Annadi, A. Roy Barman, S. Dhar, Y. P. Feng, H. B. Su, G. Xiong, T. Venkatesan, Ariando, "*Resistive switching mediated by the formation of quasi conduction band in a large bandgap insulating oxide*", Phys. Rev. B **84**, 165106 (2011).

9) A. Roy Barman, M. Motapothula, A. Annadi, K. Gopinadhan, Y. L. Zhao, Z. Yong, I. Santoso, Ariando, M. Breese, A. Rusydi, S. Dhar and T. Venkatesan, "*Multifunctional Ti1-xTaxO2: Ta Doping or Alloying?*", Appl. Phys. Lett. **98**, 072111 (2011).

10) Z. Huang, Z. Q. Liu, X. Wang, W. M. Lu, S. W. Zeng, A. Annadi, X. L. Tan, P. F. Chen, Y. L. Zhao, C. J. Li, W. B. Wu, T. Venkatesan, and Ariando, " *Controlling conductivity in strained* $SrTiO_3$*-based thin films*", Phys. Rev. B (2013) – submitted.

## LIST OF FIGURES

**Figure 1.1**: Schematic graphs of the band structures of (a) metal, (b) semiconductor, (c) insulator as defined in conventional textbooks. ................. 3

**Figure 1.2**: Schematic graphs of the band structures of (a) intrinsic semiconductor, (b) n type semiconductor, (c) p type semiconductor, (d) degenerate semiconductor. ................................................................. 4

**Figure 1.3**: Schematic graphs of the crystal structure of $TiO_2$ with form (a) rutile, (b) anatase, (c) brookite. ................................................................ 6

**Figure 1.4**: Schematic graphs of the (a) structure of DSC, (b) working principle of DSC. ................................................................................ 9

**Figure 1.5**: Schematic graphs of (a) working principle of semiconductor as electrode in photocatalytic water splitting, (b) energy band levels of typical semiconductors. ............................................................................ 11

**Figure 2.1**: Schematic graph of a pulsed laser deposition setup. .................... 13

**Figure 2.2**: Schematic graph of the working principle of X-ray diffraction. .. 14

**Figure 2.3**: Schematic graphs of the (a) RBS working geometry, (b) RBS spectrum operated in random mode. ............................................................. 15

**Figure 2.4**: Schematic graphs of RBS operated in ion channeling mode for a (a) perfect lattice, (b) disordered lattice. ............................................................ 16

**Figure 2.5**: Schematic graphs of (a) simple geometry of TEM system, (b) working principle of EDX. .......................................................................... 17

**Figure 2.6**: Schematic graphs of (a) working principle of UV-vis spectroscopy, (b) simple geometry of UV-vis spectroscopy system. .................................... 18

**Figure 2.7**: Schematic graphs of bonding in (a) Van der Pauw configuration, (b) linear configuration, (c) Hall measurement configuration. ............................. 21

**Figure 2.8**: Schematic graphs of the working principles of the (a) Josephson junction, (b) SQUID. ....................................................................... 23

**Figure 2.9**: Schematic graph of the working principle of XAS. ..................... 24

**Figure 3.1**: XRD spectrum of pure anatase $TiO_2$ deposited onto LAO (100) substrate. Bright spots in two dimensional detection systems indicate the single crystallites of the film and substrate. ............................................................ 27

**Figure 3.2**: Temperature dependent measurement of resistivity for samples prepared under deposition temperature 700°C and oxygen partial pressure $1.2\times10^{-5}$ Torr, $1.4\times10^{-5}$ Torr and $1.9\times10^{-5}$ Torr respectively. The green dash line indicates the curve fitting. ................................................................... 28

**Figure 3.3**: (a) Plot of resistivity with temperature by Mott VRH theory. Inset is the plot by taking considering the temperature dependent pre-exponential factor. The dash lines were guided by eyes. (b) Mathematical way to distinguish Mott VRH and ES VRH, as described in text. The dash lines were guided by eyes. ...... 30

**Figure 3.4**: Statistical study of the room temperature resistivity of the samples prepared with different oxygen partial pressure. ...... 32

**Figure 3.5**: (a) Transverse MR of the sample prepared under oxygen partial pressure $1.4\times10^{-5}$ Torr at different measurement temperatures. The arrows indicate the corresponding axis for the data measured at different temperatures. The dash lines are fitted to cubic polynomials. (b) Schematic diagram showing the MR measurement. (c) Angular dependent MR of the same sample under different temperatures and magnetic fields. Rotation angles were described in (b) and the arrows indicate the corresponding axis for the data. ...... 33

**Figure 3.6**: Hall coefficient (left axis) and mobility (right axis) measurement above 50 K for the sample prepared under oxygen partial pressure $1.4\times10^{-5}$ Torr. ...... 34

**Figure 4.1**: (a) UV-vis transmission spectra of pure and Ta-$TiO_2$ samples. (b) Blue shift of the optical bandgaps of anatase Ta-$TiO_2$ according to Tauc plot. ...... 37

**Figure 4.2**: Energy band diagram of a metal in contact with (a) N type semiconductor under thermal non-equilibrium condition (top) or in thermal equilibrium (bottom). (b) P type semiconductor under thermal non-equilibrium condition (top) or in thermal equilibrium (bottom). $\Phi_{sc}$ and $\Phi_m$ are the work functions of semiconductor and metal. $E_{fsc}$ and $E_{fm}$ are the Fermi levels of semiconductor and metal. $V_{bi}$ is the built in potential in the space charge region and e is the elementary charge. Space charge region is shadowed. ...... 38

**Figure 4.3**: (a) Real image and schematic graph of the working electrode used in EIS measurement. (b) Schematic graph of three electrodes setup. During measurement, current is applied between working and counter electrodes and voltage is measured between working and reference electrodes. (c) Calibration of the potential of the Ag/$AgNO_3$ reference electrode with respect to Ferrocene (1mM in 0.1M TBAP-acetonitrile solution) by CV measurement. ...... 40

**Figure 4.4**: Random and channeling spectra of 6.4% Ta-$TiO_2$ film showing excellent channeling yield. Ta concentration measured by RBS versus nominal Ta concentration in the PLD target is shown in the inset. ...... 42

**Figure 4.5**: Resistivity versus temperature of Ta-$TiO_2$ films as a function of Ta concentration. Inset shows the pure anatase performance. ...... 43

**Figure 4.6**: (a) Nyquist plots of pure $TiO_2$ with Al contact layer. The frequency range here is from 0.01 Hz to 30 kHz. The inset graph is in the expanded scale of the high frequency data. (b) Nyquist plots of 1.5% Ta incorporated $TiO_2$ without Al buffer contact layer. The frequency range shown here is from 0.01

Hz to 30 kHz. The inset graph is the expanded scale of the high frequency data. (c) Equivalent circuit of the samples in current EIS measurement.................45

**Figure 4.7**: Mott-Schottky plot of the samples. Right y-axis is for pure $TiO_2$, left y-axis is for Ta-$TiO_2$ samples. X-axis is the applied potential to the samples relative to the reference electrode. The straight lines were guided by eyes. The inset is the flat band potential of the samples obtained from the Mott-Schottky equations by considering the applied potential plot.......................................46

**Figure 4.8**: (a) Hall effect measurement of the charge carrier density (black) and mobility (blue) of the samples together with the carrier density of the samples estimated from Mott-Schottky plot (red). (b) Dielectric constant as function of measured Ta concentration calculated by reconciling Hall effect and Mott-Schottky measurements of carrier densities. (c) Comparison of Sheet resistance of the films as function of measured Ta concentration obtained from direct resistivity measurement and from Mott-Schottky plot. .........................48

**Figure 4.9**: Experimentally obtained Fermi level (red) and optical bandgap blue shift of the Ta incorporated $TiO_2$ samples where pure $TiO_2$ was selected as the reference point (blue), and simulated Fermi level shift with measured Ta doping concentration (black), the shift value of the first point (3.125%) is set as zero for easy comparison...........................................................................................50

**Figure 4.10**: (a) band structure of pure anatase $TiO_2$ (b) Total and partial DOS for pure anatase $TiO_2$. ..........................................................................52

**Figure 4.11**: (a) Band structure of 12.5% Ta doped $TiO_2$ (b) Total and partial DOS for 12.5% Ta doped anatase $TiO_2$ (c) Projected DOS of Ta atoms. ........53

**Figure 5.1**: (a) In Anderson model, it is assumed that only one magnetic impurity is surrounded by a Fermi sea, and within the magnetic impurity, there is only one energy state with energy $\varepsilon_0$ been occupied by one spin up electron (blue) below the Fermi energy of the metal (orange). Coulomb energy $U$ indicates the energy needed to add another electron to the state and $|\varepsilon_o|$ is the minimum energy to move the electron from the impurity's state to the Fermi sea. In quantum mechanics, the electron in the impurity's state may tunnel out and stay in a virtual state temporally until the state is occupied by an electron from the Fermi sea. Such process may change the spin of the electron in the impurity's state. (b) Density of states of the combination of many such events described in (a) and the resonance states at the Fermi energy (causing Kondo scattering) with different probabilities can be obtained at different temperatures, ($\Gamma$ is the width of the impurity's state) showing a decrease in Kondo scattering with increasing temperature [119]. .................................................................57

**Figure 5.2**: Trajectories of an electron returning to the initial points. *C* and *D* indicate the same trajectory but different directions. Only trajectory *C* and *D* can interference as they are phase coherent...................................................59

**Figure 5.3**: Temperature dependent resistivity measurement of $TiO_2$ samples with Ta concentrations (a) 0.1% (b) 0.2% (c) 0.3% (d) 0.4% and (e) Plot of $T_{min}$ with Ta concentration.........................................................................61

**Figure 5.4**: (a) the measurement configuration. During experiment, sample is rotated as shown. (b) MR of 0.1% Ta doped $TiO_2$ thin film measured at 2 K and 5 K. Angles are measured between the magnetic field and central axis, as shown in (a). (c) MR of the same sample in (b) measured at 10 K, 20 K and 30 K. (d) MR of the same sample measured at 50 K and 70 K. .................................... 62

**Figure 5.5**: (a) MR of 0.2% Ta doped $TiO_2$ measured at different temperatures. (b) MR of the same sample in (a) measured at different configurations; angles are described in Fig. 5.4 (d). (c) MR of 0.3% Ta doped $TiO_2$ measured at different temperatures. (d) MR of 0.4% Ta doped $TiO_2$ measured at different temperatures. .................................................................................... 64

**Figure 5.6**: Hall measurements of (a) 0.1% (b) 0.2% (c) 0.3% (d) 0.4% Ta -$TiO_2$ thin films. (e) Ta concentration dependent carrier density measured at room temperature (left axis) and effective Ta percentage (right axis). The straight lines are guided by eyes. (f) Ta concentration dependent maximum mobility of the films in (a) (b) (c) and (d). ......................................................................... 66

**Figure 6.1**: (a) Principle of diamagnetism: the internal field repels the applied magnetic field. (b) Principle of paramagnetism. Without external magnetic field, the net magnetization is zero. By applying field, linear relation of magnetic moment and applied field can be seen. (c) Plot of susceptibility of paramagnetic (positive $\chi$) and diamagnetic (negative $\chi$) materials with temperature. (d) Principle of ferromagnetism. Without magnetic field, net positive magnetization exists. (e) Principle of anti-ferromagnetism, where its lattice equals two sub-lattices with equal amplitude but opposite direction of spin configurations. (f) Principle of ferrimagnetism, where the sub-lattices have different amplitude of spins. (g) Formation of magnetic domains can minimize the magnetostatic energy. (h) Different behaviors of M-H relationship of paramagnetism (green), ferromagnetism (blue) and superparamagnetism (red). ..................................................................................................... 69

**Figure 6.2**: (a) Magnetic moment versus field (MH) measurement of $TiO_2$ substrate at room temperature. The annealing temperature is 800°C and the annealing time is 2 hours. The vacuum level is kept at $5\times10^{-6}$ Torr. Inset shows the photo of pristine, vacuum annealed and subsequently air annealed samples. (b) Room temperature MH measurements of $TiO_2$ substrates vacuum annealed with 800°C for different times. Here paramagnetic part of the signal was deducted. (c) Room temperature MH measurements of $TiO_2$ substrates vacuum annealed for 2 hours with different temperatures. Only the ferromagnetism component is shown. (d) MH measurement at 10 K and room temperature of samples oriented in-plane and out-of-plane with magnetic field. Black and red colors indicate the out-of-plane plot at room temperature and 10 K. Blue and fuchsia colors indicate the in-plane plot at room temperature and 10 K respectively. Inset at the left corner shows the schematic graph of in-plane and out-of-plane configuration. Inset at the right corner shows the changes of saturation magnetization (magnetic moment at 4000 Oe in the main graph) and coercivity with temperature in the in-plane measurement. ............................ 75

**Figure 6.3**: (a) Temperature dependent resistivity measurement of $TiO_2$ samples vacuum annealed for 2, 4 and 8 hours. Thickness of 50 nm was used in

the calculation. The curve near 300 K is expanded in the inset. (b) Hall effect measurement of the samples described in (a). The solid circles indicate the charge carrier density and the open circles represent mobility. ......................77

**Figure 6.4**: (a) SIMS data of as received, vacuum annealed and air annealed $TiO_2$. The vacuum and air annealing time is 4 hours. (b) RBS random curve of as received, vacuum annealed and air annealed $TiO_2$ substrates as in (a). (c) RBS random, channeling and curve fit for the vacuum annealed sample in (a). (d) RBS random peak of $TiO_2$ samples vacuum annealed for 1, 2 and 4 hours. Inset shows Ni peak intensity ratio and $M_s$ ratio of the $TiO_2$ samples annealed in vacuum for different times. Ni peak intensity was calculated by integration of the Ni peak area. ..........................................................................................79

**Figure 6.5**: (a) HRTEM image of $TiO_2$ crystal vacuum annealed at 800°C for 4 hours. The likely Ni rich areas are shown by white circles. (b) Elemental scan of the same area described in (a), where the two dash lines show the boundary of the Ni rich region. ..........................................................................................80

**Figure 6.6**: (a) Magnetic moment of $TiO_2$ as function of the measuring temperature. In the legend, the number ahead of FC indicates the cooling field. For example, 50FC represents that the cooling field is 50 Oe. (b) XAS data of the as received, vacuum annealed and air annealed $TiO_2$ samples. .................82

**Figure 7.1**: XRD spectrum of $SrNbO_{3+\delta}$ films prepared at 750°C and different oxygen partial pressures. Labels LAO (*h*00) indicates the substrates' signal and SNO (*h*00) indicates the films' signal. Inset shows the rocking curve of the films at SNO (200) peaks. Background figure shows the 2D XRD patterns of SNO film on LAO substrate. The bright yellow spots are corresponding for particular peaks in 2θ plot. ..........................................................................................87

**Figure 7.2**: (a) TEM image of $SrNbO_{3+\delta}$ film on LAO substrate. The film is prepared under $1 \times 10^{-5}$ Torr. (b) Atomic resolution of $SrNbO_{3+\delta}$ film. (c) Atomic resolution of LAO substrate. (d) Electron diffraction pattern of $SrNbO_{3+\delta}$ film. (e) Electron diffraction pattern of LAO substrate. ..................88

**Figure 7.3**: (a) Transmission of the films prepared under 750°C and series of oxygen partial pressures. (b) Tauc plot of the spectrums in (a). ......................89

**Figure 7.4**: Temperature dependent resistivity of the sample prepared under 750°C and $1 \times 10^{-5}$ Torr. Inset shows the room temperature resistivity of the samples as a function of the oxygen partial pressures. ...................................90

**Figure 7.5**: Temperature dependent charge carrier density and mobility of $SrNbO_{3+\delta}$ film on LAO substrate. The film was deposited under $1 \times 10^{-5}$ Torr. ..........................................................................................91

**Figure 7.6**: (a) X–ray photoelectron spectroscopy of $SrNbO_{3+\delta}$ film prepared under 750°C and $1 \times 10^{-5}$ Torr. The binding energies were referenced to the adventitious C 1*s* peak (284.5 eV). The spectrum is simulated by superposition of two sets of Nb 3*d* peaks where the $3d_{5/2}$ peaks for $Nb^{5+}$ and $Nb^{4+}$ are located at 206.63 eV and 204.12 eV respectively. The ratio of the peak area intensity of

$Nb^{5+}$ and $Nb^{4+}$ is about 6.4:1. (b) Ultraviolet photoelectron spectroscopy of the film in (a). The beam energy is 21.2 eV. The work function of the electron analyzer was calibrated as 4.47 eV. 5 V bias was applied to the sample. Kinetic energy of the secondary edge was measured as 4.26 eV, as indicated by the black line cutting off the horizontal axis. (c) Energy difference between the Fermi level and valence band edge. Fermi level was calibrated as 0 binding energy. Inset shows the wide scan of the spectrum........................................93

**Figure 7.7**: Particle (proton) induced x-ray emission spectrum of $SrNbO_{3+\delta}$ films deposited on LAO substrate under different oxygen partial pressures. Peaks corresponding to particular element are labeled..................................94

**AppFig 3.1**: Cubic polynomial fitting of the MR at 2 K..............................112

**AppFig 3.2**: Cubic polynomial fitting of the MR at 5 K..............................112

**AppFig 3.3**: Cubic polynomial fitting of the MR at 8 K..............................113

**AppFig 3.4**: Cubic polynomial fitting of the MR at 10 K............................113

**AppFig 3.5**: Cubic polynomial fitting of the MR at 50 K............................114

**AppFig 4.1**: Nyquist plots of 3.5% Ta incorporated $TiO_2$ without Al buffer contact layer. The frequency range shown here is from 0.1 Hz to 30 kHz. The inset graph is the expanded scale of the high frequency data.......................115

**AppFig 4.2**: Nyquist plots of 6.4% Ta incorporated $TiO_2$ without Al buffer contact layer. The frequency range shown here is from 0.1 Hz to 30 kHz. The inset graph is the expanded scale of the high frequency data.......................116

**AppFig 4.3**: Nyquist plots of 8.9% Ta incorporated $TiO_2$ without Al buffer contact layer. The frequency range shown here is from 0.1 Hz to 30 kHz. The inset graph is the expanded scale of the high frequency data.......................116

**AppFig 6.1**: (a) Temperature dependent resistivity of Ta-$TiO_2$ films with different Ta concentrations. (b) Temperature dependent charge carrier density (left axis) and mobility (right axis) of the films in (a)..................................119

**AppFig 6.2**: (a) Transmission of Ta incorporated $TiO_2$ films in anatase phase with Ta concentrations of 20%, 25% and 30%. (b) The corresponding Tauc plot of the films in (a). Indirect bandgap model is applied in Tauc plot..............120

**AppFig 7**: Transmittance spectrum of (001) $TiO_2$ substrate treated under different conditions: as received (black); annealed in vacuum ($5\times10^{-6}$ Torr) with 800 °C (red) for 4 hours; and subsequently annealed in air with 800 °C (blue) for 2 hours……………………………………………………………116

**AppFig 8**: Magnetic moment versus field (MH) measurement of $TiO_2$ substrate with different orientations. The annealing temperature is 800°C and the annealing time is 2hours……………………………………………………117

**LIST OF SYMBOLS**

| | | | |
|---|---|---|---|
| $R$ | Resistance | $H$ | Magnetic field |
| $\rho$ | Resistivity | K | Kelvin |
| $R_s$ | Sheet resistance | $t$ | Time |
| σ | Conductivity | $V$ | Voltage |
| $T$ | Temperature | $I$ | Current |
| $B$ | Magnetic field | $H_c$ | Coercivity |
| $M$ | Magnetic moment | $\mu$ | Mobility |
| $e$ | Electronic charge | $TiO_2$ | Titanium dioxide |
| $n$ | Electron carrier density | MR | Magnetoresistance |
| PLD | Pulsed laser deposition | XRD | X-ray diffraction |
| UV-vis | Ultraviolet-visible | DOS | Density of states |
| RBS | Rutherford backscattering spectrometry | | |
| LAO | Lanthanum aluminates ($LaAlO_3$) | | |
| TCO | Transparent conducting oxide | | |
| DMS | Dilute magnetic semiconductors | | |
| XAS | X-ray absorption spectroscopy | | |
| SIMS | Secondary ion mass spectroscopy | | |
| TEM | Transmission electron microscopy | | |
| EDX | Energy dispersive x-ray spectroscopy | | |
| SQUID | Superconducting quantum interference device | | |
| PPMS | Physical properties measurement system | | |
| EIS | Electrochemical impedance spectroscopy | | |
| TBAP | Tetrabutylammonium perchlorate | | |
| HOMO | Highest occupied molecular orbital | | |
| LUMO | Lowest unoccupied molecular orbital | | |
| VRH | Variable range hopping | $E_g$ | Energy bandgap |
| DSC | Dye sensitized solar cells | QI | Quantum interference |
| DFT | Density function theory | CV | Cyclic voltammetry |
| ppm | Parts per million | ZFC | Zero field cooling |
| CPE | Constant phase element | $\mu_B$ | Bohr magneton |
| CB | Conduction band | VB | Valence band |
| $V_{fb}$ | Flat band potential | $k_B$ | Boltzmann constant |

| | |
|---|---|
| XPS | X-ray photoelectron spectroscopy |
| UPS | Ultraviolet photoelectron spectroscopy |
| PL | Photoluminescence |
| PIXE | Particle induced x-ray emission |

# Chapter 1 Introduction

## 1.1 Motivation and scope of the thesis

Titanium dioxide ($TiO_2$) is one of the most important oxide semiconductors on account of its diverse applications in heterogeneous catalysis [1, 2], solar cells [3, 4], water splitting [5-7], gas sensors [8, 9], optical coating [10], and electronic devices [11]. It has found applications in bone implants (because of its biocompatibility) and in lithium batteries (because of its chemical compatibility) [12-15]. Most of the applications are related to the bandgap edges and the position of Fermi level of the material. $TiO_2$ only absorbs ultraviolet light because of its large bandgap. People have modified $TiO_2$ by anionic dopants for narrowing its bandgap so that more solar energy can be utilized [5, 16-19]. Regarding the shift of $TiO_2$ absorption onset towards visible region, several mechanisms were proposed although a debate existed [20-24]. Meantime, the effect of cationic dopants on the catalytic properties of $TiO_2$ generated wide interest [25-29]. Recently, blue shift of the optical bandgap of $TiO_2$ upon Ta incorporation was discovered [30]. However, the mechanism, especially the effect of cationic dopants (Ta) on the energy levels of $TiO_2$ is not systematically studied. This thesis will discuss the fundamental electronic and optical properties of $TiO_2$, which will enable us to understand the material better and engineer it (especially bandgap edges and Fermi level) for various applications with increased efficiency.

In last two decades, tremendous efforts were putted into studying the dilute magnetic semiconductors (DMS) for the applications in spintronic devices [31-37]. However, this future becomes less rossy because there is lack of sufficient evidence for the absence of magnetic impurities [38]. Here we will show some cautionary results regarding the study of DMS.

Recently, the predomination of semiconductors in photocatalytic water splitting studies was challenged by a metallic oxide, strontium niobate [39]. However, there is short of expectations that the mobility of the carrier can cover the shortage of internal field, which is needed to split photon generated electron-hole pairs. We have prepared single crystalline $SrNbO_3$ thin film and its structural, electronic and optical properties will be shown in details.

In this chapter, a basic introduction of energy bandgap and Fermi level will be

done as they are the “key concepts” to understand some of the experimental phenomenon in the following chapters. Then a brief introduction about $TiO_2$ and its application will be presented. In chapter 2, experimental thin film preparation and characterization techniques will be introduced. The effect of oxygen vacancies on the electronic transport properties of $TiO_2$ thin film in anatase phase will be discussed in chapter 3. In chapter 4, the studies of the blue shift of the bandgap of $TiO_2$ upon Ta incorporation will be developed by studying the corresponding shift of the Fermi level. From which we have concluded that Ta incorporation causes both the conduction and valence band edges shifting towards vacuum level with the former faster. This compelling finding has given us a reasonable assumption that Ta incorporated $TiO_2$ can be applied better than pure $TiO_2$ in photo-catalytic experiment. The incorporation of Ta ions caused insulator to metal transition of $TiO_2$ film in anatase phase is studied in chapter 5, where the measured transition point of Ta concentration is compared to the estimated value in chapter 4 and showing consistency. In chapter 6, reversible ferromagnetism of $TiO_2$ substrate in rutile phase due to segregation and diffusion of nickel impurities are carefully studied. In chapter 7 we will show that $SrNbO_3$ can form single crystalline film with perovskite structure on $LaAlO_3$ substrate. The film has a large optical bandgap (close to 4 eV) but surprisingly a low resistivity (in the order of $10^{-4}$ **Ω**·cm at room temperature). This low resistivity is contributed more by the charge carrier density (in the order of $10^{22}/cm^3$ at room temperature) than by the mobility (within 10 $cm^2/Vs$ at room temperature). Last chapter is the summary and outlook of this thesis, where the difficulties of implementing the assumption in chapter 4 is pointed out. In addition, some aborted results are briefly mentioned and some further possible improvements are proposed.

## 1.2 Brief introduction of concept of energy bandgap

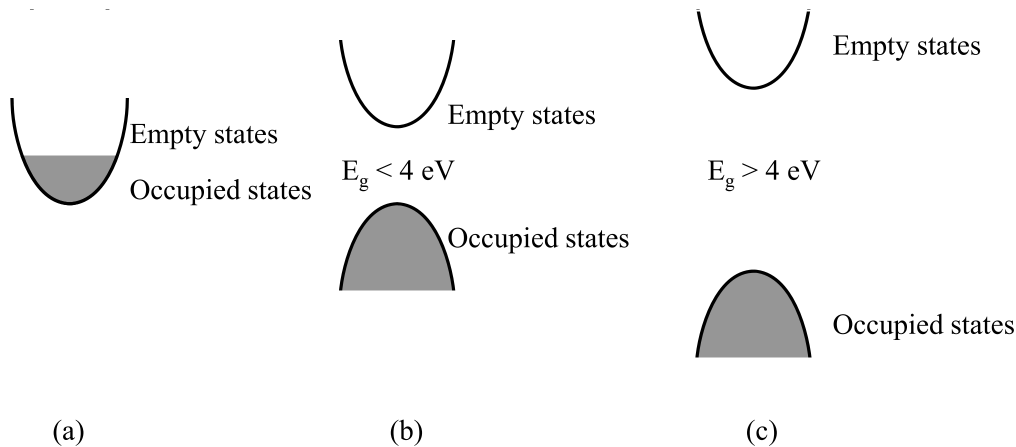


**Figure 1.1: Schematic graphs of the band structures of (a) metal, (b) semiconductor, (c) insulator as defined in conventional textbooks.**

Energy bandgap ($E_g$) is the concept in solid state physics to categorize materials in terms of their electronic properties as metals, semiconductors and insulators. Electrons moving in a solid are affected by the periodic potential which depends on the crystal structure. By considering the overall effect of periodic potential, there is a forbidden region for electrons to exist in the energy levels, which is called energy bandgap. As shown in Fig. 1.1, energy bandgap ($E_g$) separates the conduction band (CB) and valence band (VB). In some references, $E_g$ is used to differentiate metal, semiconductor and insulator [40]. In metals (Fig. 1.1(a)), bandgap does not exist; hence, electrons can move freely within the states. In semiconductors (Fig. 1.1(b)), $E_g$ is less than 4 eV. When $E_g$ is above 4 eV, the solid is normally classified as insulator (Fig. 1.1(c)). However, as the development of doping method, the boundary between semiconductors and insulators is no longer so strict (4 eV). Some material with small bandgap (< 4 eV) may be very resistive when the Fermi level is far away from the bandgap edges; on the other hand, some material with large bandgap (> 4 eV) may become semiconducting when energy levels are formed near the bandgap edges. Hence the ability to create shallow energy levels can be used as a criterion to separate semiconductors from insulators. In semiconductors, shallow energy levels near the bandgap edges can be easily formed by intrinsic or extrinsic doping, which will be able to promote donor electrons to the CB or acceptor holes to the VB easily by thermal excitations.

In contrast, the preference to create such shallow energy states in the bandgap of insulators is weak [41].

The relative position of the Fermi level to the bandgap edges may further classify semiconductors. For intrinsic semiconductor (Fig. 1.2(a)), Fermi level ($E_f$) is at the center of the bandgap. When $E_f$ is close to the CB, it is called *n*-type semiconductor (Fig. 1.2(b)) because the dominant charge carrier is electron. When $E_f$ is close to the valance band, it is called *p*-type semiconductor (Fig. 1.2(c)) because the dominant charge carrier is hole. When the defect bands are broad or are close to the CB/ VB and $E_f$ crosses the CB edge or VB edge due to extrinsic doping, it is called degenerate semiconductor (Fig. 1.2(d)), which will show some metallic characteristics. Actually, doping is one of the most effective ways of introducing charge carriers in semiconductors. *N*-type or *p*-type semiconductors' formation depends on the outer shell electrons of the dopant compared with those of the host material. When the outer shell electrons of dopant are more, extra electrons will be donated to the host semiconductor. While in the opposite case, the dopant will require electrons from the host semiconductor and holes are then donated to the semiconductor.

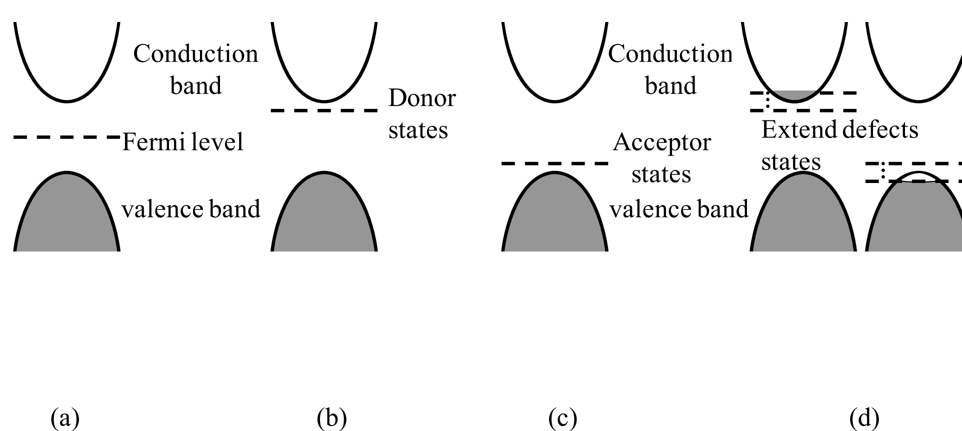


**Figure 1.2: Schematic graphs of the band structures of (a) intrinsic semiconductor, (b) n type semiconductor, (c) p type semiconductor, (d) degenerate semiconductor.**

Electrons in VB are strongly bonded or localized, while electrons in CB are highly mobile. Their differences are quantified by the concept of "Mobility". One of the most obvious quantities to separate metals, semiconductors and insulators is the conductivity, which depends on the mobility and the density

of charge carriers. Their relationship is expressed by a simple formula in Drude model [42, 43]:

$$\sigma = en_p\mu_p + en_e\mu_e \quad (1.1)$$

where $\sigma$ is the total conductivity, $e$ is the electronic charge, $n_p$ and $n_e$ are the densities of hole and electron, while $\mu_p$ and $\mu_e$ are the mobilities of hole and electron, respectively.

Electrons can transit within or across the bandgap when they acquire sufficient energy provided thermally or by electromagnetic radiation, which has applications in energy conversion devices like solar cells, light emitting diodes (LED) etc. Besides, many important characterization techniques including Photoluminescence (PL), X-ray spectroscopy (XPS), UV-visible spectrum, etc., were also designed based on this. In this thesis, most of the phenomenon will be explained based on “band theory” which is one of the most important concepts in solid state physics.

## 1.3 Fundamental physical and chemical properties of $TiO_2$

### 1.3.1 Crystal structures

There are three major phases of $TiO_2$ crystals in nature, which are rutile, anatase and brookite. Among them, rutile and anatase phases have received more attentions because of their wide applications. Rutile phase of $TiO_2$ is the most stable form, which has tetragonal structure. It belongs to the space group $P4_2/mnm$ [44, 45], as shown in Fig. 1.3(a). The lattice parameters are: $a = b =$ 4.587 Å, $c$ = 2.954 Å [46, 47]. Each unit cell contains two Ti atoms which are located at (*0*, *0*, *0*) and (*1/2*, *1/2*, *1/2*), and four O atoms are located at (± *u*, ± *u*, *0*) and (± (*u*+*1/2*), ± (*1/2*-*u*), *1/2*), where $u$ = 0.305 Å. Each Ti atom is bonded to six O atoms, where the $TiO_6$ octahedron is slightly distorted, with the equatorial Ti-O bond length of 1.946 Å and the apical Ti-O bond length of 1.983 Å. The O-Ti-O bond angles have three values, which are 90°, 81.21°, and 98.79°.

Anatase $TiO_2$ is a metastable phase and can transform to rutile upon heating. It also has tetragonal structure but belongs to the space group I41/*amd* [48], as shown in Fig. 1.3 (b). The lattice parameters are: $a = b$ = 3.782 Å, $c$ = 9.502 Å [46, 47]. Each unit cell contains four Ti atoms which are located at (*0*, *0*, *0*), (*1/2*, *1/2*, *1/2*), (*1/2*, *0*, *1/4*) and (*0*, *1/2*, *3/4*) while eight O atoms are located at

($0$, $0$, $\pm u$), ($1/2$, $1/2$, ($1/2 \pm u$)), ($1/2$, $0$, ($1/4 \pm u$)) and ($0$, $1/2$, ($3/4 \pm u$)), where $u$ = 0.208 Å. Each Ti atom is bonded to six O atoms, where the $TiO_6$ octahedron is also slightly distorted, similar to rutile, with equatorial and apical bond-lengths of 1.934 Å and 1.980 Å, respectively. The O-Ti-O bond angles have three values, which are 90°, 78.1°, and 101.9°.

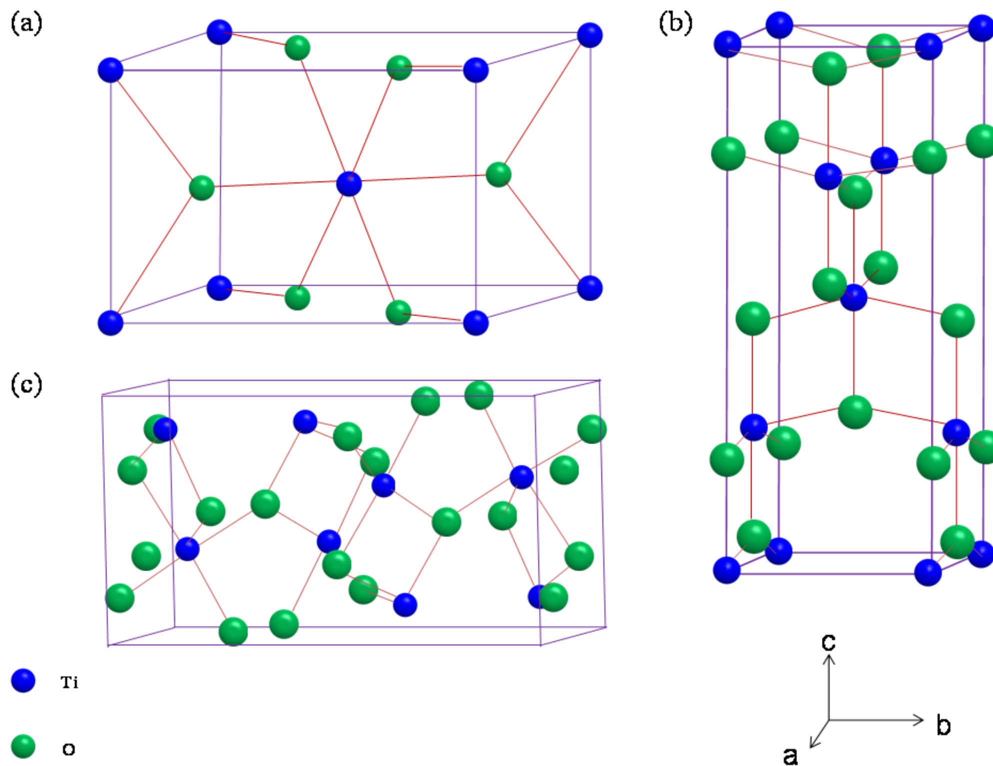


**Figure 1.3: Schematic graphs of the crystal structure of $TiO_2$ with form (a) rutile, (b) anatase, (c) brookite.**

Brookite $TiO_2$ has orthorhombic structure and belongs to space group P*bca* [49], as shown in Fig. 1.3(c). Each Ti sits at the center and coordinated octahedrally by six O atoms. The lattice parameters are: $a$ = 5.456 Å, $b$ = 9.182 Å and $c$ = 5.143 Å [45]. There are eight $TiO_2$ groups in Brookite unit cell, which is much larger than rutile and anatase. Brookite is the metastable form as well, which will change to rutile form above 750°C [50, 51].

In the following chapters, $TiO_2$ films are prepared in anatase phase which requires suitable substrate with small lattice mismatch. In addition, to eliminate the effect of the substrate on the measured electronic and magnetic signals of the sample, the substrate should be thermally inert in high vacuum because most of the films are prepared under such condition. $LaAlO_3$ (100)

was chosen as it satisfies all the above requirements. It has pseudocubic structure with the lattice constant a = 3.793 Å [52]. The small lattice mismatch (0.26%) between the film and the substrate promises the high quality of the sample. $LaAlO_3$ is thermally robust, which still shows insulating when it is annealed under the pressure 1 × 10-6 Torr and the temperature 800°C for more than 2 hours.

1.3.2 Electronic structures

The density of states (DOS) of three phases of $TiO_2$ introduced above have been extensively studies by density function theory (DFT) calculation [53]. Separated by the bandgap, the upper part of VB is mainly generated by $O_{2p}$ orbital and the lowest part of CB is mainly generated by $Ti_{3d}$ orbital which is composed of $t_{2g}$ ($d_{xy}$, $d_{xz}$ and $d_{yz}$) and $e_g$ ($d_{z^2}$, and $d_{x^2-y^2}$) bands. There are hybridizations between $O_{2p}$ and $Ti_{3d}$ orbital in both VB and CB regions. Although the DFT calculation has some limitations [54], such as weak predictions of bandgap value, its results were widely applied in explaining other phenomena and can be used for engineering the band structures of $TiO_2$. The absolute value of bandgaps of $TiO_2$ obtained from DFT calculation are much smaller than the actual value obtained from X-ray absorption experiment. The experimental results show that rutile $TiO_2$ has direct bandgap of 3.0 eV and anatase $TiO_2$ has indirect bandgap of 3.2 eV [55, 56]. The 0.2 eV energy difference was predicted by DFT calculation as well. Although the bandgaps of rutile and anatase are quite close, the electronic properties are very different [30, 57]. Anatase can become metallic upon introducing appropriate cationic dopants while, in contrast, rutile remains semiconducting. This is because in anatase phase a shallower defect level is formed upon doping [58]. The details on this phenomenon will be further discussed in the following chapters.

**1.4 Typical applications of $TiO_2$**

$TiO_2$ is widely applied as photo-catalyst [1, 3], as gas sensors [8, 9], in solar cells [4, 59], as heterogeneous catalysis [2], as corrosion protective coating [10], in electronic devices [11] and as white pigment [60]. Some of the applications are related to surface chemistry, and other various applications may be met by an appropriate tuning of the Fermi level. Due to the high dielectric constant and the high refractive index, rutile is suitable for electronic

and optical purpose while anatase is more suitable for catalysis purpose. In some applications, mix of rutile and anatase phase was shown as the optimized case. Here we will address several applications in details with an appropriate design of the experiments.

### 1.4.1 Transparent Conducting Oxides (TCOs)

A material with bandgap of ~ 3 eV will be transparent over the entire visible spectrum. Some of these (oxide) materials can be doped with shallow defect states, which can induce enough amounts of donors at room temperature to make the sample conductive. Then the material becomes both transparent and conductive [61, 62]. These kinds of materials are widely used in photo-electronic applications such as an ohmic contact electrode, as transparent windows in photovoltaic devices etc. To date, the commercially available TCOs include Tin doped Indium oxide (ITO) and Fluorine doped Tin oxide (FTO); the former has higher conductivity and is more expensive while the latter is cheaper and has lower transparency and conductivity. Recently, Nb doped anatase $TiO_2$ and Ta doped anatase $TiO_2$ were shown as interesting candidates [63, 64]. Here we will show that the bandgap and conductivity depend on the doping concentration in a wide range.

### 1.4.2 Dye Sensitized Solar Cell (DSC) and water splitting

Different from that in TCOs, where the absolute value of bandgap is crucial, in DSCs (first invented by Michael Grätzel, hence it is also called the Grätzel's cell) the locations of the bandgap edges are more important [4]. As shown in Fig. 1.4(a), typical DSC includes working electrode, electrolyte and counter electrode. Normally, mesoporous $TiO_2$ (made of $TiO_2$ powders code P25 which contains 80% of anatase and 20% of rutile phases) nanocrystalline layer on top of TCO substrate behaves as working electrode. TCO glass provides electrical contact for $TiO_2$ as well as letting light pass through. There is a layer of dye absorbed on the surface of $TiO_2$ particles, which is used for light absorbing. A redox couple (normally the iodide/triiodide couple) is dissolved in the electrolyte, which can mediate charges through the cell. The counter electrode is a piece of platinum coated TCO glass, which is attached to the working electrode by a melted polymer sealant, with electrolyte sealed in between. The working principle is shown in Fig. 1.4(b). In working process,

light enters the cell through the TCO of the photoanode and is then absorbed by the dye molecules. Electrons will then be excited from the highest occupied molecular orbital (HOMO) level to the lowest unoccupied molecular orbital (LUMO) level of the dye and then injected into the $TiO_2$ layer in subpicoseconds. Electrons will be transferred to the TCO of the working anode and then passing through the external circuit to the counter electrode. The oxidized dye will be reduced by iodide species in the electrolyte which are oxidized into triiodide. The electrons at the counter electrode can reduce the triiodide into iodide, thus establishing a closed circuit.

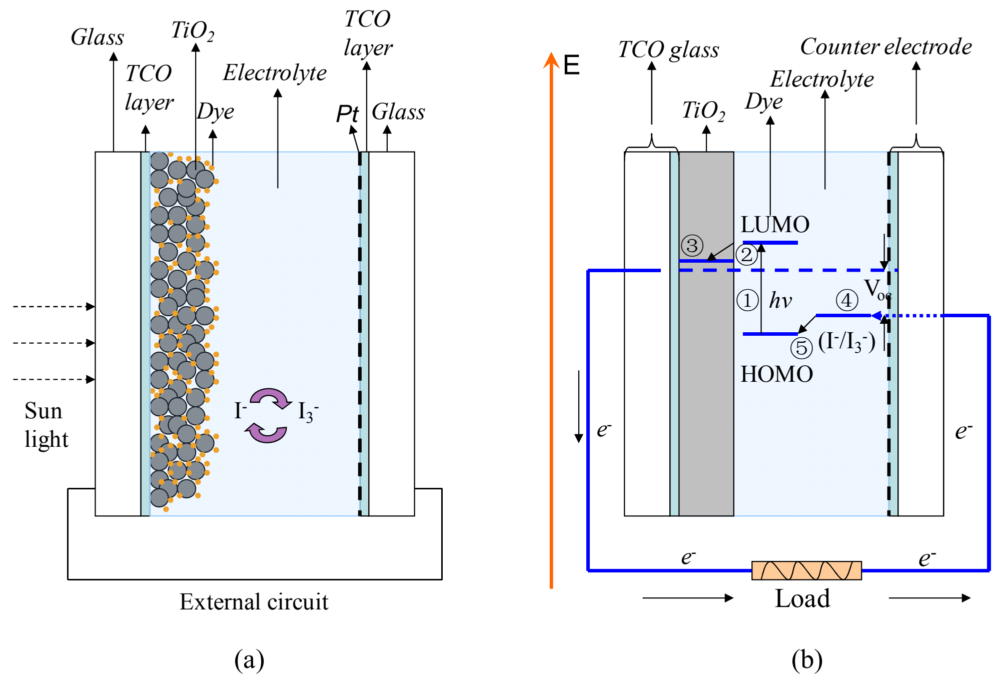


**Figure 1.4: Schematic graphs of the (a) structure of DSC, (b) working principle of DSC.**

The efficiency of DSC is determined by open circuit voltage ($V_{oc}$), short circuit current ($I_{sc}$) and the fill factor (*ff*). $V_{oc}$ is defined as the potential difference of the quasi Fermi level of $TiO_2$ and the electrochemical potential of the electrolyte. $I_{sc}$ depends of the charge injection, separation and recombination efficiencies. Both the factors depend on the location of CB edge of $TiO_2$. Hence understanding the CB edge movement is crucial to explain the dependence of efficiency of DSC by doping $TiO_2$ with cations or anions.

In DSC, $TiO_2$ was applied to directly convert solar energy into electrical

energy. Besides, it also can be used to convert solar energy into chemical energy, in which, splitting water into $H_2$ and $O_2$ is the most important one. $TiO_2$ is the first oxide material used in photo-catalytic water splitting experiment done by Fujishima and Honda [65]. As shown in Fig. 1.5(a), when the surface of $TiO_2$ is irradiated, photons with energies larger than 3.2 eV get absorbed. Electrons are excited from the VB to the CB leaving holes in the former. As the energy level of the VB edge is lower than the $H_2O$ oxidation level, holes diffuse to the surface of $TiO_2$ and convert $H_2O$ into $O_2$. The excited electrons flow to the counter electrode and reduce $H^+$ into $H_2$. In this experiment, only solar energy was consumed to split water into oxygen and hydrogen gases. Hence it attracted a lot of attentions in the "green energy resource" studies. Followed by this, several experimental and theoretical reports appeared [5, 66]. To split water theoretically, the minimum required voltage is 1.23 V. In reality, a much larger bandgap (1.9 ~ 2.0 eV) is needed [67]. Besides the bandgap, the band edge position has to be aligned with water redox potential. In addition, the electrode material must be chemically stable in the electrolyte. These requirements have already limited the available material. Fig. 1.5(b) shows the band edge positions of several semiconductors. As has been shown by many researchers, $TiO_2$ satisfies all the requirements except its large bandgap, which is out of visible light range. To overcome this drawback, tuning the bandgap by doping or combining $TiO_2$ with other smaller bandgap material was explored [6, 7]. Doping with cationic or anodic ions can change the properties (e.g. stability of the phase structure, conductivity, transparency) of $TiO_2$ drastically. However, the effect of cationic dopants on the shift of the energy levels is not fully understood. In this thesis, we will discuss the changing of the bandgap as well as the shift of the band edges of $TiO_2$ with Ta concentration, from which, people may get some sense about optimizing the tandem cell combination of improving the efficiency.

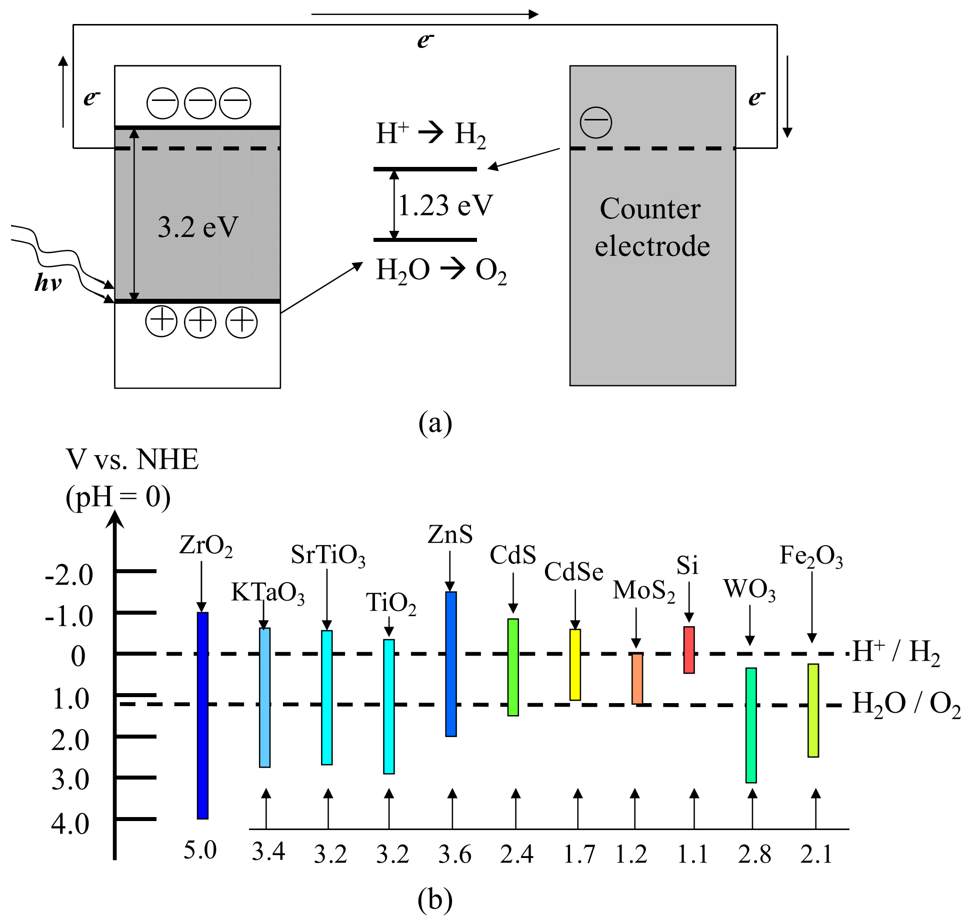


**Figure 1.5: Schematic graphs of (a) working principle of semiconductor as electrode in photocatalytic water splitting, (b) energy band levels of typical semiconductors.**

1.4.3 Other applications

Rutile $TiO_2$ is an important dielectric material for microelectronic application. Depending on the lattice orientation, rutile phase has dielectric constant ranging from 90 to 170, which is a high value for capacitors in future generations of memories [36]. Besides, $TiO_2$ is a promising candidate for applications in spintronics as the discovery of above room temperature ferromagnetism in Co doped $TiO_2$ thin films [37]. Nanostructured $TiO_2$ also involved in Li ion batteries and electrochromic devices [12, 13]. Not only limited in electronical, chemical and environmental applications, $TiO_2$ is applied in biological studies as well [14, 15]. Overall, $TiO_2$ is a very interesting and important material not only in fundamental physics but also in daily applications.

# Chapter 2 Basic sample preparation and characterization methods

## 2.1 Sample preparation technique: Pulsed Laser Deposition

$TiO_2$ thin films are prepared by Pulsed Laser Deposition (PLD) technique, which is a physical vapor deposition process with a precise control on the material's stoichiometry, carried out in a vacuum system. As shown in Fig. 2.1, a pulsed laser beam is passed through a glass window and focused onto a target. When the energy density of the laser is high enough, a plasma plume can be generated. The material flux provided by the plume will then accumulate at the surface of the substrate attached onto the heater whose temperature can be controlled during deposition. The heater is located 5 –10 cm away from the target. The laser used in this work is a Lambda Physik Excimer KrF UV laser with wavelength of 248 nm, maximum output energy of 1 J, pulse duration of 30 ns, and maximum frequency of 30 Hz. Before deposition, the chamber is pumped down to a base pressure of $10^{-7}$ Torr by using turbo molecular pump roughened and backed by an oil free rotary pump. The desired material may be grown as thin film in an appropriate ambience (e.g. $O_2$, $N_2$, Ar, $H_2$-Ar etc.).

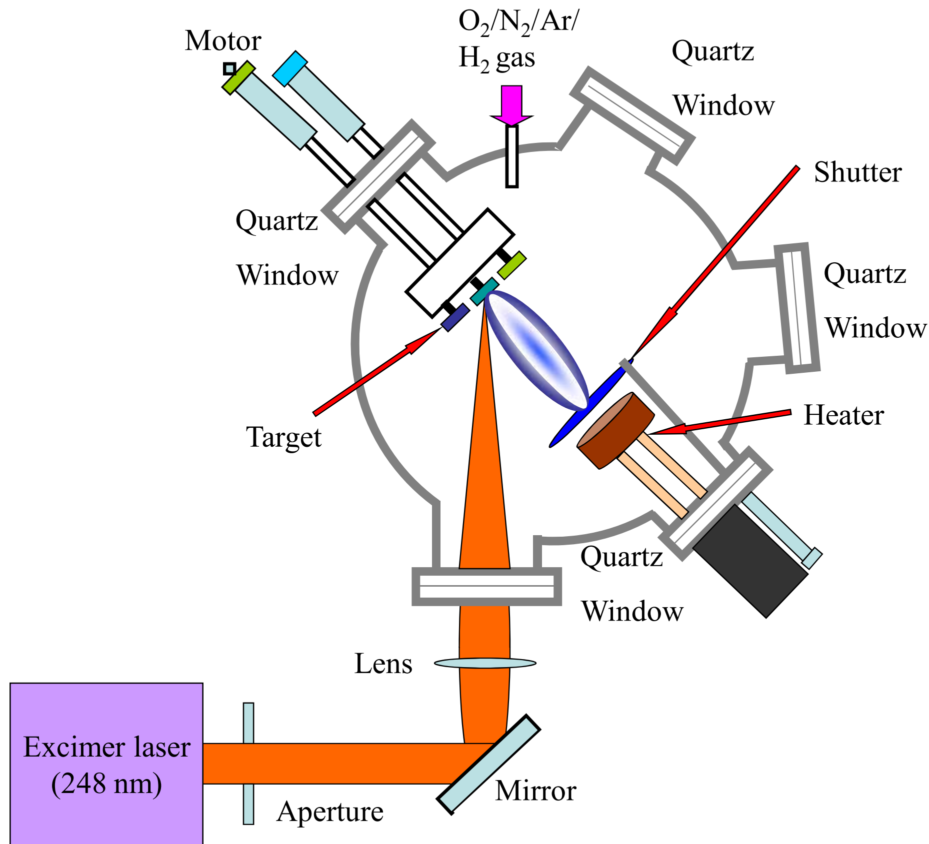


**Figure 2.1: Schematic graph of a pulsed laser deposition setup.**

## 2.2 Structure characterization techniques

### 2.2.1 X-ray diffraction

X-ray diffraction (XRD) is a nondestructive powerful technique for characterizing samples' crystal structures. The lattice parameter in *c-direction* (perpendicular to sample surface) may be elucidated by using Bragg's Law formulated as:

$$n\lambda = 2d\sin\theta, \qquad (2.1)$$

where $n$ is the diffraction order, $\lambda$ is the wavelength of X-ray, $d$ is the spacing between atomic planes parallel to sample surface and $\theta$ is the angle between sample surface and the incident X-ray beam, as shown in Fig. 2.2. In this thesis, crystal structures of the samples are characterized by Bruker D8 Discover X-ray system using Cu K$\alpha$ emission line operated at 40 kV, 40 mA. The diffraction pattern is recorded by a VÅNTEC-2000 2D detector, on which, an epitaxial film shows an image of bright spots while polycrystalline shows an image of bright ring patterns. The $d$–spacing, therefore, can be calculated

from the integrated curve and formula 2.1. By comparing with the database, the crystal structure of the sample can be determined.

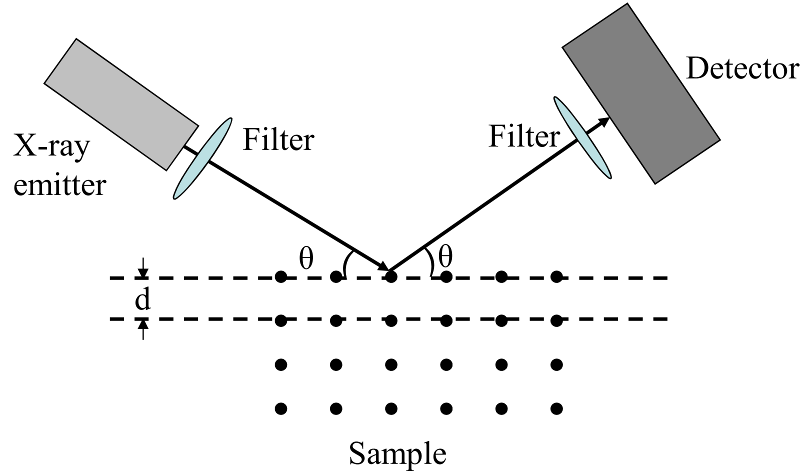


**Figure 2.2: Schematic graph of the working principle of X-ray diffraction.**

2.2.2 Rutherford Backscattering Spectrometry and Ion Channeling

Rutherford Backscattering Spectrometry (RBS) is a widely used nondestructive nuclear technique for the quantitative determination of the composition of a material and depth profiling of individual elements [68]. It has good sensitivity for heavy elements of the order of parts per million (ppm) and with a depth resolution of the order of several nm. During experiment, a beam of protons or $\alpha$ particles ($^{4}He^{2+}$) generated by an electrostatic accelerator (typically of energy 0.5-4 MeV) is directed towards the sample at normal incidence, as shown in Fig. 2.3(a). The energy ($E_1$) of the backscattered ions is given by [69]:

$$E_1 = \frac{M_1^2}{\left(M_1 + M_2\right)^2} \left\{ \cos\theta \pm \left[ \left( \frac{M_2}{M_1} \right)^2 - \sin^2\theta \right]^{1/2} \right\}^2 E_0 , \tag{2.2}$$

where $\theta$ is the scattering angle, $E_0$ is the incident energy while $M_1$ and $M_2$ are the mass of the incident particle and the target nucleus respectively.

In a material consists of two elements with a mass difference of $\Delta M_2$, the energy separation $\Delta E_1$ of backscattered particles is:

$$\Delta E_1 = E_0 \frac{dK}{dM_2} \Delta M_2 , \tag{2.3}$$

where $K$ is the polynomial anterior of $E_0$ in equation (2.2). As shown in Fig.

2.3(b), $\alpha$-particles are backscattered by two different elements with mass $M_2$ and $M_2'$. The backscattered $\alpha$ particles have different energies, width and peak intensities. From the energy (peak position), elemental property of the sample can be obtained, while the width tell us the depth of the element in the sample and the peak intensities indicate the elemental concentrations.

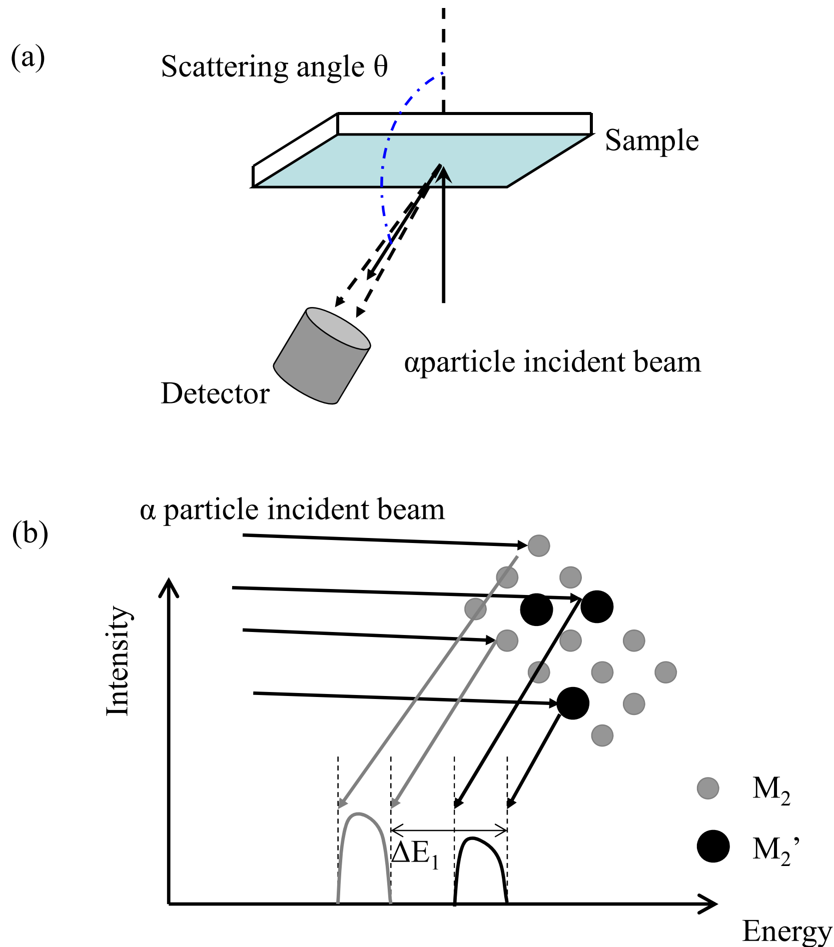


**Figure 2.3: Schematic graphs of the (a) RBS working geometry, (b) RBS spectrum operated in random mode.**

The crystal quality (crystal order) can be determined quantitatively by RBS operated in ion channeling mode. The working principle can be pictorially depicted as shown in Fig. 2.4(a). When the crystal is highly ordered and the incident beam is aligned exactly along the crystallographic directions, the incident beam is steered away from the lattice atomic strings and mostly travelling in the open spaces of the lattice by escaping the wide angle backscattering events. In such case the backscattering only occurs when the incident beam sees the top surface atomic strings, then next atoms along the

rows will be shadowed, that's where the surface peak appears in the RBS-Channeling spectra. In contrast, a disordered crystal will increase the probability of backscattering of the incident $\alpha$ particle, as shown in Fig. 2.4(b). The ratio of the yields from aligned to random spectra at the below of surface peak edges is named minimum yield ($\chi_{\min} = \frac{I_{channel}}{I_{random}}$), which provides the crystallinity information of an element in the crystal.

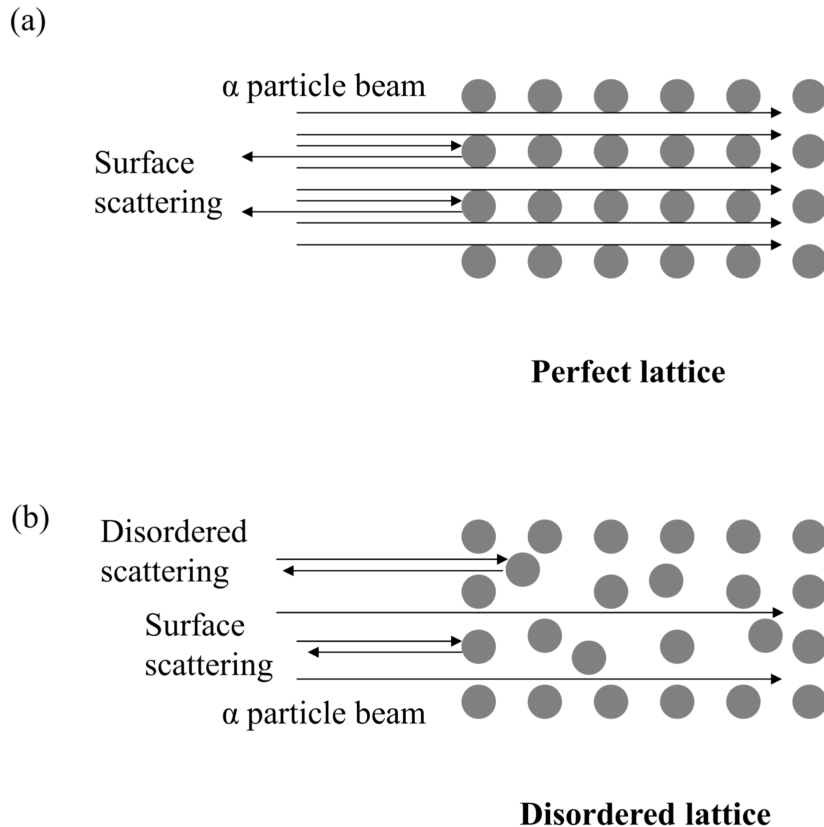


**Figure 2.4: Schematic graphs of RBS operated in ion channeling mode for a (a) perfect lattice, (b) disordered lattice.**

2.2.3 Transmission Electron Microscopy & Energy-dispersive X-ray spectroscopy

Transmission Electron Microscopy (TEM) is a powerful technique for charactering the real images of samples with atomic resolution. The essential components of a TEM are shown in Fig. 2.5(a). During experiment, electrons are emitted from the source, which may be a tungsten filament or a $LaB_6$ crystal. Then they are accelerated by an electric field and focused onto the sample by electromagnetic lenses. The electrons will interact with the sample

specimen with some portion of them scattered before passing through the sample. A real image will be formed on the imaging device with transformation of the diffraction patterns formed by the scattered electrons. The crucial part in TEM experiment is the sample preparation process. For thin film sample, the sample thickness has to be reduced to 30 – 50 μm scale.

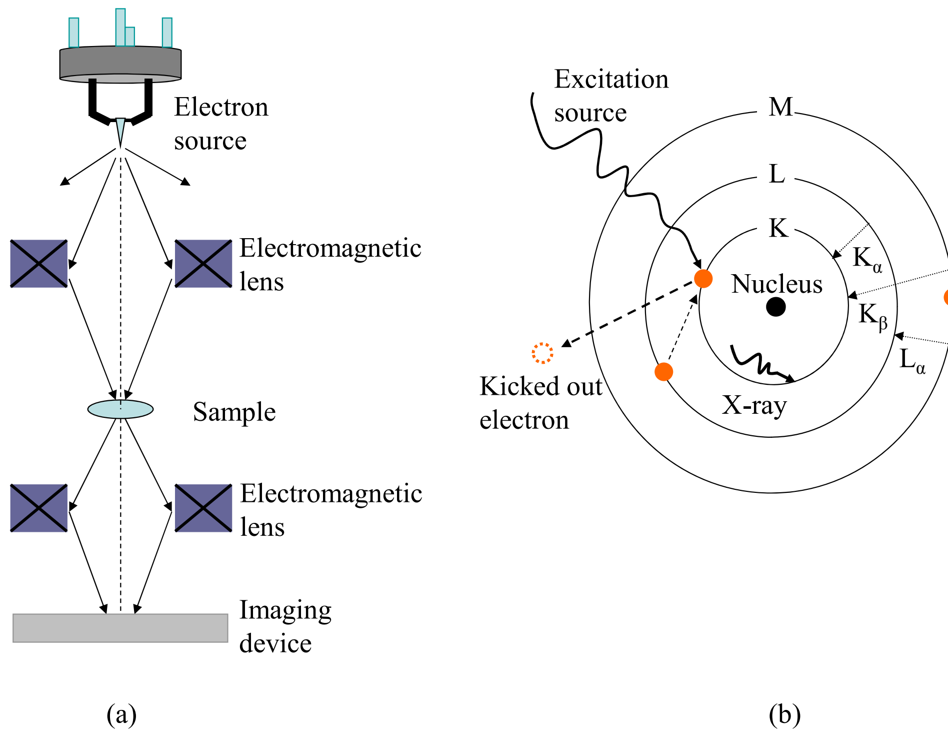


**Figure 2.5: Schematic graphs of (a) simple geometry of TEM system, (b) working principle of EDX.**

Energy-dispersive X-ray (EDX) spectroscopy is designed based on the fundamental principle that each element has a unique atomic structure which allows electrons' transition between different orbitals and gives unique atomic X-ray spectrum. As shown in Fig. 2.5(b), electrons in inner orbital can be kicked out by external energy source (electrons or protons) and leave the orbital empty. Then the electrons in outer orbital can release some energy and occupy the empty inner orbital. The released energy maybe in the form of X-ray and captured by an energy dispersive spectrometer. The energy difference between the outer and inner states is element dependent so that EDX can be used to determine the specimen composition. However, some elements have overlapped X-ray peaks (e.g., Mn $K_\beta$ and Fe $K_\alpha$, Ti $K_\beta$ and V $K_\alpha$), which will bring down its accuracy.

## 2.3 Optical bandgap and flat band potential study techniques

### 2.3.1 Ultraviolet-visible Spectroscopy

Ultraviolet-visible (UV-vis) Spectroscopy is a technique to investigate the transmittance (*T*), reflectance (*R*) and absorbance (*A*) of light of a material in solid, liquid or gaseous form. As the name implies, the wavelength covers ultraviolet (below 400 nm), visible (400 nm ~ 800 nm) range and a bit of infrared region (above 800 nm). The working principle is illustrated in Fig. 2.6(a), where a portion of the incident light is reflected with the rest transmitted or absorbed. Light with energy larger than the bandgap of the material is absorbed while that below the bandgap is transmitted.

The value of *T*, *R* and *A* satisfies the following equation:

$$A = -\ln\left(\frac{T}{1-R}\right) \tag{2.4}$$

In uniform material, *A* is proportional to the sample thickness $d$ as $A \propto \alpha \cdot d$, where $\alpha$ is the absorption coefficient. The wavelength dependent of $\alpha$ can be used to obtain optical bandgap, which will be shown in chapter 4. During experiment, monochromatic light intensities before ($I_0$) and after ($I$) passing through the sample are taken which gives *T* as ($I/I_0$), as shown in Fig. 2.6(b).

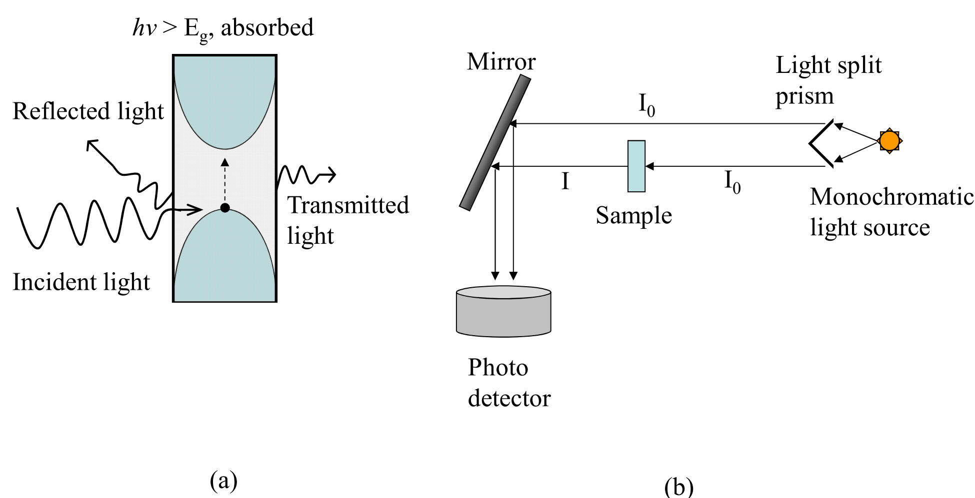


**Figure 2.6: Schematic graphs of (a) working principle of UV-vis spectroscopy, (b) simple geometry of UV-vis spectroscopy system.**

### 2.3.2 Electrochemical Impedance Spectroscopy

Electrochemical Impedance Spectroscopy (EIS) is a popular frequency domain technique applied for the determination of the double layer capacitance and to

the characterization of electrode processes and complex interfaces. During operation, a small amplitude, sinusoidal voltage ($V_0 \exp(i\omega t)$) is applied across the sample with the magnitude and phase angle of the current response ($I_0 \exp(i\omega t + \theta)$) captured as a function of frequency. The complex impedance can be calculated based on the following formula:

$$Z(\omega) = Z'(\omega) + iZ''(\omega) = \frac{V_0 \exp(i\omega t)}{I_0 \exp(i\omega t + \theta)} \quad (2.5)$$

where $i = \sqrt{-1}$, $Z(\omega)$ is the total impedance, $Z'(\omega)$ is the real part, $Z''(\omega)$ is the imaginary part, $\omega$ is the radial frequency, $V_0$ and $I_0$ are the amplitudes of the applied voltage and recorded current , and $\theta$ is the phase shift angle between the voltage and current.

As the impedance of a real system can be equivalent to the combinations (either in parallel or in series) of basic elements (e.g. resistor, capacitor and inductor) whose characteristic current responses of voltage are well known, in actual operation, an equivalent circuit is needed to simulate the experimental frequency-dependent impedance. A complex system may be represented mathematically by many possible equivalent circuits having multiple circuit elements and parameters; however, a proper equivalent circuit should be built up that can bring out a physically meaningful model explaining the system.

### 2.4 Transport properties study technique: Physical Property Measurement System

Physical Property Measurement System (PPMS) is an instrument to perform electrical and magneto-transport measurement at varying temperatures (ranging from 2 K to 400 K) and magnetic field (ranging from -9 Tesla to 9 Tesla). In transport studies, typically three types of measurements (temperature dependent resistance (*R(T)*), magnetoresistance (MR) and Hall effect) are performed. The resistance measurement may be performed with four probes either in van der Pauw configuration (Fig. 2.7(a)) or linear configuration (Fig. 2.7(b)). In the former geometry, current is applied along one edge of the sample ($I_{12}$) and the voltage is measured along the opposite edge ($V_{34}$). Then a resistance $R_{12,\,34}$ is defined as $V_{34}/I_{12}$. Similarly, another resistance $R_{13,\,24}$ can be obtained. From these two resistances, the actual sheet resistance ($R_s$) of the sample can be calculated based on the following formula

[70]:

$$e^{-\pi R_{12,34}/R_s} + e^{-\pi R_{13,24}/R_s} = 1 \tag{2.6}$$

In most cases, exact value of $R_s$ cannot be calculated from above equation except when $R_{12,34} = R_{13,24} = R$, then $R_s$ is given by

$$R_s = \frac{\pi R}{\ln 2} \tag{2.7}$$

For a known sample thickness ($d$), the resistivity ($\rho$) can be calculated as

$$\rho = R_s \cdot d \tag{2.8}$$

For the linear geometry, metal electrodes need to be placed on the sample to make the equal potential along each electrode. Then the resistivity of the sample is calculated as:

$$\rho = \frac{R \cdot A}{l} \tag{2.9}$$

where $R$ is the measured resistance, $A$ is the cross-section area and $l$ is the length between two voltage electrodes, as shown in the figure.

In the presence of magnetic field, the transport properties of a material may be changed. Among which, MR and Hall effect measurements are normally performed. The former is the study of the $R$(T) under magnetic field and the in-plane and out-of-plane MR of the specimen is measured with magnetic field parallel or perpendicular to its surface. Mathematically MR is defined as

$$\mathrm{MR} = \frac{R_{field} - R_{direct}}{R_{direct}} \times 100\% \tag{2.10}$$

where $R_{field}$ and $R_{direct}$ are the resistances measured with and without applying magnetic field.

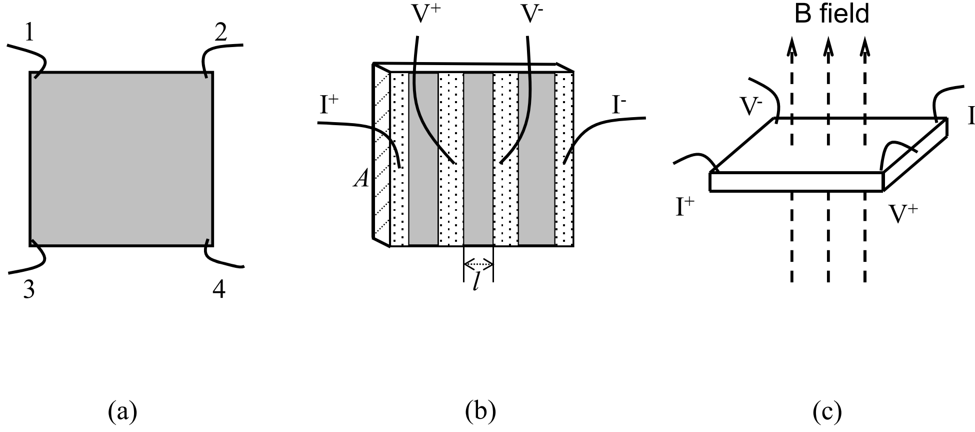


**Figure 2.7: Schematic graphs of bonding in (a) Van der Pauw configuration, (b) linear configuration, (c) Hall measurement configuration.**

The latter, Hall effect measurement is normally applied to study the charge carrier density and mobility. By passing through a current across the sample under magnetic field (with perpendicular component to the current direction), electrons deviate from their straight path, which accumulates charges on one face of the material. As a result, an in-plane potential difference is built up and perpendicular to the current direction. The measurement configuration is shown in Fig. 2.7(c), where current and voltage electrodes are bonded diagonally onto the sample. By scanning magnetic field ($B$), the built up voltage of a constant current ($I$) is defined as Hall voltage ($V_H$). With known sample thickness ($d$), the charge carrier density can be calculated with following equation:

$$n = \frac{I \cdot B}{e \cdot V_H \cdot d} \quad (2.11)$$

If there is only one type of charge carrier (e.g. electron, $n$) dominate in the semiconductor, the corresponding mobility ($\mu$) can be obtained as:

$$\mu = \frac{1}{en\rho} \quad (2.12)$$

## 2.5 Magnetism and impurity characterization techniques

### 2.5.1 Superconducting Quantum Interference Device-Vibrating Sample magnetometers

The magnetic properties of samples (magnetic moment ($M$) versus temperature ($T$) or magnetic moment ($M$) versus magnetic field ($H$)) can be measured by Superconducting Quantum Interference Device-Vibrating Sample

magnetometers (SQUID-VSM), which is designed based on Josephson Effect [71, 72]. As shown in Fig. 2.8(a), a Josephson junction is formed by sandwiching a thin layer of insulator by two weakly coupled superconductor layers. In superconductor one the electron-pair wave has phase $\phi_1$ while the electron-pair wave has phase $\phi_2$ in superconductor two. When the thickness of the insulator is close to several nanometers, a tunneling current may pass through the junction as a function of the phase difference($\Delta\phi = \phi_1 - \phi_2$) even in the absence of applying any voltage:

$$\mathrm{i} = i_c sin \Delta \phi \tag{2.13}$$

where $i_c$ is the critical current, a parameter which can be affected by temperature and applied magnetic field.

By compiling two Josephson junctions in parallel as a loop, as shown in Fig. 2.8(b), a simple SQUID device may be constructed for detecting magnetic signals. Without external magnetic field, an input current ($I$) will split into two equal branch currents ($I_a$, $I_b$). In the presence of an external magnetic field ($B$), a screening current ($I_s$) will flow in the circle to cancel the external magnetic flux ($\Phi$). Hence the currents across the two junctions become ($I/2 + I_s$) and ($I/2 - I_s$) separately. Whenever either of them exceeds the critical current of the Josephson junction, a voltage can be measured. Further increase $\Phi$ to exceed half the magnetic flux quantum ($\Phi_0 = \frac{2e}{h} = 2.07 \times 10^{-15}$Wb, $e$ is the electronic charge and $h$ is Planck's constant) will cause $I_s$ to flow in the opposite direction to ensure the flux in the loop be an integer number of $\Phi_0$. Thus $I_s$ changes its direction with a period of $\Phi_0$. Hence the magnetic signal can be measured in the electric signal [73]. During experiment, the system utilizes a superconducting magnet (solenoid superconducting wire made of NbTi alloy) to generate magnetic fields up to 9 Tesla and uses thermal heater and liquid Helium, which is compressed from Helium vapor to tune the sample temperature in the range of 400 K to 2 K. The sample under magnetic field will be magnetized with magnetic moment ($M$), and then generate flux in the SQUID coils been detected as electrical outputs. The sample is mounted onto a quartz holder by (GE) 7031 varnish with good thermal contact even at low temperature (e.g. 2 K) and negligible magnetic contributions.

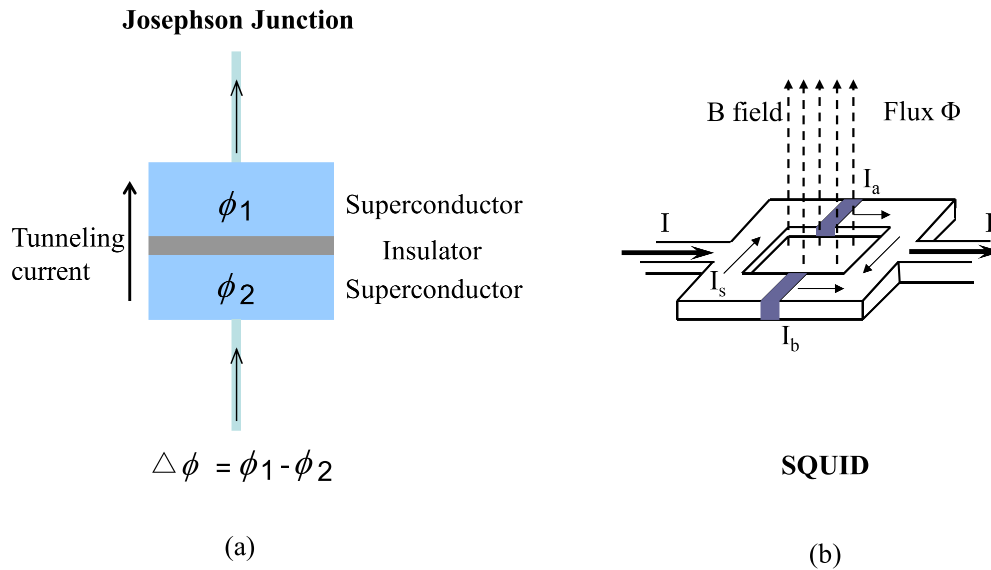


**Figure 2.8: Schematic graphs of the working principles of the (a) Josephson junction, (b) SQUID.**

2.5.2 Secondary Ion Mass Spectroscopy

Secondary Ion Mass Spectroscopy (SIMS) is a destructive technique used for analyzing the composition of solid materials. During experiment, the surface of the specimen is sputtered by primary ion beams ($Ar^+$) with secondary ions been ejected out of the surface and been collected by a detector and analyzed by mass spectrometer. SIMS is an extremely sensitive technique, which can limit the accuracy to ppm level. Similar to RBS, it is an ion mass sensitive technique, which is not sensitive to atomic states. To specify the ion state, X-ray spectroscopy needs to be applied.

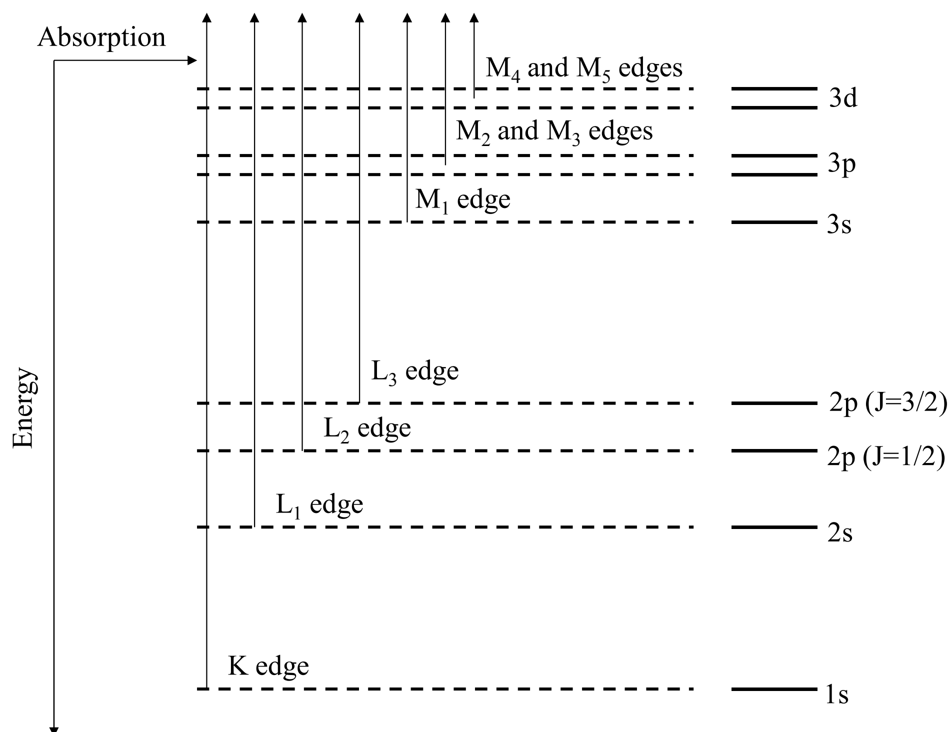


**Figure 2.9: Schematic graph of the working principle of XAS.**

### 2.5.3 X-ray Absorption Spectroscopy

X-ray Absorption Spectroscopy (XAS) is a technique widely used for determining the local geometric and electronic structures of samples, which may be in gaseous, liquid or solid phases. During experiment, an X-ray beam (usually at synchrotron radiation sources) is used to excite the core electrons to vacuum level. As electrons exist at different energy levels, the excitation energy is also different. As shown in Fig. 2.9, electrons in states with quantum number $n$ =1, 2, and 3 are corresponding to the K, L, and M edges, respectively. For example, excitation electrons from 1s level occurs at K edge; excitation electrons from 2s and 2p level occurs at L edge. As the excitation energy depends on the outer shell electrons as well, XAS is also sensitive to the atomic state. The details of this technique including spectrum analysis can be found in varieties of literatures [74].

# Chapter 3 Unexpected variable range hopping (VRH) mechanism observed in pure anatase $TiO_2$ thin film

Oxygen vacancies normally act as electron donor in *n*-type oxides. Hence we should expect resistivity reducing with deposition pressure in preparing thin film $TiO_2$ in anatase phase. In such case, a donor level is formed near the conduction band edge where the electrons can be driven to the conduction band by thermal energy (so called defect band model). More electrons will be excited by increasing temperature. As a result, mobility of the free electron reduces as the electron-phonon and electron-electron scatterings are enhanced [58]. However here, a sharp minimum in the resistivity of $TiO_2$ in anatase phase as a function of the sample preparing oxygen pressure was observed. The mobility of the sample with minimum resistivity increases with temperature, which is opposite of the expectation. The resistivity minimum formation is attributed to the competition between formations of oxygen vacancies and compensation defects (e.g. cationic vacancies). Such argument was developed from variable range hopping (VRH) mechanism, which is understood as the result of random potential induced electron trapping [75]. As the defects in $TiO_2$ (anionic and cationic) depend on the oxygen pressure, their effect on the VRH becomes crucially important not only for the fundamental understanding, but also for wide spread applications of $TiO_2$ [40].

## 3.1 Development of VRH theory

To understand the physical picture of hopping conduction, we can make a simple assumption. In an n type material the donor density $N_D$ is larger than the acceptor density $N_A$. At low temperatures, equal amount of $N_A$ electrons will drop down to fill in the acceptor states, leaving a fraction of $(N_D - N_A)/N_D$ of donor states been occupied by electrons. As the temperature increases, electrons will be excited and hop from the filled to empty donor states [76].

### 3.1.1 Mott VRH

Mott VRH is a model applied in strongly disordered systems for explaining low temperature conduction. Its dimensional temperature dependent conductance was first derived by Nevill Mott, as the following equation [77]:

$$\sigma = \sigma_0 \exp\left[-\left(\frac{T_0}{T}\right)^{1/(d+1)}\right] \tag{3.1}$$

where $\sigma_0$, $T_0$ are constants and $d$ is a number represents the dimension.

In the derivation, the most important assumption is that a hopping electron will always try to find the lowest activation energy and shortest hopping distance. It is shown that the hopping probability ($P$) at certain temperatures depends on the spatial distance of the sites ($r$) and the energy separation of the sites ($W$) as:

$$P \sim \exp\left(-2\alpha r - \frac{W}{k_B T}\right) \tag{3.2}$$

where $\alpha^{-1}$ is the attenuation length for hydrogen like localized wave function. As essentially pointed by Mott, there is a competition between hopping distance $r$ and mismatch energy $W$ [78]. By assuming constant density of states near the Fermi level, equation 3.1 can be obtained.

3.1.2 Efros-Shklovskii (ES) VRH

In Mott's derivation, electron-electron correlation was ignored. Later Efros and Shklovskii modified equation 3.1 in 3-D case from $T^{-1/4}$ to $T^{-1/2}$ by taking account of this issue. It was shown that the density of states quadratically vanished at the Fermi level, which means a soft Coulomb Gap was formed [79]. In many disordered systems, both types of VRH mechanisms may be seen. The cross-over happens when the break of the Coulomb Gap by thermal energy is present [80, 81]. Here we found that this kind of mechanisms cross-over is not the only explanation for the experimental observation. When the temperature dependent pre-exponential factor in equation 3.1 was considered, temperature dependent resistivity curve could also be fitted well in $TiO_2$ thin film system.

**3.2 Sample preparation and characterization**

Epitaxial $TiO_2$ films were deposited by PLD on single crystal $LaAlO_3$ (LAO) substrate. The target was made by pressing and sintering $TiO_2$ (99.999% purity) powders. During the experiment, a lambda Physik pulsed laser ($\lambda$ = 248 nm) with energy density of 2 J/cm$^2$ and a frequency of 5 Hz was used for ablating the target. The base pressure was kept at $5\times10^{-7}$ Torr for all the depositions. Half an hour deposition typically gives 100nm thick films, which was measured by Step Profiler and also confirmed by RBS. XRD data show the anatase phase of the films, as shown in Fig. 3.1, except the LAO peaks, only anatase (004) and (008) peaks can be seen.

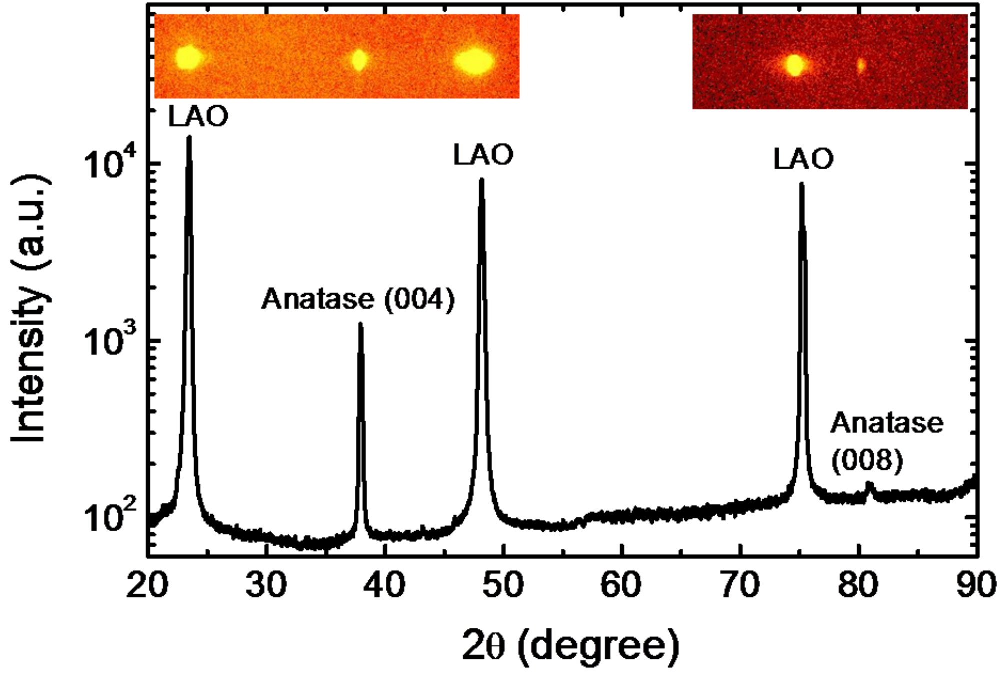


**Figure 3.1: XRD spectrum of pure anatase $TiO_2$ deposited onto LAO (100) substrate. Bright spots in two dimensional detection systems indicate the single crystallites of the film and substrate.**

### 3.3 Transport properties and magneto-resistance (MR) studies

3.3.1 Theoretical mobility and MR in the range of VRH conduction

In the Drude model, the Hall resistance is inversely proportional to the charge carrier density. However, in quantum mechanical phonon assisted hopping regime, this simple relation may be no longer valid because it is difficult to confirm the existence of the transverse voltage built by field induced force on charge carriers in simple Drude system [82]. Holstein is the first person who showed a non-vanishing Hall coefficient in the impurity conduction regime [76]. He proposed a virtual impurity site beside the origination and destination impurity sites. Quantum interference would occur between the direct path from origination to destination impurity sites and the indirect path, which passing through the virtual site. Theoretical work showed a weak Hall effect. After that, Gruenewald calculated the Hall mobility in Mott VRH regime by applying percolation theory [83]. According to their calculation, mobility $\mu_H$ satisfies the following equation:

$$\ln \mu_H \propto -\frac{3}{8}\left(\frac{T_0}{T}\right)^{1/4} \tag{3.3}$$

where $T_0$ is the same constant in equation (3.1).

The change of resistance in presence of magnetic field is an important quantity to characterize a material's conduction property. Qualitatively, in hopping regime, MR should be positive as the magnetic field will squeeze the wave functions in the transverse direction and hence the overlap of the wave functions in transport direction is decreased. Mikoshiba is the first theorist who showed the exponential dependence of resistivity on magnetic field in n-type Germanium [84]. Later Shklovskii derived equations by applying percolation theory to explain the large MR in VRH regime [79]. In Mott's case, i.e. with constant density of states, whence the weak field MR should be of the form:

$$\ln(MR+1) = \gamma H^2 T^{-3/4} \tag{3.4}$$

where γ is a constant and H is the magnetic field.

In the situation when the density of states is governed by the Coulomb gap, equation 3.4 will be modified as:

$$\ln(MR+1) = \gamma' H^2 T^{-3/2} \tag{3.5}$$

where γ' is a constant different from γ.

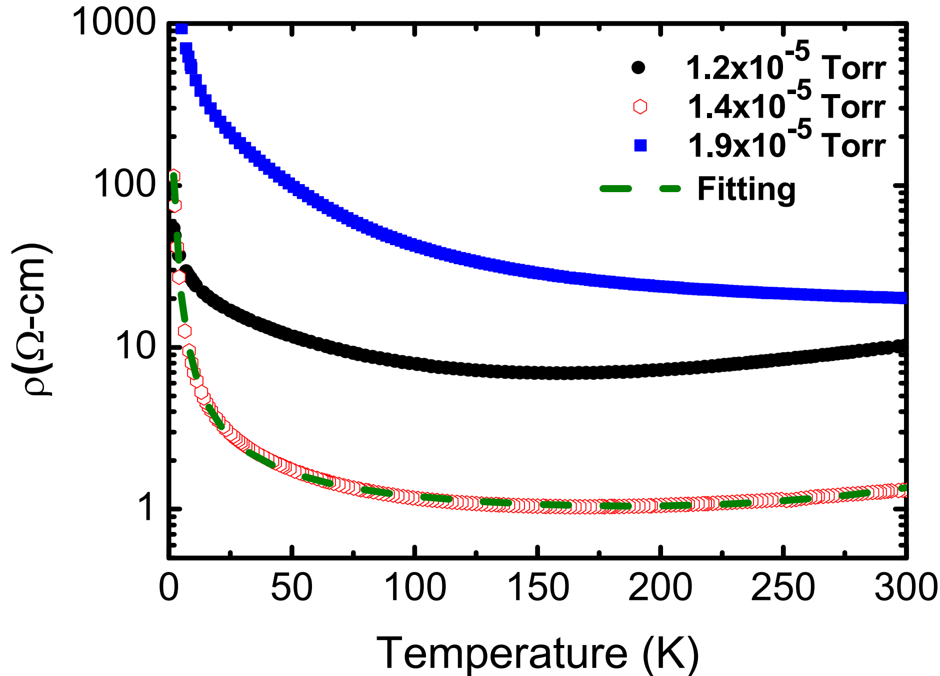


**Figure 3.2: Temperature dependent measurement of resistivity for samples prepared under deposition temperature 700°C and oxygen partial pressure $1.2\times10^{-5}$ Torr, $1.4\times10^{-5}$ Torr and $1.9\times10^{-5}$ Torr respectively. The green dash line indicates the curve fitting.**

3.3.2 Experimental results

Temperature dependent resistivity of samples prepared under 700°C and with different oxygen partial pressures are shown in Fig. 3.2. The resistivities of the films for pressures above 10-4 Torr are too large to be measured by our system. As can be seen, for the sample prepared at $1.4\times10^{-5}$ Torr, the resistivity firstly decreases with decreasing temperature from 300 K and then performs in the opposite way. As shown in Fig. 3.3(a), the resistivities of the samples were plotted with temperature according to Mott's VRH formula (equation (3.1)). Equation (3.1) was satisfied over a large range of temperatures for all three samples in Fig. 3.2, particularly for the sample prepared under $1.4\times10^{-5}$ Torr oxygen partial pressure. The charge transport mechanisms for samples prepared under oxygen partial pressure $1.2\times10^{-5}$ Torr and $1.9\times10^{-5}$ Torr are not fully fitted by VRH. At first glance, the situation of the $1.4\times10^{-5}$ Torr sample should be similar, as we can see the changing of the slope of the straight line indicated by the carmine dash line. However, this change in slope can be omitted when the temperature dependent pre-exponential factor is taken into consideration [85], as shown in the inset of Fig. 3.3(a). An alternative to the temperature dependent pre-exponential factor is the cross over from Mott VRH to ES VRH. Using an approach which treats the pre-exponential factor as constant [86, 87], Mott and ES VRH formulas can be combined as

$$\rho = \rho_0 \cdot \exp\left[\left(\frac{T_0}{T}\right)^v\right] \tag{3.6}$$

where, the exponential factor $v$ may separate the Mott VRH from ES VRH. Mathematically, a function $w$ $(T)$ can be built as:

$$w(T) = -\frac{d\ln\rho}{d\ln T} = v\left(\frac{T_0}{T}\right)^v . \tag{3.7}$$

Then the value of $v$ can be obtained by making a linear regression fit to the log $[w\ (T)]$ versus log $(T)$, where the slope of the plot is equal to $-v$ (derivation is shown in appendix 1). As shown in Fig. 3.3(b), a changing of $-v$ value can be observed, which may indicate a cross over from Mott VRH to ES VRH with further decrease in temperature. The transition temperature is around 20 K. As both the temperature dependent pre-exponential factor and the VRH transition can be used to explain the data, the charge transport mechanism below 20 K

remains an open question.

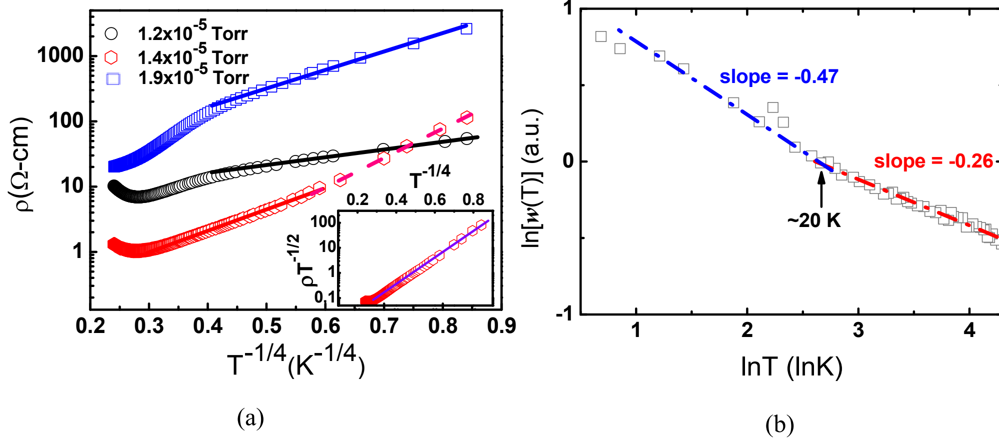


**Figure 3.3: (a) Plot of resistivity with temperature by Mott VRH theory. Inset is the plot by taking considering the temperature dependent pre-exponential factor. The dash lines were guided by eyes. (b) Mathematical way to distinguish Mott VRH and ES VRH, as described in text. The dash lines were guided by eyes.**

The metallic part of the resistivity at temperature above the resistivity minimum can be fitted quite well with the formula considering the electron phonon scattering. By taking the following formula, which covers the metallic and insulating range, the resistivity data of the sample prepared under oxygen partial pressure $1.4\times10^{-5}$ Torr can be fitted with low error, as shown in Fig. 3.2 by the green dash line.

$$\rho = A\cdot T^5 + B\cdot T + C\cdot \exp\left[\left(\frac{T_0}{T}\right)^{1/4}\right] + D \tag{3.8}$$

where *A, B, C, D,* and $T_0$ are constants (values can be found in appendix 2). The metallic to insulating transition temperature depends on those constants. Approximately, it decreases with the room temperature resistivity of the samples, although there are no obvious theoretical reasons behind this.

By comparing the absolute resistivities of the samples prepared at different pressures, as shown if Fig. 3.2, a sharp resistivity minimum is seen at a partial pressure $1.4\times10^{-5}$ Torr. For the samples prepared with 650°C and 750°C, the resistivity minimum located quite close to this pressure as well and the minimum resistivity values shifted with deposition temperatures systematically, as shown in Fig. 3.4. As is well known, oxygen vacancies are donors in $TiO_2$. Increasing oxygen vacancies would increase the charge carrier densities and the conductivity [58, 88], in disagreement with the present

experimental results. To investigate the validity of the results, a statistical study was done, especially for the samples prepared under 700°C. As shown in Fig. 3.4, resistivities of more than ten samples at room temperature were plotted as the function of oxygen partial pressure within a narrow pressure range. Although this data is shown only for room temperature a similar behavior is observed over the whole temperature range. Obviously there is a valley in the plot, which indicates the minimum resistivity of the samples. A similar valley was observed in reduced rutile $TiO_2$ bulk crystal, where the resistivity minimum was correlated to the change in the defect structures [89]. In that system, the charge donor was recognized as Ti interstitials and over reducing the sample will format the planar defect and clustering the donor centers. The carrier densities of the samples in this system under this preparation condition are well below the Mott limit which is close to $5\times10^{18}$ $cm^{-3}$ (assuming an electron effective mass of 1 and a dielectric constant of 31) [90, 91]. Hence the electron transport is through hopping and this will depend on the number of carriers and also the number of hopping sites which will be most likely compensating centers arising from cationic defects [77]. In oxides such as $TiO_2$ it has been observed that oxygen vacancies increase with decreasing pressure and compensating defects increase with increasing oxygen pressure [92]. Hence a cross-over is expected where the highest hopping conductivity will be seen which in this case corresponds to $1.4\times10^{-5}$ Torr. As can be seen in Fig. 3.4, for the samples prepared under 700°C, small changes of the oxygen partial pressure can induce huge changes of the resistivity exceeding almost two orders of magnitude over a 50% change in pressure. This may be because the electron hopping probability exponentially depends on the distance between the two hopping sites which is oxygen pressure dependent [77].

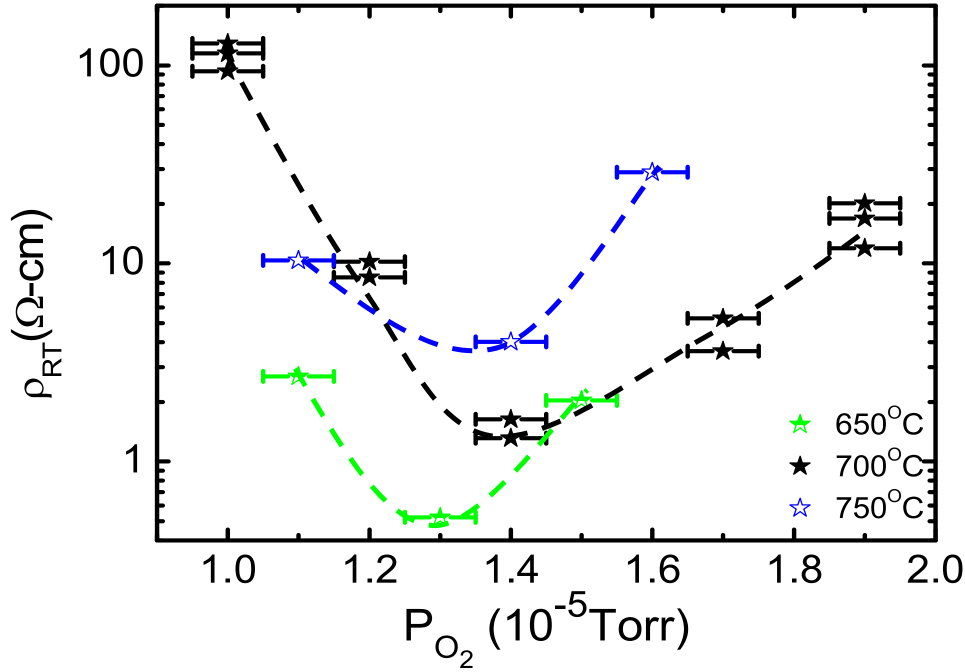


**Figure 3.4: Statistical study of the room temperature resistivity of the samples prepared with different oxygen partial pressure.**

In many spintronic applications magnetic fields are used. It will thus be important to understand the MR behavior of these VRH insulators. As shown in Fig. 3.5(a), MR in transverse geometry at 2 K and 5 K is positive; however, it changes sign to negative when the temperature was above 10 K. In this measurement, *H* // [001], *J* // [010], as shown in Fig. 3.5(b), *H* is the direction of applied magnetic field, *J* is the direction of the current density and [001] is the direction perpendicular to the plane of the sample. Interestingly, at 8 K, it is negative at low field and then changes to positive at high field, as a result of the superposition of two curves with different signs. The negative MR could be explained by the theory of quantum interference (QI), which occurs between the initial and final states during the hopping paths. This theory has been applied in many other systems in the VRH regime quite successfully [93, 94]. The positive MR could be explained by the theory developed by Shklovskii, as already introduced in section 3.3.1. As can be seen, the positive MR depends on both the magnetic field and the temperature. The relatively large variations of MR from 2 K to 5 K and above are identical to the theory. Of course the scattering of the hopping electrons by impurity centers might participate as well, as suggested by Kitada [88]. Qualitatively, MR induced by

QI and shrinkage of the electron wave function both decrease with increasing temperature though the latter has the major influence. This can be used to explain the changing behavior of MR with increasing temperature, which goes from large positive value to large negative value and then approaches zero. Interestingly, cubic polynomials are enough to fit all the experimental curves in Fig. 3.5(a) (fitting details can be found in appendix 3), which was the result of the combination of the mechanisms indicated above.

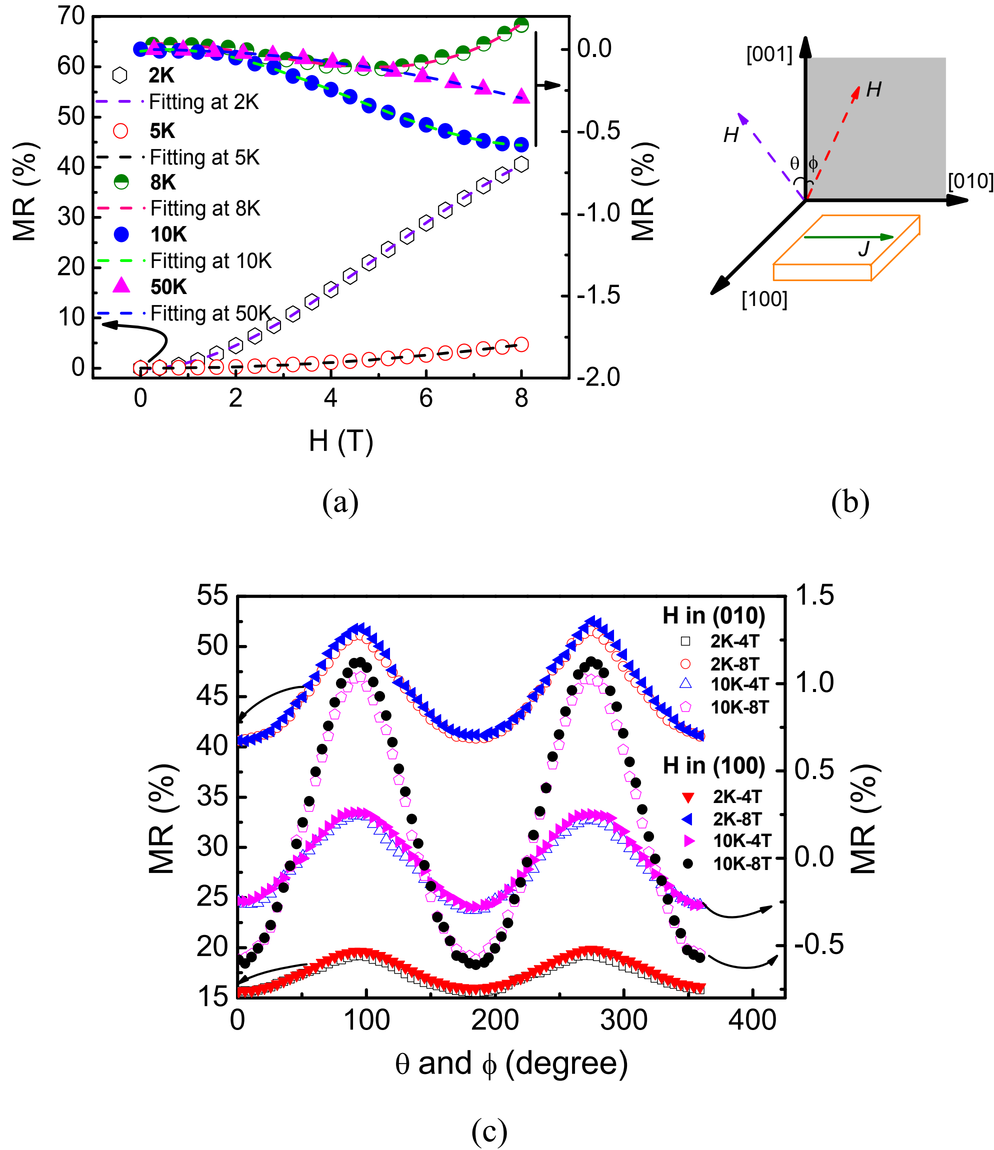


**Figure 3.5: (a) Transverse MR of the sample prepared under oxygen partial pressure 1.4×10$^{-5}$ Torr at different measurement temperatures. The arrows indicate the corresponding axis for the data measured at different temperatures. The dash lines are fitted to cubic polynomials. (b) Schematic diagram showing the MR measurement. (c) Angular dependent MR of the same sample under different temperatures and magnetic fields. Rotation angles were described in (b) and the arrows indicate the corresponding axis for the data.**

Angular dependent MR was measured at different fields and temperatures for the film, as shown in Fig. 3.5(c); they are almost identical whether $H$ is rotated in (010) or (100) planes. The anisotropic MR could be fitted with a cosine function with the same period, but different amplitude. The anisotropy is a well-known factor induced by quantum interference arising from orbital effect. A similar phenomenon was observed in other systems, where QI was the dominant mechanism in VRH regime [95].

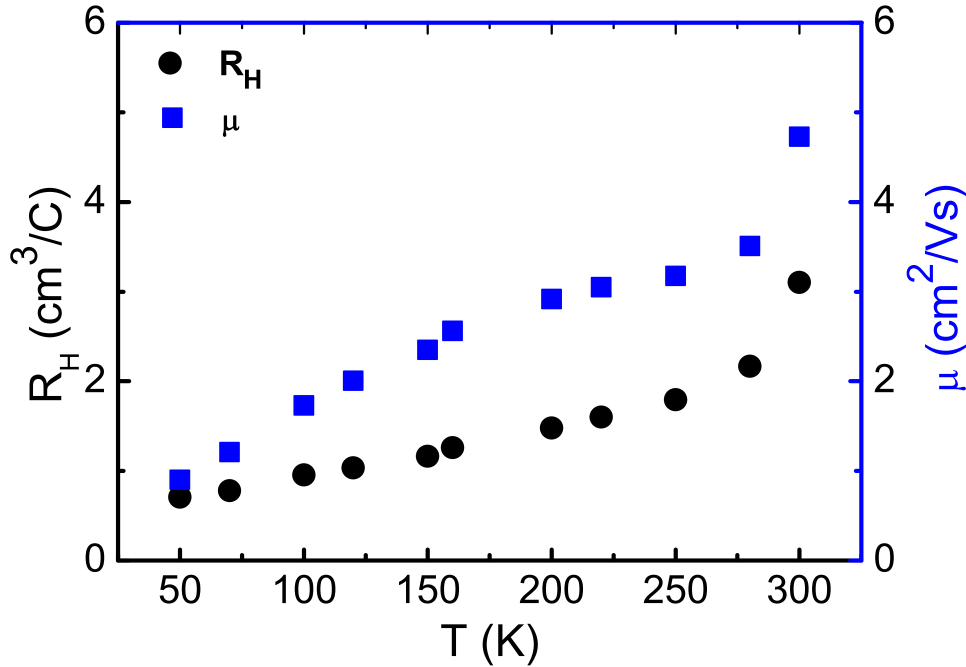


**Figure 3.6: Hall coefficient (left axis) and mobility (right axis) measurement above 50 K for the sample prepared under oxygen partial pressure $1.4\times10^{-5}$ Torr.**

As discussed above, VRH is involved in the whole measurement temperature range although it dominates the transport at low temperature. To investigate, normal Hall effect measurement was done. Although a simple Drude model relates the Hall coefficient $R_H$ and charge carrier mobility is not valid in VRH regime anymore, abnormal $R_H$ plot strongly suggests non-CB transport mechanism [96], as can be seen in Fig. 3.6, where both $R_H$ and $\mu_H$ increase with temperature. Qualitatively, $\mu_H$ follows this theory but the quantitative discrepancy between the experimental value and theoretical expectations probably comes from the large scattering in high temperature. The Hall measurement below 50 K was difficult to obtain due to enhanced fluctuations in the data, may be a characteristic of VRH system.

### 3.4 Summary

In summary, we have shown the discovery of an anomalous resistivity minimum in a $TiO_2$ film prepared at different temperatures and pressures. The resistivity is a very sharp function of oxygen pressure. In most of the pressure range the transport is VRH though below 20 K it is difficult to differentiate between Mott and ES's mechanism. MR of the sample prepared at $1.4\times10^{-5}$ Torr is positive at low temperature (for VRH) but negative beyond 10K indicating quantum interference effects further supported by angle dependent MR measurements.

# Chapter 4 Tailoring the bandgap of anatase $TiO_2$ by cationic dopant Ta and study of the shift of flat band potential by applying Mott-Schottky equation

As has been introduced in chapter 1.3.2, the anatase phase has indirect bandgap, valued as 3.2 eV theoretically. The valence and conduction band edges are contributed by $O_{2p}$ and $Ti_{3d}$ orbital. Now if we intentionally replace certain amount of Ti by larger ionic radius element, like Ta, the changed periodic potential should enlarge the bandgap. In addition, Ta has 5 outer shell electrons, which will contribute an extra electron compared to Ti after the replacement. Then the charge carrier density in the doped film will be more than in pure $TiO_2$. In that case, how is the Fermi level expected to vary with Ta concentration?

## 4.1 Blue shift of optical bandgap of $TiO_2$

Experimentally, UV-vis spectrum gives an estimation of the optical bandgap of materials with the help of Tauc plot [97]. Depending on the type of the bandgap (direct and indirect), Tauc plot has different forms. For the direct bandgap (CB minimum and VB maximum are located at the same momentum point), the following formula should be applied.

$$(\alpha h\nu)^2 \propto (h\nu - E_g) \tag{4.1}$$

where $\alpha$ is the absorption coefficient, described in section 2.3.1. $h\nu$ is the photon energy and $E_g$ is the interested optical bandgap.

For the indirect bandgap (CB minimum and VB maximum are located at different momentum points), $E_g$ can be obtained from the following formula

$$(\alpha h\nu)^{1/2} \propto (h\nu - E_g) \tag{4.2}$$

One common effect in doping semiconductor is the blue shift of the optical bandgap. As the Fermi level crosses over the CB minimum (refer to Fig. 1.2(d)), electrons excited from the VB have to occupy the new minimum, hence the optical bandgap is effectively increased, which is known as the Burstein-Moss effect [98, 99]. Kurita described the blue shift of the optical bandgap totally due to this effect [91]. However, we found with Ta doping, the absolute bandgap changes as well. In addition, both of the conduction and VB edges move towards the vacuum level but with the former moving faster accounting for the observed blue shift of the optical bandgap.

The UV-vis spectrum was measured at room temperature. As shown in Fig. 4.1(a), transmission edges of $TiO_2$ films near the violet region shift to smaller wavelength with Ta concentrations, which causes continuing increase of the bandgap in Tauc plot (Fig. 4.1(b)) according to equation 4.2. How to obtain the individual shifts of conduction and valence band edges with Ta concentrations? Here the shift of the Fermi level of anatase $TiO_2$ thin films with Ta doping needs to be considered.

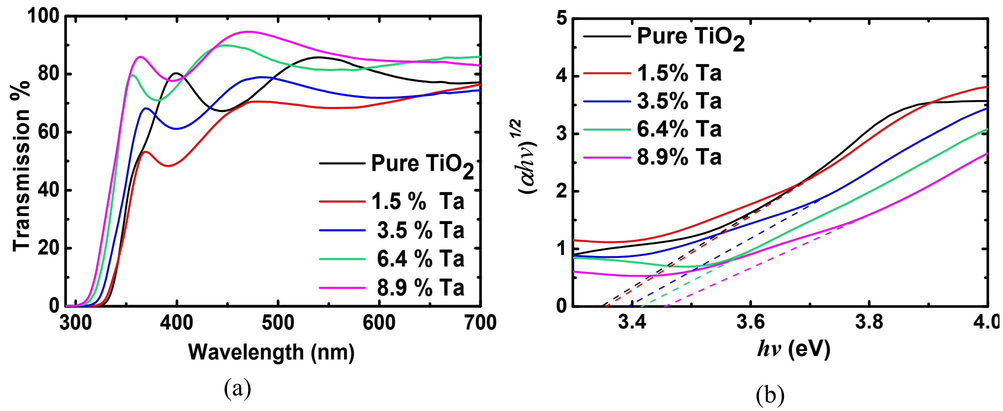


**Figure 4.1: (a) UV-vis transmission spectra of pure and Ta-$TiO_2$ samples. (b) Blue shift of the optical bandgaps of anatase Ta-$TiO_2$ according to Tauc plot.**

### 4.2 Mott-Schottky equation

When an ideal semiconductor (without surface state) is in contact with electrolyte, a semiconductor-electrolyte junction is formed, which is similar as semiconductor-metal junction (Schottky junction) [100]. The electrochemical potential of the electrolyte is similar as the Fermi level of the metal. Therefore, under charge transfer equilibrium, a deplete region (space charge layer) is formed near the junction in the semiconductor side. As shown in Fig. 4.2, when a semiconductor adjacent to a metal under thermal equilibrium, a built in potential ($V_{bi}$) in the deplete region is formed and related to the difference of the Fermi levels of the semiconductor and the metal. The junction behaves like a capacitor which can store positive (or negative) charges ($Q$) in the space charge region of N (or P) type semiconductor. The space charge capacitance ($C$) is then evaluated as $\mathrm{d(Q)}/\mathrm{d(V_{bi})}$

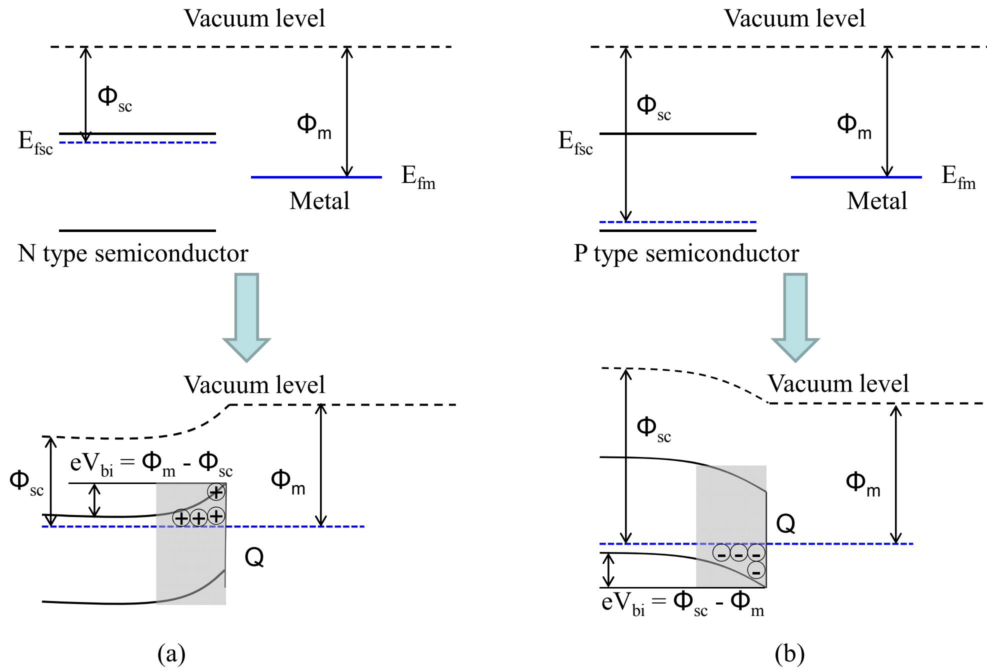


**Figure 4.2: Energy band diagram of a metal in contact with (a) N type semiconductor under thermal non-equilibrium condition (top) or in thermal equilibrium (bottom). (b) P type semiconductor under thermal non-equilibrium condition (top) or in thermal equilibrium (bottom). $\Phi_{sc}$ and $\Phi_m$ are the work functions of semiconductor and metal. $E_{fsc}$ and $E_{fm}$ are the Fermi levels of semiconductor and metal. $V_{bi}$ is the built in potential in the space charge region and e is the elementary charge. Space charge region is shadowed.**

The flat band potential (Fermi level) could be obtained from Mott-Schottky equation (depending on the free charge carrier density, as shown below in equitation (4.3)), which was derived from the Poisson's equation by applying Boltzmann statistics for Schottky barriers at semiconductor/metal and semiconductor/electrolyte heterojunctions with several assumptions, as summarized by Cardon [101]: " (1) the metal or electrolyte and the bulk semiconductor phases have zero resistance; (2) the barrier has perfect blocking properties; (3) no surface states are present; (4) interfacial layers, such as an insulating layer in the semiconductor/metal case or a Helmholtz layer in the semiconductor/electrolyte case, are absent; (5) the dielectric constant is frequency-independent; (6) only one type of localized electronic defect is present, being a completely ionized donor (for n-type) or acceptor (for p-type); (7) the spatial distribution of these defects is homogeneous; (8) the interface is perfectly planar and two dimensionally infinite."

$$\frac{1}{C^2} = \frac{2}{e\varepsilon_0\varepsilon_r N_{sc} A^2}\left(V - V_{fb} - \frac{k_B T}{e}\right) \tag{4.3}$$

where $C$ is the space charge layer capacitance, $\varepsilon_0$ is the vacuum permittivity, $\varepsilon_r$ is the static dielectric constant, $N_{sc}$ is the charge density in the space charge region, $A$ is the exposed area of the sample to the electrolyte, $V$ is the applied potential with respect to reference electrode, $V_{fb}$ is the flat band potential, $k_B$ is the Boltzmann constant, $T$ is the absolute room temperature, and $e$ is the elementary charge of electron.

Although in real cases, some of the assumptions are not sufficiently satisfied, equation (4.3) can still be applied in finding the flat band potential as long as the proportional relation of $1/C^2$ and $V_{fb}$ is valid in a region.

When the charge carrier density of the semiconductor is larger than $10^{19}$ $cm^{-3}$, one cannot apply Boltzmann statistics due to metal-like conducting property with significant carrier degeneracy. Instead, a modified Mott-Schottky equation was derived by applying a more general Fermi-Dirac statistics and is given below [102]:

$$\frac{1}{C^2} = \frac{2}{e\varepsilon_0\varepsilon_r N_{sc} A^2}\left(V - V_{fb} - \frac{2}{5}\frac{E_F}{e}\right) \tag{4.4}$$

where $E_F = \frac{\hbar^2 (3\pi^2 N)^{2/3}}{2m^*}$ is the Fermi level energy and $m^*$ is the effective electron mass. It should be noted that the difference in the flat band potential using equations (4.3) and (4.4) is negligible when free charge carrier density is smaller than $5\times10^{20}$ $cm^{-3}$.

**4.3 Experimental section**

Single crystal $Ti_{1-x}Ta_xO_2$ ($x$ = 0.0, 0.015, 0.035, 0.064 and 0.089) films were deposited by PLD technique on single crystal (001) LAO substrates. The PLD targets were prepared by solid-state reaction of 99.999% pure $TiO_2$ and 99.995% pure $Ta_2O_5$ powders (bought from Sigma Aldrich Co.). Energy density of the laser is around 2 $J/cm^2$ and the frequency is 5 Hz. The oxygen partial pressure during deposition was maintained at $1\times10^{-5}$ Torr with chamber base pressure below $1\times10^{-6}$ Torr and the deposition temperature was maintained at 700°C. The deposition lasted one hour with 5 Hz laser frequency giving around 200 nm thick films. After the deposition, all the samples were annealed in

atmosphere at 500°C for 1 hour to minimize the effect of oxygen vacancy.

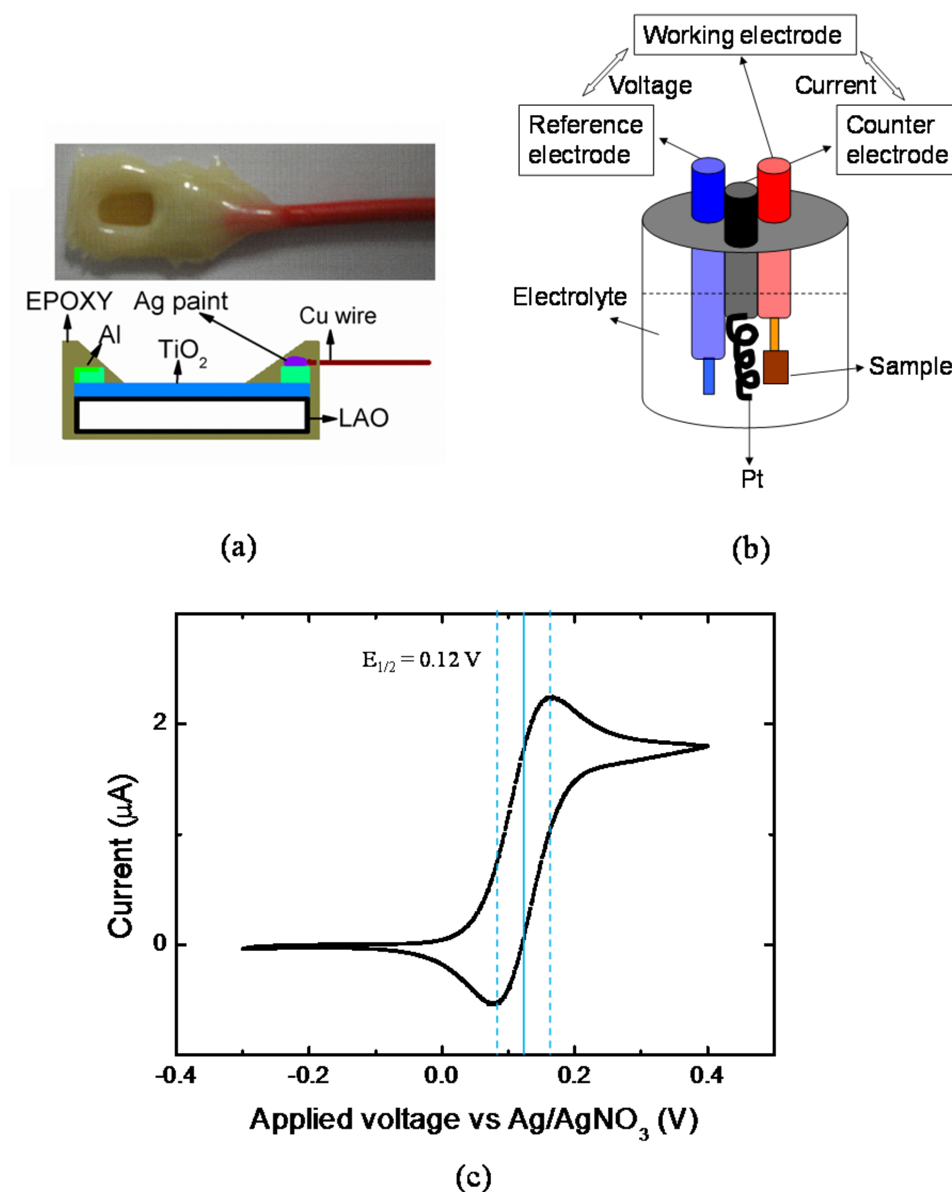


**Figure 4.3: (a) Real image and schematic graph of the working electrode used in EIS measurement. (b) Schematic graph of three electrodes setup. During measurement, current is applied between working and counter electrodes and voltage is measured between working and reference electrodes. (c) Calibration of the potential of the $Ag/AgNO_3$ reference electrode with respect to Ferrocene (1mM in 0.1M TBAP-acetonitrile solution) by CV measurement.**

The crystal quality of the films is examined by XRD and RBS operated in random and channeling modes. During the RBS experiment, first we aligned the [001] axial location of the target with the incident beam direction, and found the random direction by tilting away from any minor axes and planes near the [001] major axis. After that, the RBS spectra at both aligned and

random cases were collected. SIMNRA [103] simulation package was used to fit the random spectra of our films and the thickness information was obtained in "nm" by dividing the atomic mass density of $TiO_2$ from the areal density obtained from RBS. The EIS measurements were carried out using these well-characterized Ta incorporated $TiO_2$ single crystal films on the LAO substrate. As shown in Fig. 4.3(a), the top of film was covered by a 100 nm thick aluminum layer deposited by thermal evaporation leaving the central part uncovered. A Cu wire was connected to the Al contact pad by silver paint. Then the pads were covered by EPOXY for an electric isolation.

For the EIS measurement, a three electrodes configuration was used, as shown in Fig. 4.3(b): the working electrode was the $TiO_2$ sample (Fig. 4.3(a)); the counter electrode was a Pt wire and the reference electrode was made of 0.01 M $AgNO_3$/Ag, 0.1 M Tetrabutylammonium perchlorate (TBAP) dissolved in anhydrous acetonitrile (99.9% pure). The potential of the reference electrode was calibrated relative to Ferrocene using cyclic voltammetry (CV) measurement. The obtained $E_{1/2}$ of Ferrocene is around 0.12 V with respect to Ag/$AgNO_3$ reference electrode and was stable during the experiment, as shown in Fig. 4.3(c). The electrolyte used in the present experiment was 0.1 M TBAP in anhydrous acetonitrile (99.9% pure). The impedance measurements were carried out with a potentiostat equipped with a frequency response analyzer (AUTOLAB PGSTAT302N) in the frequency range from 0.1 Hz (0.01 Hz for the pure $TiO_2$ sample) to $10^5$ Hz.

**4.4 Experimental results and discussion**

XRD patterns of all the obtained films are similar as Fig. 3.1, which confirms the formation of anatase phase only. Besides the signals come from the substrate, only anatase (004) and anatase (008) can be seen in the spectrum. The $TiO_2$ films for all Ta concentration showed pure anatase phase and after annealing in atmosphere they showed good stability over a period of six months. In the RBS spectrum (Fig. 4.4), the Ta peak is separated from La and Al (from substrate), Ti (from film) and oxygen edges due to their atomic mass differences, from which, Ta concentration can be simulated accurately. RBS-Channeling spectra of these samples, as depicted in Fig. 4.4, clearly shows a low channeling $\chi_{min}$ for Ti and La (~2%) which implies that the Ti is

epitaxially aligned with the substrate. Almost all Ta ions were uniformly substituted (channeling minimum yield 2.5%) in the Ti lattice. The typical thickness of the films was found to be about 200 nm. The amount of Ta concentration in the films was determined and plotted in the inset of Fig. 4.4 as a function of nominal Ta concentration in the PLD target. The measured RBS film concentration of Ta deviated systematically within 10-20% of the nominal target concentration but in our subsequent data we used only the Ta concentration measured by RBS.

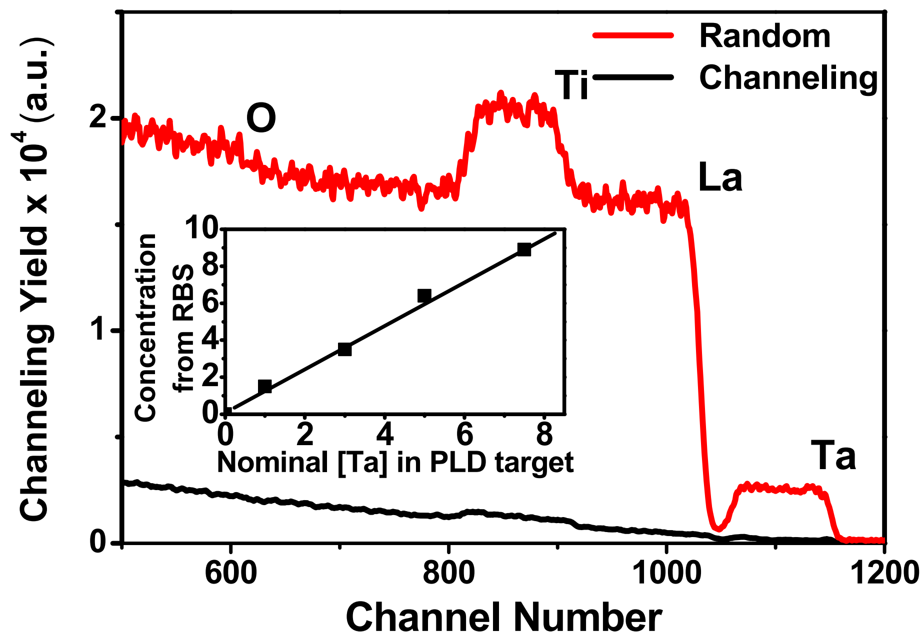


**Figure 4.4: Random and channeling spectra of 6.4% Ta-$TiO_2$ film showing excellent channeling yield. Ta concentration measured by RBS versus nominal Ta concentration in the PLD target is shown in the inset.**

Fig. 4.5 shows the temperature dependent resistivity of various Ta incorporated films. As can be seen, pure $TiO_2$ film shows semiconducting behavior (inset), which means that resistivity decreases with increasing temperature. The plot is different from Fig. 3.2 in chapter 3 because the sample preparation conditions are different. Here post air annealing of the film after deposition is proceeded to minimize the effect of oxygen vacancies which is crucial for the studies presented in chapter 3. The transport behavior of 1.5% Ta incorporated film suggests metallic nature with resistivity increasing with temperature. The room temperature minimum resistivity was $4.7\times10^{-4}$ Ω·cm, which was obtained with 6.4% Ta-$TiO_2$ film. We can raise a

question from this phenomenon. How much concentration of Ta can cause the transport behavior of $TiO_2$ films to change from semiconducting to metallic? In the next chapter, low concentration Ta doped anatase $TiO_2$ films will be studied.

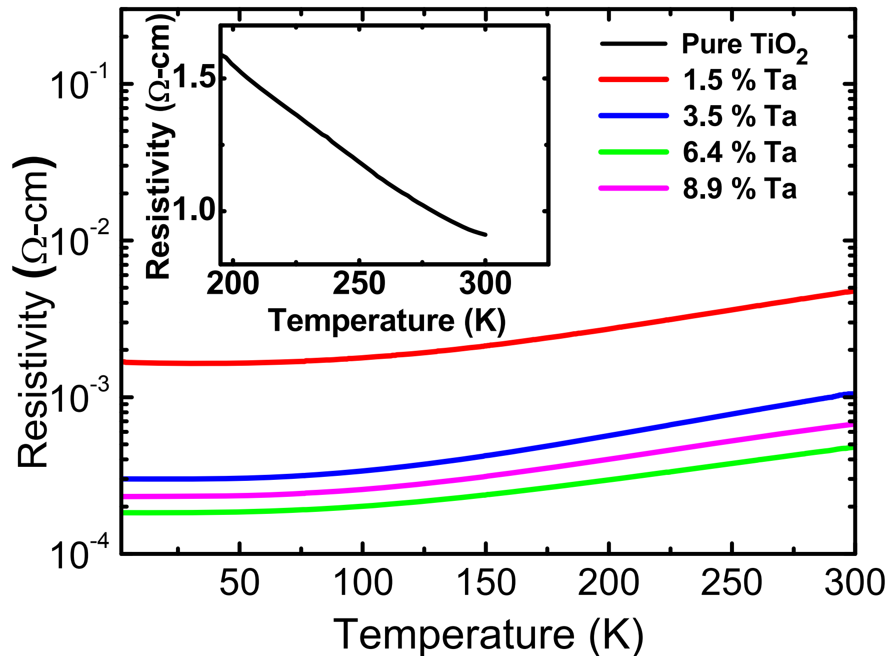


**Figure 4.5: Resistivity versus temperature of Ta-$TiO_2$ films as a function of Ta concentration. Inset shows the pure anatase performance.**

Back to the story, the electrochemical impedance spectra (Nyquist plot) of the pure anatase $TiO_2$ thin film measured at different potentials is shown in Fig. 4.6(a), where a big semicircle is seen in the low frequency range. However, with the magnified spectra (shown in the inset), a much more complex impedance response is seen to develop in the high frequency region. As similar situation was observed with Ta incorporated $TiO_2$ when a thin aluminum layer was deposited to make the electrical contact. However, when the aluminum contact was removed and was replaced by silver paint, only a simple semicircle was seen in the high frequency region. Fig. 4.6(b) shows the impedance spectra obtained from 1.5% Ta-$TiO_2$ without aluminum contact layer (the impedance spectra of 3.5%, 6.4% and 8.9% Ta-$TiO_2$ films are shown in appendix 4). As shown in the inset, besides a big semicircle seen in the low frequency region, a much smaller semicircle with almost constant diameter at different applied potentials can be observed at higher frequency.

The EIS data can be fitted using the software Zview with an equivalent circuit shown in Fig. 4.6(c). Here, $R_1$ represents the series resistance of the circuit. $R_2$ and the constant phase element, ($CPE_1$) arise from the contact of Al or Ag paint with $TiO_2$ film. The $DX_1$ is a transmission line circuit element (Fig. 4.6(c)) comprising of three parts: sheet resistance $R$ of the $TiO_2$ film, the space charge layer capacitance, CPE and resistance $R'$ arising from the leakage of current (this is due to the limitation of current setup, which is operated in air without inert gas circulation). For pure $TiO_2$, the Warburg impedance is unambiguously seen in the intermediate frequency range, indicating a distinguishable electron transport process through the thin films ($R$). A transmission line model was employed to fit the spectra [104, 105]. Evidently the sheet resistance $R$ decreases gradually with the applied forward bias, which can be rationalized based upon the evolution of depletion layer with bias. With increasing forward bias, the height and width of depletion layer shrinks. As a result, charge transport through the film is facilitated. In contrast, as $R$ is much smaller than $R'$ in Ta-$TiO_2$ films, the straight line of Warburg impedance is not distinguishable in the spectra. However, since the space charge layer capacitance was obtained from the low frequency part, the fitting will not be compromised by the different electron transport kinetics in the intermediate frequency range. So the data can be fitted with the simple parallel $R'$-CPE model. To obtain the true space charge layer capacitance value, the obtained CPE capacitance value was then corrected by the following equation [106]:

$$C = T(\omega''_{\max})^{P-1} \quad (4.5)$$

where $C$ is the corrected capacitance, $\omega''_{max}$ represents the frequency of maximum –Z" value on the Nyquist plot, $T$ and $P$ come from the definition of the impedance of CPE, i.e., $Z_{CPE} = T^{-1} / (\omega i)^{P}$. Equation (4.5) is derived from the correction of parallel connection of a CPE and resistor, and used here because the semicircle in the lower frequencies can be simplified as a parallel circuit of a resistor and a CPE. In addition, the two semicircles are separated clearly from each other, as shown in Fig. 4.6(b), which make the fitting more reliable (the fitting parameters of R, R', $T_{CPE}$, $P_{CPE}$, $\omega''_{max}$ are compiled in appendix 5).

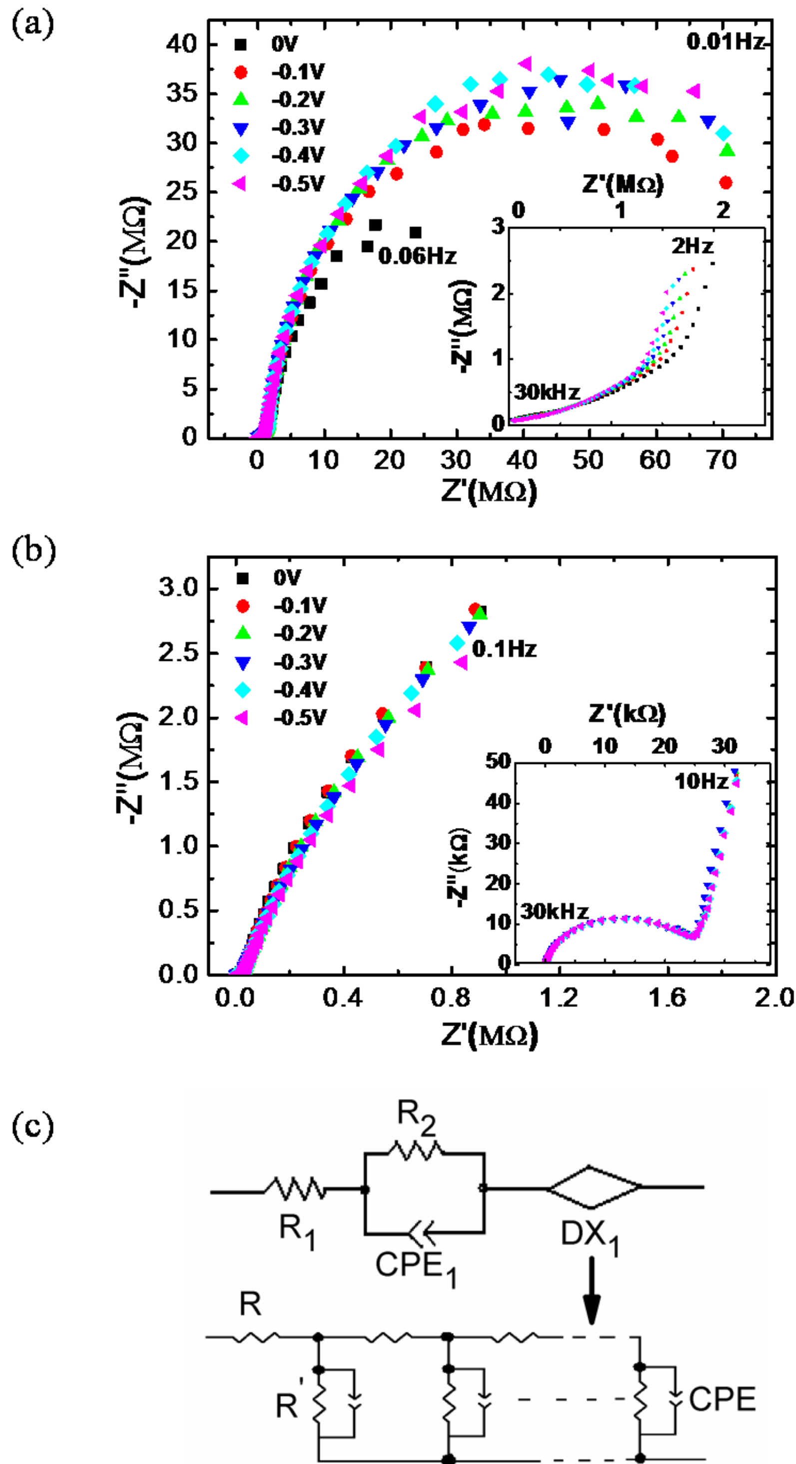


**Figure 4.6: (a) Nyquist plots of pure $TiO_2$ with Al contact layer. The frequency range here is from 0.01 Hz to 30 kHz. The inset graph is in the expanded scale of the high frequency data. (b) Nyquist plots of 1.5% Ta incorporated $TiO_2$ without Al buffer contact layer. The frequency range shown here is from 0.01 Hz to 30 kHz. The inset graph is the expanded scale of the high frequency data. (c) Equivalent circuit of the samples in current EIS measurement.**

The obtained capacitance value from equation (4.5) can be substituted into

Mott-Schottky equations (4.3 and 4.4) according to different charge carrier densities. From the plot, the flat band potentials of the samples relative to Ag/$AgNO_3$ reference electrode can be obtained, as shown in Fig. 4.7, where it is assumed that the space charge layer capacitance is much smaller than Helmholtz layer capacitance and is dominant at low bias voltage [107]. It is clear that the pure anatase $TiO_2$ possesses the least negative flat band potential of ~ -1.08 V (vs. Ag/$AgNO_3$). As the Ta concentration increases, the flat band potential of the sample becomes more negative.

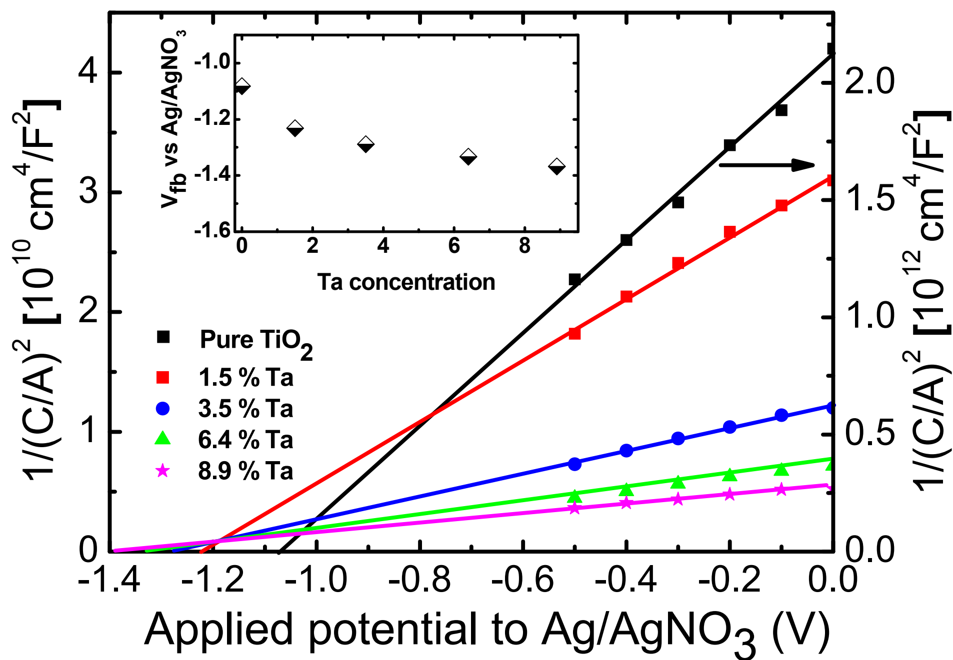


**Figure 4.7: Mott-Schottky plot of the samples. Right y-axis is for pure $TiO_2$, left y-axis is for Ta-$TiO_2$ samples. X-axis is the applied potential to the samples relative to the reference electrode. The straight lines were guided by eyes. The inset is the flat band potential of the samples obtained from the Mott-Schottky equations by considering the applied potential plot.**

The free charge carrier concentration was determined from the slope of the Mott-Schottky plots in Fig. 4.7. With increasing Ta concentration in $TiO_2$, free charge carrier density increases, and as a result the sheet resistance of the Ta incorporated thin films drops gradually. These data are plotted in Fig. 4.8(a) along with those obtained from the Hall effect and direct resistivity measurements. From both the impedance and Hall effect measurements, the free charge carrier density was found to increase with Ta concentration. However, the free charge carrier density determined by Hall effect

measurement becomes larger than that obtained from impedance measurement at higher Ta concentration. The discrepancy between these two measurements is most likely from the change of the static dielectric constant when pure anatase $TiO_2$ films are incorporated with Ta. Since in the impedance measurement we assumed $\varepsilon_r$ of 31 for all the films by reconciling the two carrier density data we may be able to estimate the $\varepsilon_r$ as a function of Ta concentration [108, 109].

As the free charge carrier density can be independently obtained from Hall effect measurement, by substituting it into Mott-Schottky equation the static dielectric constant can be calculated from the equation:

$$\varepsilon_r = \frac{2}{e\varepsilon_0 d_{M-S} N_{SC}^{Hall} A^2} \tag{4.6}$$

where $d_{M\text{-}S}$ is the slope of the linear part of Mott-Schottky plot and $N_{SC}^{Hall}$ is the free charge carrier density determined by Hall effect measurement.

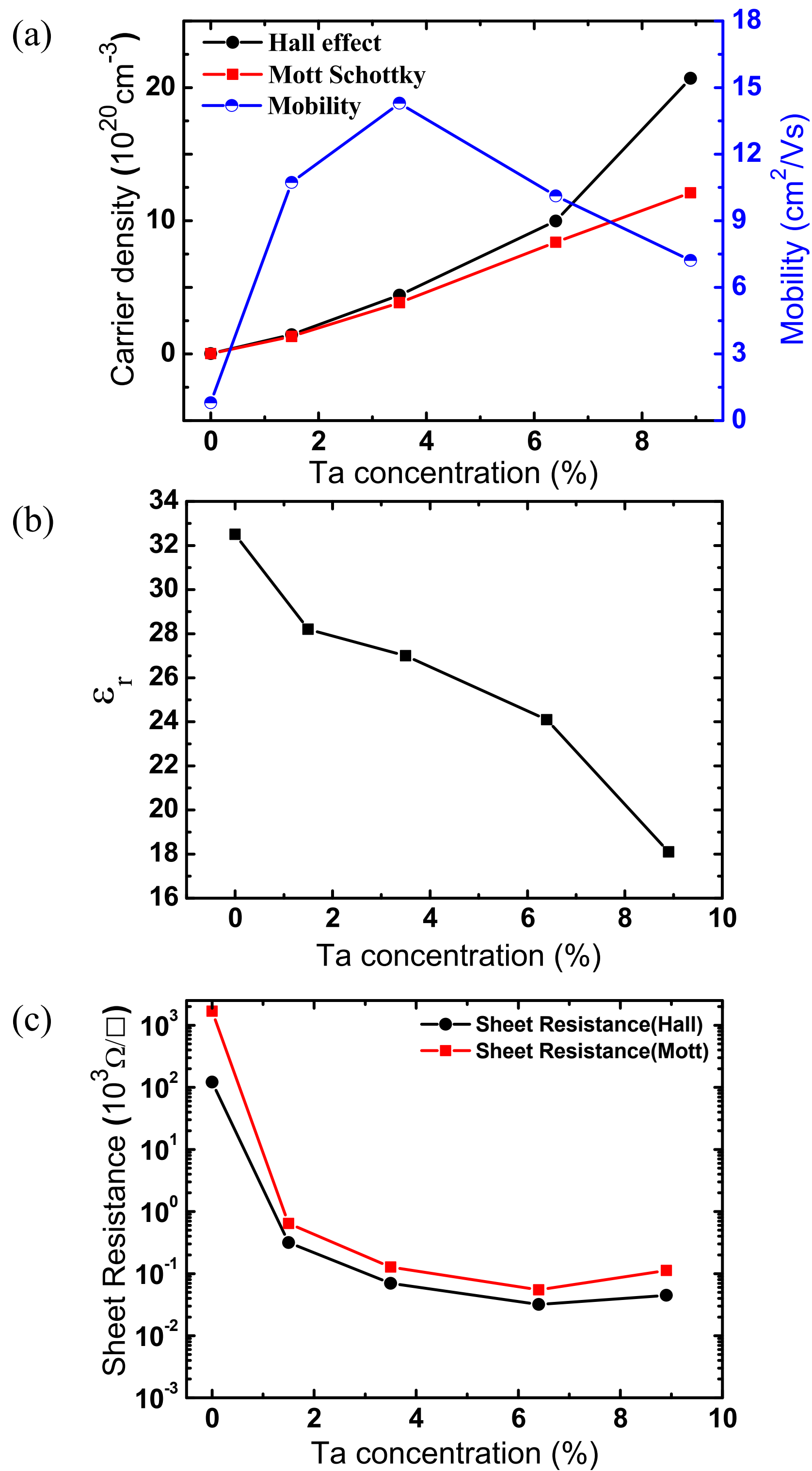


**Figure 4.8: (a) Hall effect measurement of the charge carrier density (black) and mobility (blue) of the samples together with the carrier density of the samples estimated from Mott-Schottky plot (red). (b) Dielectric constant as function of measured Ta concentration calculated by reconciling Hall effect and Mott-Schottky measurements of carrier densities. (c) Comparison of Sheet resistance of the films as function of measured Ta concentration obtained from direct resistivity measurement and from Mott-Schottky plot.**

As revealed in Fig. 4. 8(b), the dielectric constants of the pure and Ta incorporated samples were calculated with equation (4.6). The static dielectric constant of the pure anatase $TiO_2$ was calculated to be ~32, very close to the reported value of 31, which validates the above approach. As Ta atoms were incorporated into the film, the dielectric constant of the sample decreased gradually. In the present experiment, as the space charge layer capacitance was obtained from the low frequency region of impedance spectra, we assume the derived dielectric constant to be approximately the static dielectric constant. In general, the static dielectric constant of insulating material is determined by measuring the capacitance of the insulating materials sandwiched between two metal plates. However, when the material becomes relatively conducting, it becomes difficult to get reliable measurement using low frequency alternating current. Hence the above method of combining Hall effect and Mott-Schottky measurements provides a feasible way of determining the static dielectric constant of metallic material.

The carrier mobility of the samples obtained from Hall measurement can be seen in Fig. 4.8(a), which initially increases with Ta concentration and then drops after it gets to a maximum at about 4-5%. Fig. 4.8(c) shows the sheet resistance obtained from Hall effect measurement showing good consistence with impedance measurement. At room temperature it decreases with increasing Ta concentration and saturates at high Ta concentration. The energy difference between the CB edge and the Fermi level of pure anatase can be approximated by the following equation:

$$\Delta E = k_B T \ln\left(\frac{N_{sc}}{N_c}\right) \tag{4.7}$$

where $N_c = 2\left(\frac{m_c^* k_B T}{2\pi\hbar^2}\right)^{2/3}$ is the effective density of states for the CB. Assuming the effective electron mass $m_c^*$ in anatase $TiO_2$ is 1 $m_0$ ($m_0$ is free electron mass) [90]; the Fermi level at room temperature was estimated to be about 62 meV below the CB edge. To address the movement of the Fermi level and the changes of the rigid bandgap due to Ta incorporation in $TiO_2$ films, the shift of the flat band potential and optical bandgap need to be considered concurrently. If we assume that the VB edge is not moving with Ta

incorporation and that only Fermi level and CB edge are shifting, the observed results become difficult to explain. As can be seen in Fig. 4.9, at 1.5% Ta level, the optical bandgap only blue shifts ~20 meV. However, the Fermi level has shifted ~140 meV. At this level, the sample is already degenerate, which means the excited electron by photons can no longer occupy the lowest state of the CB. Hence the optical bandgap blue shift value should be much larger than 20 meV, which disagrees with the experimental result. So the VB must shift to higher energies to reconcile the difference between the measured movement of the Fermi level and the observed blue shift of the optical bandgap. Based on this assumption, the Ta incorporated $TiO_2$ reaches degeneracy at about 0.8% Ta substitution (at the degeneracy point, the Fermi level and CB edge just overlap).

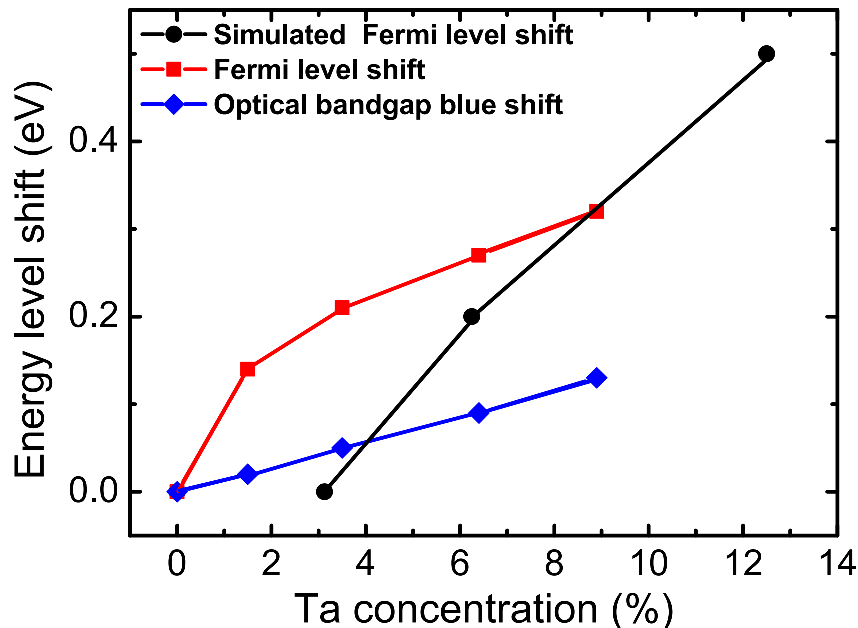


**Figure 4.9: Experimentally obtained Fermi level (red) and optical bandgap blue shift of the Ta incorporated $TiO_2$ samples where pure $TiO_2$ was selected as the reference point (blue), and simulated Fermi level shift with measured Ta doping concentration (black), the shift value of the first point (3.125%) is set as zero for easy comparison.**

### 4.5 Theoretical calculation results

In order to verify whether the above discussion of the shift of Fermi level with Ta concentrations is valid, plane-wave pseudopotential DFT calculations for Ta incorporated anatase $TiO_2$ was performed. The calculation with the Vienna *ab initio* Simulation Package (VASP) code used generalized gradient

approximation with Perdew-Burke-Ernzerhof exchange-correlation functional [110-112]. The oxygen $2s^22p^4$, titanium $3d^24s^2$ and tantalum $5d^36s^2$ are treated as valence electrons. We used the projector augmented-wave (PAW) potential [113], which is generally more accurate than the ultrasoft pseudopotential, and the plane-wave cut-off is set as 500 eV based on convergence test. The Ta concentration is simulated from 3.125% to 12.5% by using $TiO_2$ supercell from 2 × 1 × 1 to 2 × 2 × 2. All the atom positions are allowed to relax until the force acting on each is less than 0.02 eV/Å. Our simulated crystal structure of anatase $TiO_2$ ($a$ = 3.80 Å, $c$ = 9.72 Å) matched well with experimental data ($a$ = 3.78 Å, $c$ = 9.50 Å) [47], which also proved the credibility of our simulation. The band structure and DOS of pure anatase $TiO_2$ is plotted in Fig. 4.10, which shows bandgap of 2.2 eV. Although it is smaller than the experimental value, we believe that it still can give correct tendency after Ta doping. The VB edge of $TiO_2$ mainly consists of O 2*p* orbital, while the CB edge has predominantly Ti *d* orbital. The *d* valence electrons of Ti are mainly transferred to O *2p* orbital due to the electronegativity difference between Ti and O. After incorporating one Ta into Ti site among 2 × 1 × 1 supercell, no intermediate states appear up among $TiO_2$ bandgap, while Fermi level is shifting up to the CB, as shown in Fig. 4.11(a). From the partial DOS it is shown that states near Fermi level are mainly contributed by Ta and Ti *d* orbitals (Fig. 4.11(b)). As Ta possesses one extra *d* electron, Ta substituting Ti will introduce more electrons into the crystal framework. In addition, as Ta is a shallow dopant, its *d* states is not showing up in the bandgap but mixed with Ti *d* states. From the projected DOS of Ta *d* orbitals, it can be seen that the extra electron is mainly contributed by $t_{2g}$ orbitals (Fig. 4.11(c)).

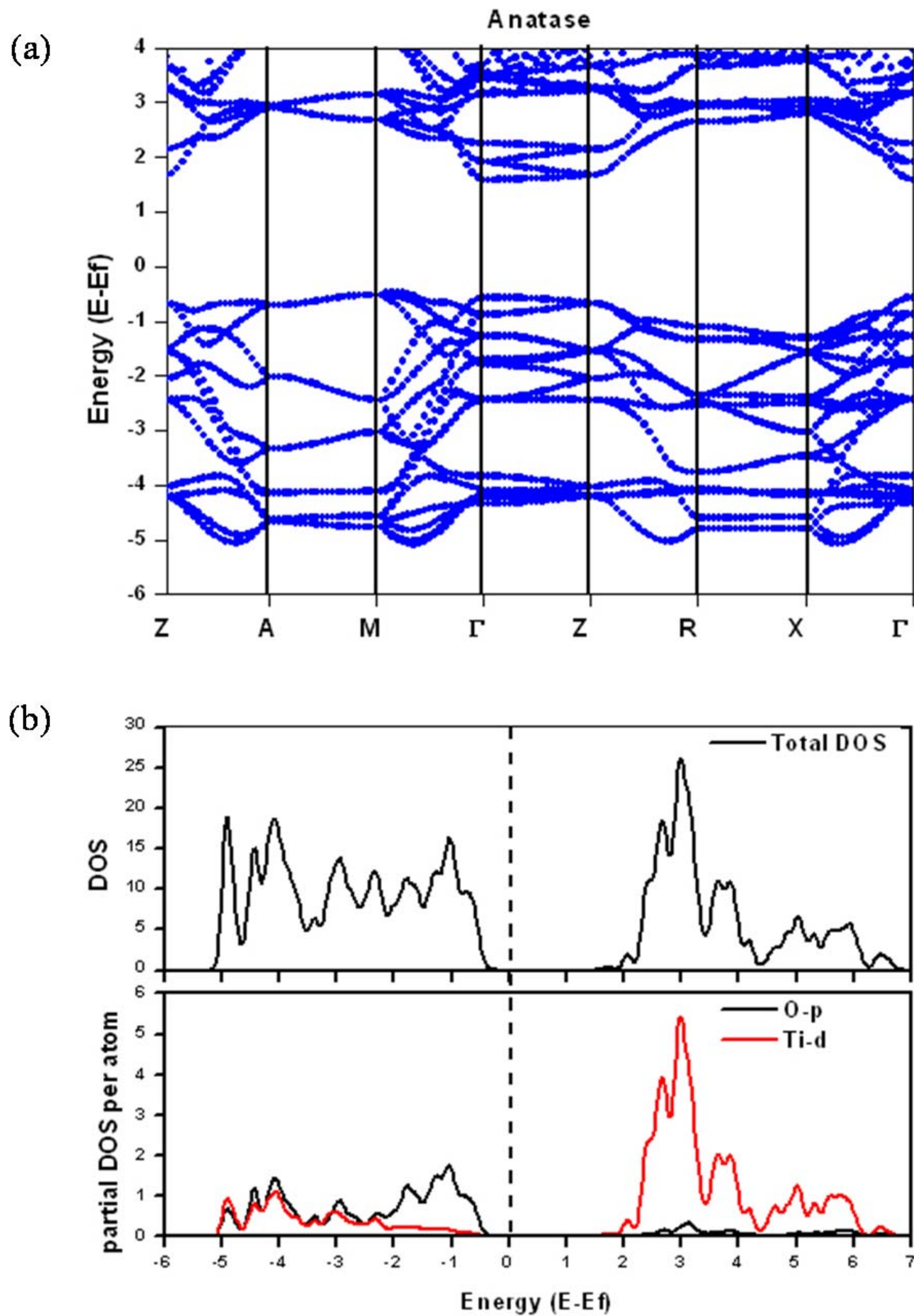


**Figure 4.10: (a) band structure of pure anatase $TiO_2$ (b) Total and partial DOS for pure anatase $TiO_2$.**

The calculated dependency of the Fermi level on Ta incorporating concentrations is plotted in Fig. 4.9. It is clear that more Ta *d* electrons will push the Fermi level higher due to the similar levels between Ta and Ti *d* orbitals.

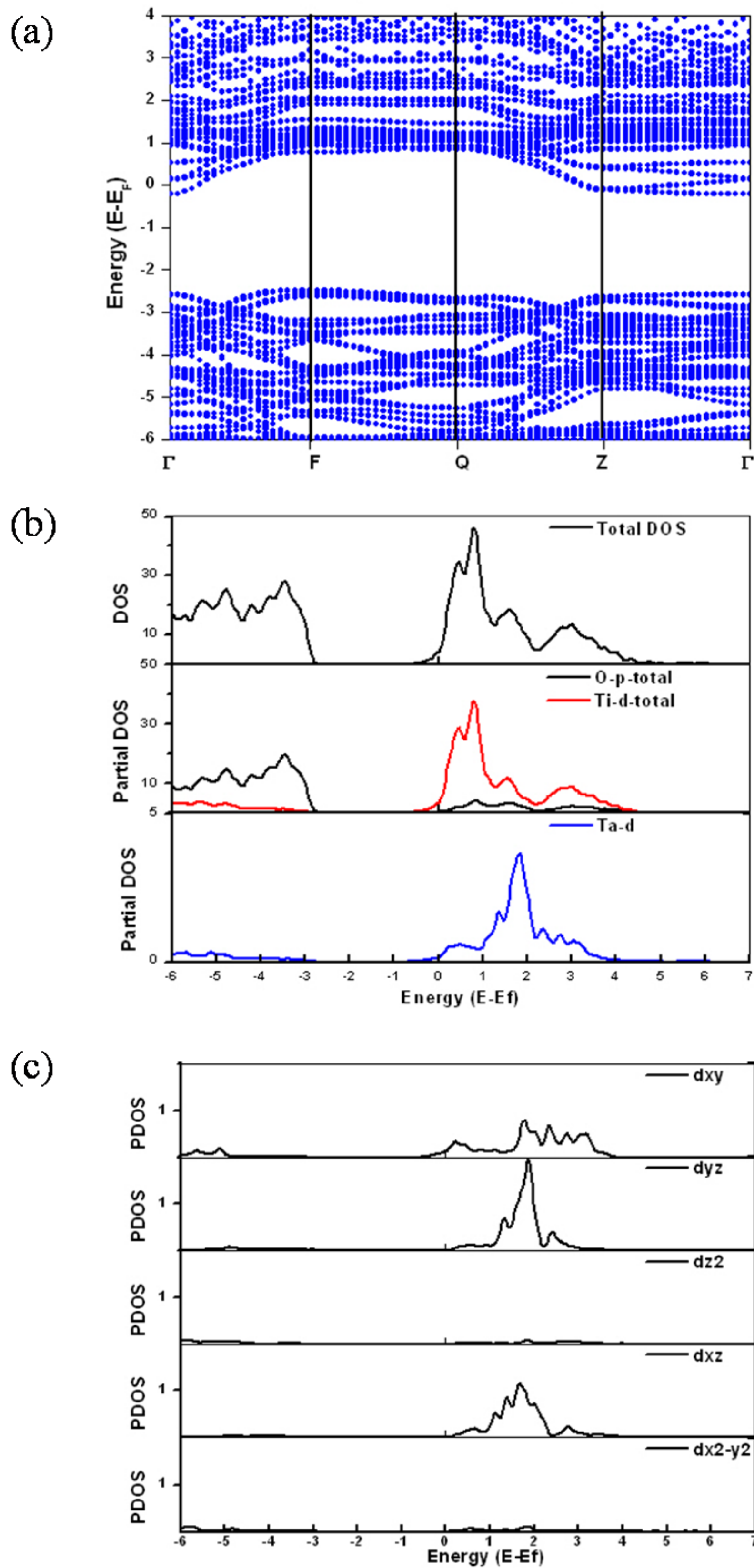


**Figure 4.11: (a) Band structure of 12.5% Ta doped $TiO_2$ (b) Total and partial DOS for 12.5% Ta doped anatase $TiO_2$ (c) Projected DOS of Ta atoms.**

### 4.6 Summary

Continuous shift of the flat band potential of Ta incorporated anatase $TiO_2$ with increasing Ta concentration was observed from the Mott-Schottky plots. The DFT calculation confirmed the continuous shift of the Fermi level. The obtained free charge carrier density and room-temperature sheet resistance are consistent with those obtained from the Hall effect and direct resistivity measurements. The free charge carrier density increases with Ta concentration and the sheet resistance decreases with Ta saturating at higher concentration. By reconciling the carrier density measurements from Hall and Mott-Schottky plot, we were able to estimate the static dielectric constant of metallic Ta incorporated $TiO_2$, a measurement which is difficult to accomplish via capacitive measurements. By considering the blue shift of the optical bandgap together with the movement of the Fermi level, significant movement of the VB was recognized and the formation of the degenerate state at CB was estimated to occur at a Ta concentration of 0.8%.

# Chapter 5 Insulator to metal transition of anatase $TiO_2$ thin film upon low concentration of Ta doping

In chapter 4 we have shown that Ta incorporated anatase $TiO_2$ film has metallic transport behavior while pure anatase $TiO_2$ has semiconductor transport behavior. Also we have estimated the transition occurred at Ta concentration of 0.8%. In this chapter we will study this transition by preparing anatase $TiO_2$ films with low Ta concentration.

## 5.1 Insulator to metal transition

The differences in metal and semiconductor band structures were introduced in Chapter 1. Their transport behaviors are quite different. In general, the resistance of a metallic (semiconducting) system monotonically decreases with reducing (increasing) temperature. The transport property of a material is affected by various parameters such as temperature, pressure, doping, etc., which may be used to cause phase transitions of the material between "metal" and "insulator" [114]. In some cases (e.g. $VO_2$), structure change of a material by ambient environment (temperature, pressure, etc.) causes drastic changes in its transport behavior [115]. However, here we concentrate on two mechanisms which can induce a resistance minimum within a measurement temperature range without any structure changes of the material. One is Kondo effect, which is a consequence of the interactions between a local spin and the spins of the conduction electrons [116]. The other mechanism is weak localization, which is due to the constructive self-interference of the electron's wave function, leading to an enhanced probability for electrons to return to their initial points at low temperatures [117]. The weak localization is compared with the strong localization (described in Chapter 3) which is induced by the random potential. It is shown that at low concentration of Ta the random potential in anatase $TiO_2$ is overcome, which makes weak localization as the dominant transport mechanism in this study.

## 5.2 Kondo effect

In regular metals such as silver, copper, zinc, etc. the resistivity is given by an expression of the form

$$\rho(T) = \rho_0 + AT^5 \tag{5.1}$$

Here the $T^5$ behavior comes from the electron phonon scattering, while the

impurities in the metal give rise to the constant term $\rho_0$. When a small amount of magnetic impurities (iron, manganese, chromium, molybdenum, etc) are present in these metals, the resistivity exhibits a minimum, normally at quite low temperature. The temperature $T_{min}$ at which this occurs varies with the impurity concentration $c$ roughly as $c^{1/5}$. The depth of the resistivity minimum, $\rho(0) - \rho(T_{min})$, is proportional to $c$. Since $\rho(0)$ itself is proportional to $c$, the relative depth of the minimum is roughly independent of $c$ [118]. This phenomenon was satisfactorily explained by Kondo utilizing an antiferromagnetic interaction between the localized spin of the impurity and the spin of the free electrons. The interaction implies the resistivity minimum and below $T_{min}$ the resistivity increases logarithmically with decreasing temperature. As illustrated by Anderson model in Fig. 5.1(a), let us consider an up spin electron with energy $\varepsilon_0$ at the localized impurity state surrounded by the Fermi Sea. The energy needed for the electron to be transited to upper empty energy state is between about 1 and 10 electron volts, which is large for magnetic impurities. In classical physics, this process is impossible unless some energy is put into the system. However, in quantum mechanics, such process may happen within a small timescale $h/|\varepsilon_0|$ (determined by Heisenberg uncertainty principle) as long as another electron tunnels from the Fermi Sea back into the impurity. Such replacement of the electrons may cause the reversal of their spins, which changes the energy spectrum of the system qualitatively (Fig. 5.1(b)). The Kondo resonance state is generated at the Fermi level when many such processes act together. Such a resonance is very effective at scattering electrons with energies close to the Fermi level, which are responsible for the low temperature conductivity of a metal as well [119].

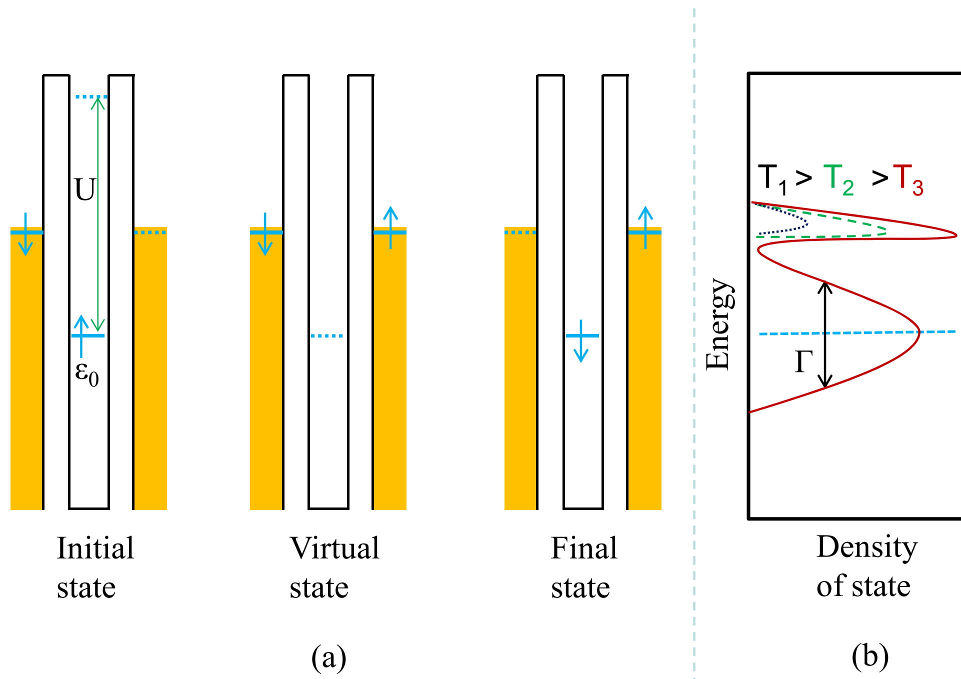


**Figure 5.1: (a) In Anderson model, it is assumed that only one magnetic impurity is surrounded by a Fermi sea, and within the magnetic impurity, there is only one energy state with energy $\varepsilon_0$ been occupied by one spin up electron (blue) below the Fermi energy of the metal (orange). Coulomb energy $U$ indicates the energy needed to add another electron to the state and $|\varepsilon_o|$ is the minimum energy to move the electron from the impurity's state to the Fermi sea. In quantum mechanics, the electron in the impurity's state may tunnel out and stay in a virtual state temporally until the state is occupied by an electron from the Fermi sea. Such process may change the spin of the electron in the impurity's state. (b) Density of states of the combination of many such events described in (a) and the resonance states at the Fermi energy (causing Kondo scattering) with different probabilities can be obtained at different temperatures, (Γ is the width of the impurity's state) showing a decrease in Kondo scattering with increasing temperature [119].**

Kondo's theory predicts an infinite resistance when the temperature approaches 0 K. However, experimental data show the Fermi liquid behavior ($\rho_0 - aT^2$, where $a$ is a constant) [120, 121]. It is accepted that there exists a temperature (called Kondo temperature $T_K$) only above which Kondo's theory can be applied. Below $T_K$, the local spins form bound collective states (Kondo singlet) with the free electrons. In order to flip the local spin, this binding must be broken by the thermal energy of excited free electrons. As the temperature is reduced, this becomes more and more unlikely.

Magnetic field can suppress the spin inversion (dissociate Kondo singlet) and therefore implies negative MR. As the localized spins are random and non-correlated, the effect of magnetic field on the change of resistance should

be isotropic in ideal Kondo systems. The negative MR is logarithmically dependent on the magnetic field in the intermediate region, out of this region, i.e. as the field is approaching 0 Tesla or larger than a value defined as Kondo crossover field $B_K$, it saturates [122].

**5.3 Weak localization**

In disordered electronic system, the electron moves in a diffusive motion. The probability of transporting an electron between two points in space gives the resistivity of the system. When these two points overlap, it represents the probability for the electron to return to the initial location with arbitrary trajectory. As shown in Fig. 5.2, electron may return to the initial point through various ways. Trajectories *C* and *D* are identical but with different directions (they are phase coherent). In classical physics, the total probability for the electron to return is just the summation of probabilities of all the paths. However, in quantum mechanics, paths *C* and *D* may interfere constructively with each other as their wave functions satisfy the time reversal symmetry. The result of the quantum interference is the increasing probability of returning to the starting point for the electron rather than moving forward, which increases the resistance of the system. The precondition of such process is that the electrons have to be phase coherent within a large distance, which is defined as the phase breaking length. This requires the temperature to be low enough in order for the effect to be observable [118]. Theoretically, weak localization may exist in all real dimensions [123]. However experimentally, it is more likely to be observed in two dimensional systems because it is easier for electrons to form self-crossing trajectory in such systems. [124]. In contrast to Kondo effect, although the resistance shows logarithmic temperature dependence in weak localization, it diverges when the temperature approaches zero because all the electrons have been self-trapped [125].

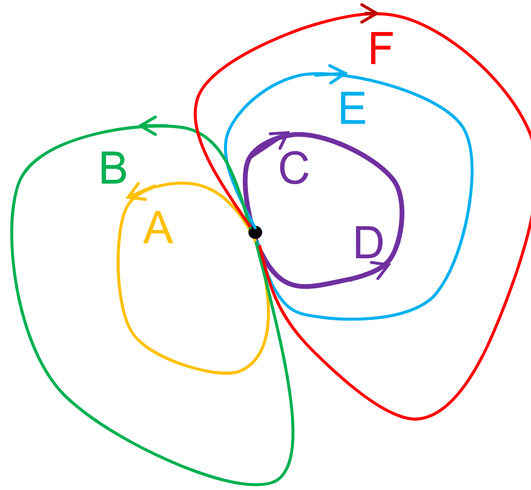


**Figure 5.2: Trajectories of an electron returning to the initial points. *C* and *D* indicate the same trajectory but different directions. Only trajectory *C* and *D* can interference as they are phase coherent.**

The magnetic field $B$ has effects on an electron through two mechanisms, which are classical Lorentz force and quantum mechanical Aharonov–Bohm effect. The former can curve the electron's trajectory and it will be suppressed when the mean free time $\tau$ of elastic scattering is short. The latter will add an extra phase factor to the electron's wave function hence affect the probability of electron's transportation. As a quantum effect, the latter is not limited by any elastic processes. [126]. Weak localization is a quantum process and it is strongly dependent on the phase relation between time-reversed paths. Whenever the phase coherence is broken, the localization is in general suppressed, which leads to enhancement of the conductivity. The time-reversed paths may exist in any orientation in three dimensional cases; as a result the MR of weak localization is independent of the relative directions of the current and the magnetic field. In contrast, the time-reversed paths are confined in two dimensional systems, therefore, only the perpendicular component of the field has effect on the conductance. Hence in 2D systems, the response of the resistance to the magnetic field is highly anisotropic. In addition, the MR is temperature dependent because it is related to the phase breaking time $\tau_{\phi}$, which depends on temperature and much larger than $\tau$ [125].

### 5.4 Experimental results

Single crystal $Ti_{1-x}Ta_xO_2$ ($x$ = 0.001, 0.002, 0.003, and 0.004, which are the nominal compositions of Ta in the targets) films were prepared by PLD on single crystal (001) LAO substrates. The method of making the target and the deposition conditions were the same as those presented in chapter 4. The thicknesses of the films are close to 100 nm, which usually takes half an hour of deposition. XRD data show the pure anatase phase, which is same as presented in Fig. 3.1. The transport property was measured by PPMS and is shown in Fig. 5.3. It can be seen that 0.1% of Ta dopant has reduced the absolute value of $TiO_2$ resistivity by more than one order (comparing Fig. 3.2 with Fig. 5.3(a)) at room temperature. As the temperature reduces, the resistivity keeps decreasing until near around 130 K when it starts to increase. The inset shows the plot with temperature axes in logarithmic scale, where a linear fit below the transition temperature is clearly visible. This transport behavior follows weak localization predictions in two dimensional systems. By increasing the Ta concentration, the samples become more conductive and the resistivity at low temperatures deviates from logarithmic fitting. The saturating resistivity at low temperatures in the logarithmic plot of above 0.2% Ta doped films shows the Kondo – like behavior although more evidences (isotropy/anisotropy of the MR) are needed. From Fig. 5.3(a) – (d), the resistivity minimum shifts towards lower temperatures with Ta concentration, as plotted in Fig. 5.3(e).

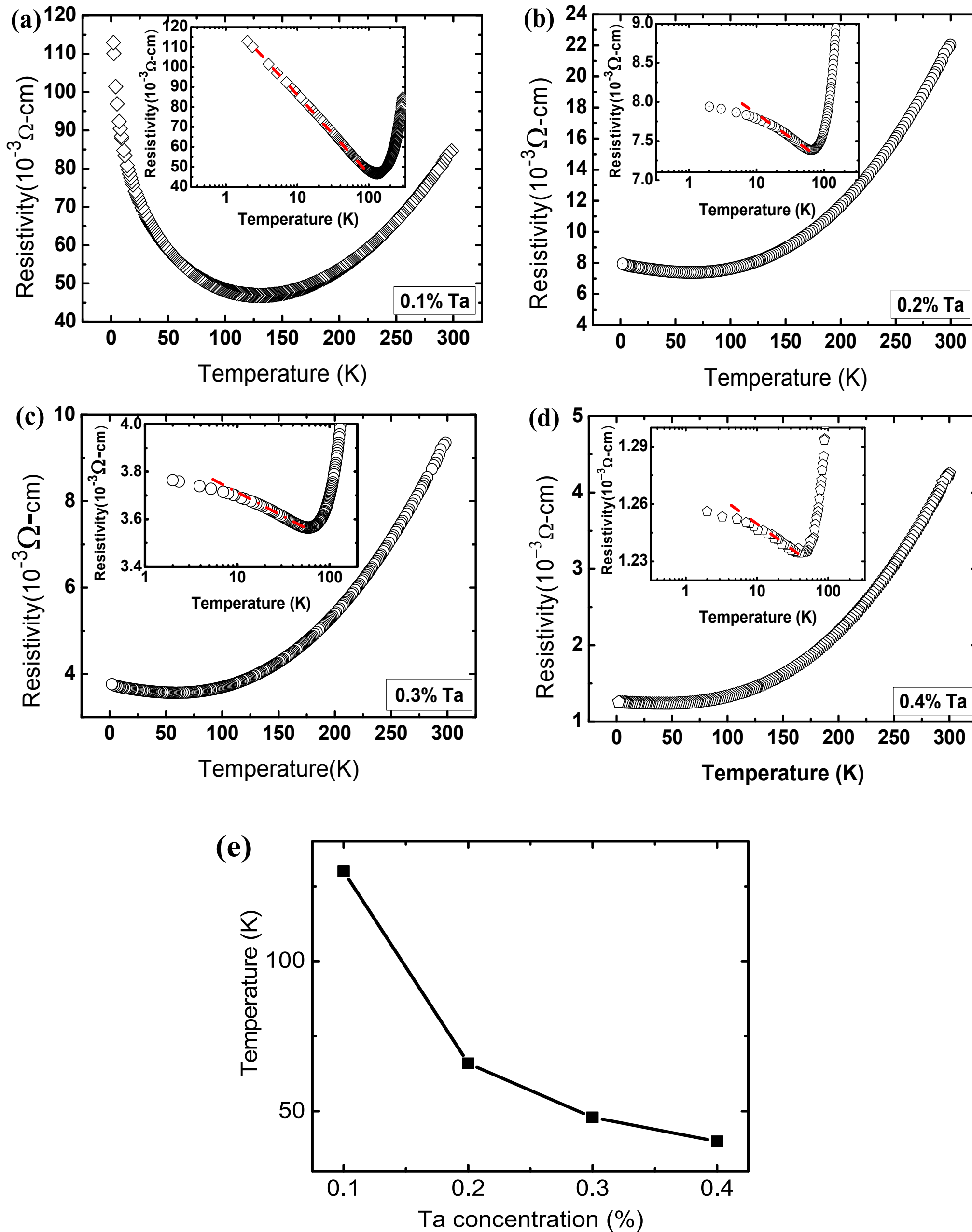


**Figure 5.3: Temperature dependent resistivity measurement of $TiO_2$ samples with Ta concentrations (a) 0.1% (b) 0.2% (c) 0.3% (d) 0.4% and (e) Plot of $T_{min}$ with Ta concentration.**

The MR of 0.1% Ta doped $TiO_2$ film measured at different temperatures and configurations are shown in Fig. 5.4. Between 5 K and 70 K, the MR is negative. In contrast, at 2 K, it is positive. The MR is anisotropic as the values measured at different configurations deviate a lot. This phenomenon is quite similar as the MR measurement of pure anatase $TiO_2$ thin film been discussed in chapter 3. There we attribute the positive MR to variable range hopping

(induced by strong localization) and negative MR to quantum interference (reason of weak localization), which also can be applied here. Obviously, Ta doping has lowered the transition temperature of positive to negative MR (comparing with Fig. 3.5(a)), which may indicate the enhanced crystallinity of the samples (reduced random potentials) upon Ta doping. One Ta atom contributes an extra electron when it successfully substitutes a Ti atom in $TiO_2$ lattice. The statistical result of this substitution is the shift of the Fermi level towards conduction band, which increases the formation energy of oxygen vacancies (donor defects) [92]. Hence the suppressed formation of oxygen vacancies by Ta doping will improve the crystallinity of the $TiO_2$ film and reduce the random potentials. The involving of variable rang hopping mechanism may explain the relatively large change of the resistance at low temperatures as more and more electrons are strongly localized.

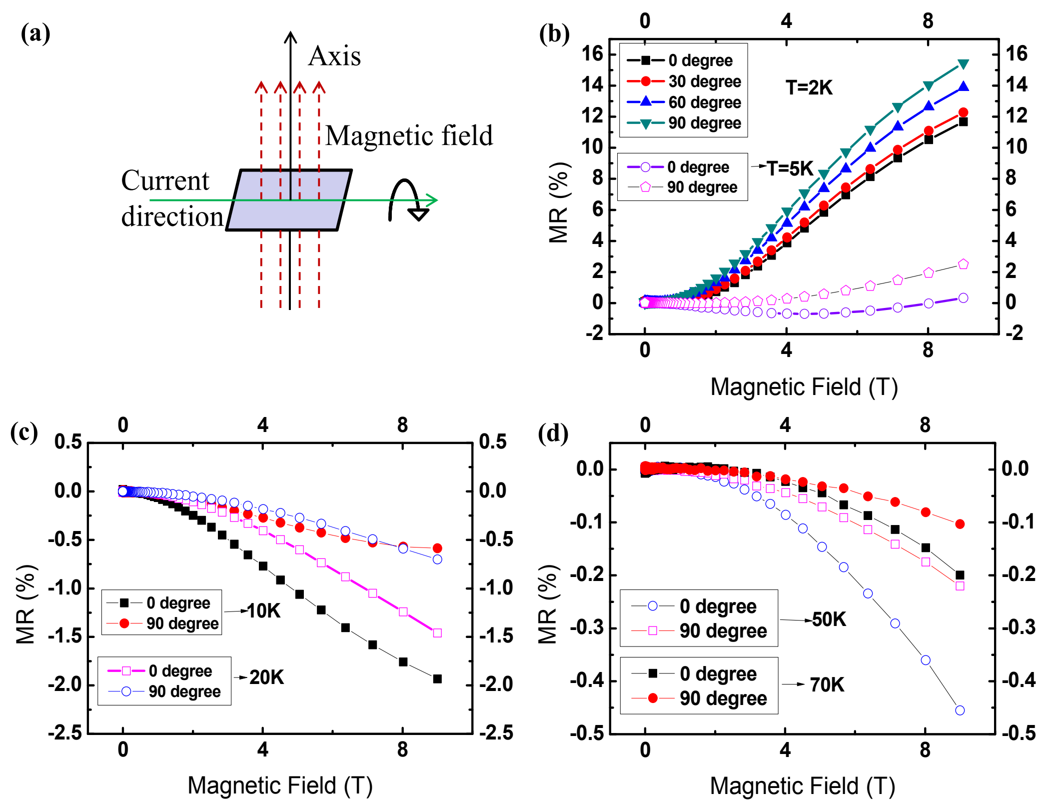


**Figure 5.4: (a) the measurement configuration. During experiment, sample is rotated as shown. (b) MR of 0.1% Ta doped $TiO_2$ thin film measured at 2 K and 5 K. Angles are measured between the magnetic field and central axis, as shown in (a). (c) MR of the same sample in (b) measured at 10 K, 20 K and 30 K. (d) MR of the same sample measured at 50 K and 70 K.**

When Ta doping level reaches 0.2%, the shifting of negative to positive MR at

low temperature (5K for 0.1% of Ta doping) disappears, as shown in Fig. 5.5(a). Only negative MR can be observed (except at 300 K, where MR is positive due to Lorentz circulation of electrons in magnetic field), which may indicate the vanishing of the strong localization. Similar phenomenon has been observed for 0.3% and 0.4% Ta doping cases, as shown in Fig. 5.5(c) and (d). This is consistent with the argument about the improving crystallinity of $TiO_2$ by Ta doping. The MR of the Ta doped $TiO_2$ films shows anisotropic behavior and its absolute value (|MR|) measured at any temperature below 100 K keeps decreasing with Ta concentrations ($\geq 0.2\%$). When the magnetic field is in the same plane of the measuring current ($\theta = 90°$), the MR is still finite (Fig. 5.5(b)). When the magnetic field is normal to the plane of the measuring current ($\theta = 0°$), the MR is more negative. This may indicate the quasi two dimensional natures of the thin films because in two dimensional structures the MR induced by weak localizations depends on the perpendicular component of the field only and in three dimensional cases it does not depend on the field direction. The anisotropic and non-vanishing MR could also be explained by super-positions of a constant and sinusoidal MRs which are due to Kondo effect and weak localization in two dimensions respectively [127]. As we do not have further techniques to separate these two possibilities (Kondo versus 3D weak localization) the mechanism that causes resistivity saturation with decreasing temperature is still not clear.

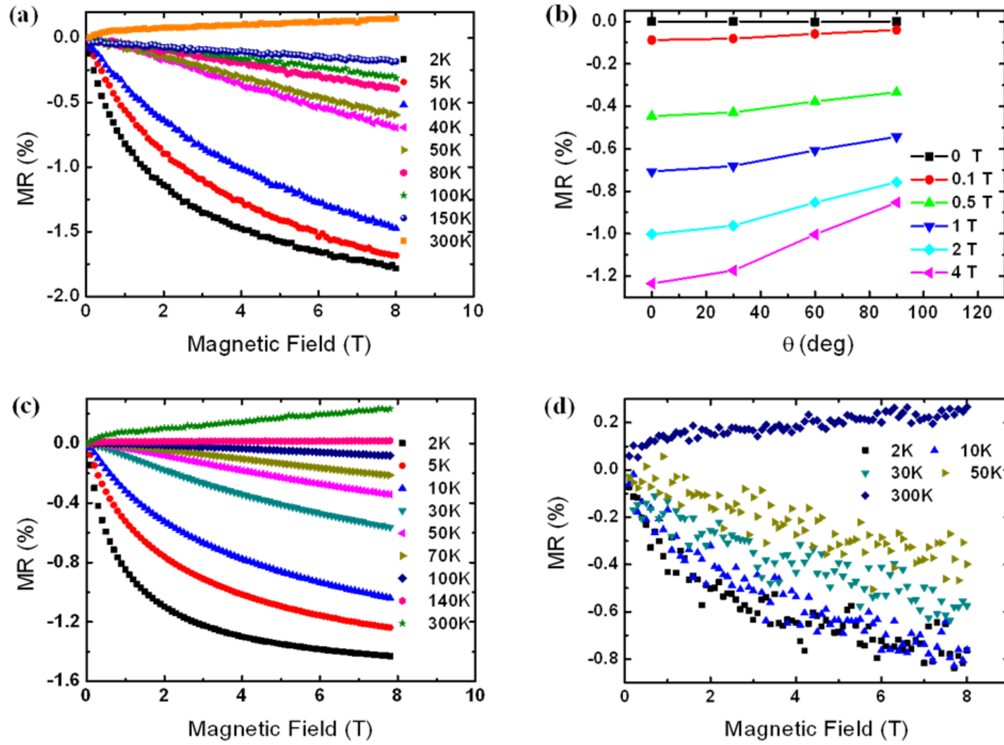


**Figure 5.5: (a) MR of 0.2% Ta doped $TiO_2$ measured at different temperatures. (b) MR of the same sample in (a) measured at different configurations; angles are described in Fig. 5.4 (d). (c) MR of 0.3% Ta doped $TiO_2$ measured at different temperatures. (d) MR of 0.4% Ta doped $TiO_2$ measured at different temperatures.**

The charge carrier density (*n*-type) and mobility of 0.1%, 0.2%, 0.3% and 0.4% Ta doped samples were measured and shown in Fig. 5.6. The electron density increases with Ta concentration and in all cases slightly decreases with increasing temperature (mechanism is not clear). The Ta concentration dependent electron density measured at room temperature was plotted in Fig. 5.6(e), where a linear relationship was observable for the electron density of the films as a function of Ta concentration (above 0.2%). Assuming all the electrons were contributed by Ta dopants, the effective Ta percentage (successfully replacing Ti atom in $TiO_2$ lattice and the electron can be ionized at room temperature) could be calculated, as shown in Fig. 5.6(e). Within 0.1% Ta doped $TiO_2$ film, only 33.9% dopants were effective. However, this value was increased to 84.7%, 90.5% and 95.3% for 0.2%，0.3% and 0.4% Ta doped films respectively. The losses of the electron density may be due to localizations, in which case, fewer electrons were localized by increasing Ta concentration, which also indicates the improved crystallinity of $TiO_2$ films by

Ta doping. The mobility does not change with temperature continuously. As the temperature decreases mobility starts to increase because of the decreased electron-phonon and electron-electron scatterings till a transition point is reached. After that, mobility starts to decrease because localizations become effective. Below the transition temperature, mobility seems to saturate with increasing Ta concentration to 0.4%. This is consistent with the argument that the crystallinity of the sample is enhanced by Ta doping as the localization at low temperatures is suppressed with increasing Ta concentration. The maximum mobility of each sample keeps increasing with Ta concentration, as shown in Fig. 5.6 (f), which is nonlinear. Generally, it is difficult to determine when the sample becomes totally metallic because the resistivity follows semiconductor like behavior at low temperatures. However, if we use the mobility of the samples as a criteria for metallicity, its bell shaped behavior with temperatures becomes broader with increasing Ta concentration, until reaching 0.4% Ta concentration, where the low temperature drop of mobility disappears, indicating a transition point from semiconductor (below 0.4% Ta concentration) to metallic behavior (0.4% Ta concentration). This is within a factor of two (Ta concentration of 0.8%) predicted from impedance measurements (Chapter 4).

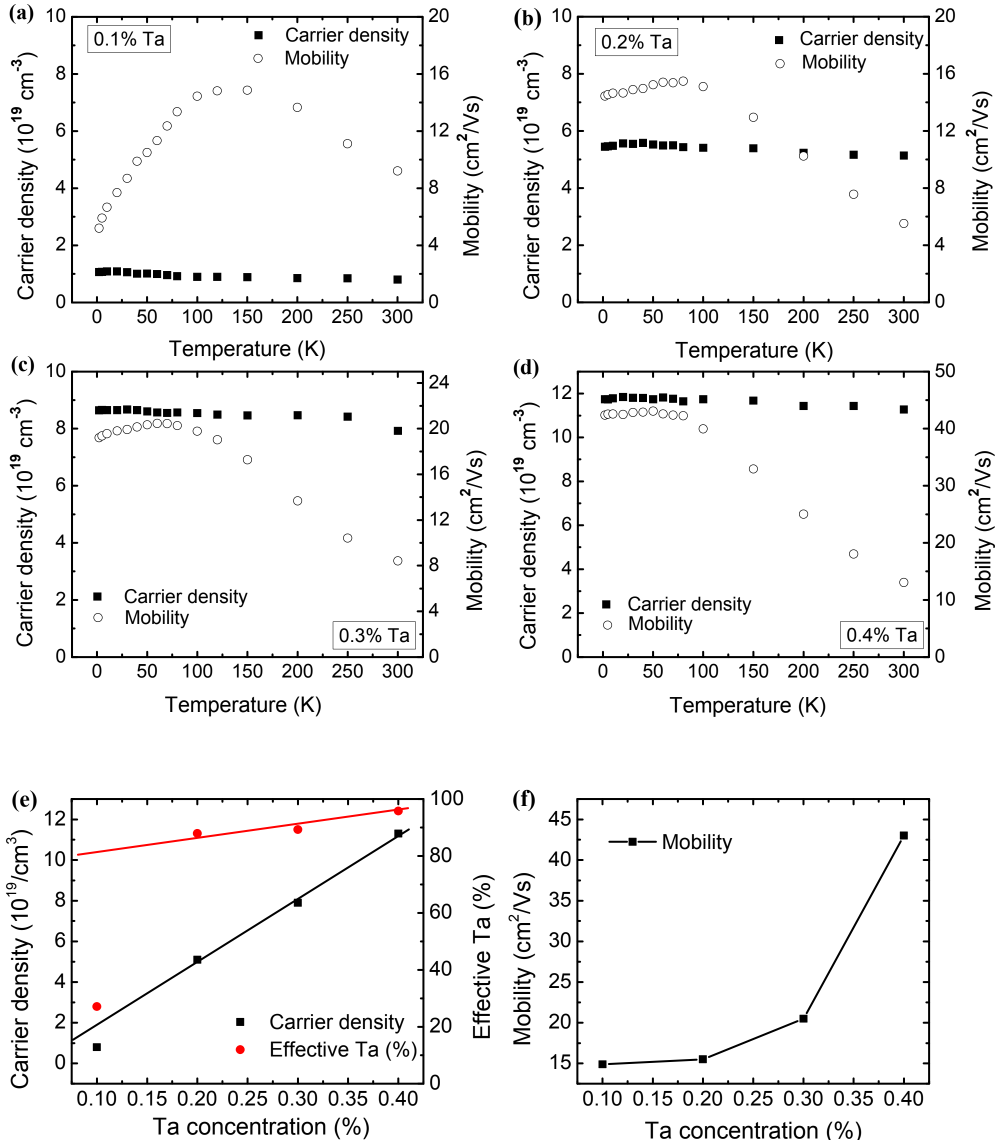


**Figure 5.6: Hall measurements of (a) 0.1% (b) 0.2% (c) 0.3% (d) 0.4% Ta -$TiO_2$ thin films. (e) Ta concentration dependent carrier density measured at room temperature (left axis) and effective Ta percentage (right axis). The straight lines are guided by eyes. (f) Ta concentration dependent maximum mobility of the films in (a) (b) (c) and (d).**

## 5.5 Summary

Transport properties of nominal 0.1%, 0.2%, 0.3% and 0.4% Ta doped anatase $TiO_2$ thin films have been studied. Comparing with the transport mechanism of the pure $TiO_2$ sample presented in chapter 3, a transition of strong to weak localizations upon Ta doping at low temperatures was observed and discussed. Ta ions improve the crystallinity of the sample as they suppress the formation of oxygen vacancies, which then reduce the localization effects. MR and Hall measurements of the samples have been done, which are consistent with above

conclusion. The anisotropy of the MR suggests a combination of 2D weak localization and Kondo effect at low temperatures. The data is not adequate to rule out 3D weak localization effects. We found that 0.4% Ta doping is a critical concentration where the anatase $TiO_2$ films undergo a transition into metallic behavior by analyzing their charge carrier and mobility behaviors in the range of temperatures investigated in the present study.

# Chapter 6 Nickel impurity mediated reversible ferromagnetism of rutile $TiO_2$ substrate upon annealing

Deposition of the film in high vacuum gives metallic and ferromagnetic sample. However, later it is found that treating the substrate in similar annealing condition can provide the same character as well. By further systematic study, Ni impurity was found in the vacuum annealed substrate which is responsible for the observed signals. The experimental details will be elaborated step by step in this chapter, but first, let me introduce some basic knowledge of magnetisms.

## 6.1 Introduction to oxide based Dilute Magnetic Semiconductors

### 6.1.1 Types of magnetism

An electron has both charge and spin freedoms, while only the latter can contribute to the magnetism. According to the response of the electrons (spins) under magnetic field, magnetism can be recognized as diamagnetism, paramagnetism, ferromagnetism, anti-ferromagnetism, ferrimagnetism, and superparamagnetism.

An orbiting electron is equivalent to a current loop with a magnetic dipole moment. Hence in the materials with fulfilled atomic shells, “Lenz law” (application of an external magnetic field causes induced current in a material which opposes the change in external magnetic field) becomes significant, which then imply the diamagnetism (repel the magnetic field). In most materials it is a weak effect except in superconductors, a strong quantum effect repels the magnetic field entirely.

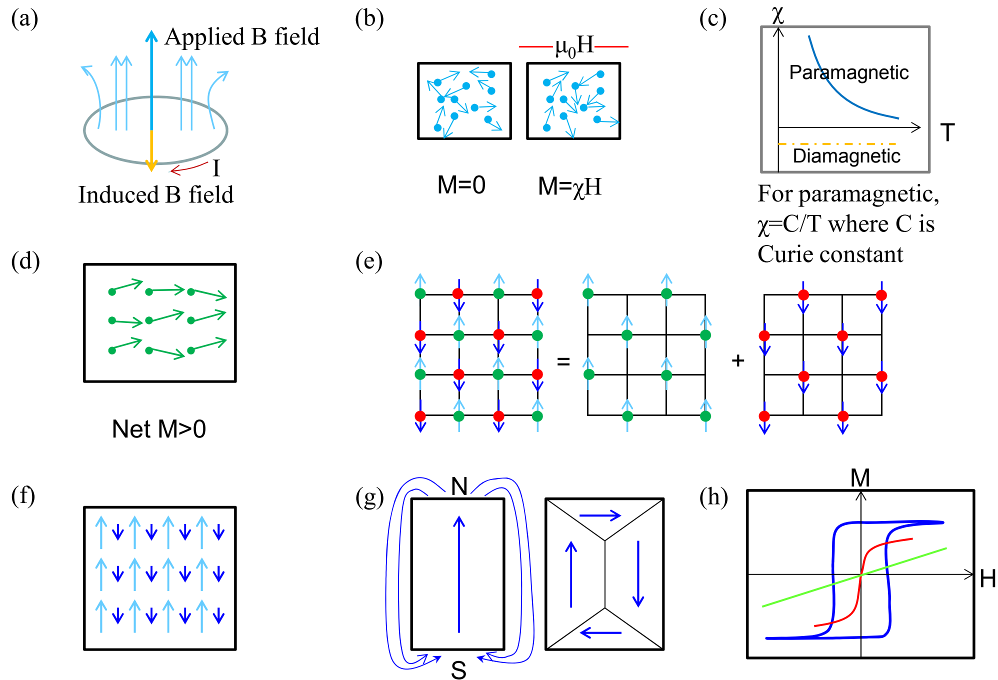


**Figure 6.1: (a) Principle of diamagnetism: the internal field repels the applied magnetic field. (b) Principle of paramagnetism. Without external magnetic field, the net magnetization is zero. By applying field, linear relation of magnetic moment and applied field can be seen. (c) Plot of susceptibility of paramagnetic (positive $\chi$) and diamagnetic (negative $\chi$) materials with temperature. (d) Principle of ferromagnetism. Without magnetic field, net positive magnetization exists. (e) Principle of anti-ferromagnetism, where its lattice equals two sub-lattices with equal amplitude but opposite direction of spin configurations. (f) Principle of ferrimagnetism, where the sub-lattices have different amplitude of spins. (g) Formation of magnetic domains can minimize the magnetostatic energy. (h) Different behaviors of M-H relationship of paramagnetism (green), ferromagnetism (blue) and superparamagnetism (red).**

Paramagnetic materials are attracted when in the present of magnetic field. After removing the field, materials recover to the initial state. Paramagnetism can be found in the materials with some unpaired electrons, where the electrons have non-coupling spins. It is still a weak effect (although stronger than diamagnetism) because only a small fraction of the spins will be oriented by the field. The magnetic moment has linear relations with the applied magnetic field at a particular temperature.

When the unpaired spins in the outer shell exchange coupling with each other, the material may show ferromagnetism (positive exchange coupling) or anti-ferromagnetism (negative exchange coupling). For the former, spins will be aligned under presenting magnetic field. Hence large magnetic moment is induced. A portion of the aligned spins will not be disrupted by the destructive

energy (e.g. thermal fluctuation) after removing the field. The remaining aligned spins will be destroyed by applying opposite magnetic field and large magnetic moment in opposite direction will be induced by further increasing the field. As a result, normally a hysteresis loop of the magnetic moment will be obtained by cycling the magnetic field in the measurement of the ferromagnetic materials. For the latter, due to negative exchange coupling, spins will be aligned in a pattern with neighbors pointing in opposite directions. As the magnetic moments have the same amplitude, in the absent of external magnetic field, the anti-ferromagnetic structure corresponds to a vanishing total magnetization. In the present of magnetic field, due to different responses of the sublattices, there may remain some net magnetization. For ferromagnetism and anti-ferromagnetism, the temperatures above which the properties are totally destroyed (spins become totally random) are called Curie temperature and Neel temperature respectively. Anti-ferromagnetism plays a crucial role in giant magnetoresistance (GMR) based spin valve sensors [128, 129].

Similar to but different from anti-ferromagnetism, sublattices with unequal opposing spins can be constructed in ferrimagnetic materials, where then a net magnetization remains. The temperature effect of ferrimagnetism is comparable to that of ferromagnetism as it holds a spontaneous magnetization below the Curie temperature, although, sometimes magnetization compensation point (where two sublattices have equal opposite moments) may be found at a particular temperature.

Below Curie temperature, magnetic moments throughout the volume of a ferromagnet are expected to align parallel. However, it does not happen in reality. Instead several regions called “domains” are created within which all the moments point in the same direction but the moments of the adjacent domains can point in other directions. As a result, the net magnetization is zero. The formation of domains is to minimize the magnetostatic energy (the energy which a single domain magnet sustains subject to its own demagnetizing field). The boundary which separates two neighboring domains is called domain wall, which is related to exchange energy and anisotropy energy.

The size of the particle separates ferromagnetism from superparamagnetism.

When the radius of the particle is larger than a single domain size (40~100nm), a multi-domain ferromagnet is formed. In contrast, when the particle becomes smaller than a single domain size, superparamagnet is formed. There are large numbers of moments pointing in the same direction within a superparamagnetic particle. However, in the absent of external magnetic field, the time used to measure the magnetization of the particles is much longer than the time between two spin flips under the influence of temperature. Hence the magnetization as a whole will fluctuate like a paramagnet. However, their susceptibility (the ability to be changed by magnetic field) is much larger than the one of paramagnets. When the spins are all aligned by the external field, the magnetization of a superparamagnet becomes saturate, which is similar but slower than that of a ferromagnet.

Fig. 6.1 shows the general characters of types of magnetic properties.

### 6.1.2 Dilute Magnetic Semiconductors

In traditional electronics, charges are the only media of signal. Hence to introduce the spin freedom into electronic devices becomes attractive in spintronic applications. One main strategy to achieve that is to introduce the polarized spins into conventional semiconductors with the host material's application worth properties maintained [130, 131]. To the end, dilute magnetic semiconductors (DMS) have been a major focus of magnetic semiconductor research. The practical DMS should be nonmagnetic semiconductors with magnetic dopants uniformly distributed throughout the host matrix which then as a whole become spin polarized above room temperature. Oxides, especially transitional metal oxides have been one of the most versatile material systems because of their special structural forms, bonding characteristics and the defect states [132]. Predominantly three popular models are used to explain the origin of ferromagnetism in DMS systems, which are 1) direct coupling of spins; 2) exchange coupling of spins through conducting charges; 3) bond magnetic polarons.

When the ferromagnetic dopants in semiconductors are close enough to have overlap of their wave functions, direct exchange coupling of the spins will occur. This kind of coupling is entirely the dopants' property; hence it is less interesting in the application point of view.

The coupling of the spins is strongly distance dependent. When the distance is large enough that direct spin coupling is unlikely to happen, free charge carriers may behave as the media [133]. This kind of indirect exchange interaction model, named as Ruderman-Kittel-Kasuya-Yosida (RKKY) model, was proposed to explain the unconventional ferromagnetism in DMS [134, 135]. It is believed that the conduction charge carriers may be temporarily polarized by a localized magnetic moment when they are around it. The polarized charge carriers can interact with other localized magnetic moments during their movements. Hence the localized magnetic moments interact indirectly with each other mediated by the free charge carriers.

In some systems, the charge carriers induced by the dopants or by the deficient of anions (oxygen vacancies) are localized. In case a local magnetic moment falls in the region enclosed by the localized carriers, it may polarize them, hence forming a bound polaron with a large net magnetic moment [136, 137]. With increasing density, the overlap of the polarons may build up a short range or even long range magnetic ordering. This model is widely applied in oxide DMS systems with large dielectric constant as it could explain the high temperature ferromagnetism [35].

**6.2 Background of the experiment**

Among various oxides based DMS, $TiO_2$ is one of the most explored host material and many types of dopants have been introduced into this host. Cobalt doped $TiO_2$ generated great interest for its above room temperature ferromagnetism, where in some cases it was discussed as magnetism originating from Cobalt clusters [31, 32]. In contrast, nonmagnetic atom doped $TiO_2$ also can show ferromagnetism, where cationic vacancies or $Ti^{3+}$ induced by oxygen vacancies were discussed as the reason [33, 34]. As all of these experiments used oxide crystals as the substrate, it is crucial to first confirm that the substrate is magnetically inert. Yee *et al*. observed that ferromagnetism arose only from commercial single side polished substrates of $Al_2O_3$, $LaAlO_3$, $SrTiO_3$, $TiO_2$, and ZnO, where they claimed that Fe ions from the unpolished side gave ferromagnetism [38]. They showed reversibility of this ferromagnetism by implementing vacuum and subsequent atmospheric annealing. However, the detailed physical explanations for those observations

were lacking.

**6.3 Experimental details**

In the present study, double sides polished single crystal rutile $TiO_2$ (001) substrates ($5 \times 5 \times 0.5$ $mm^3$) were obtained from three different vendors (CrysTec GmbH Kristalltechnologie, Germany; MTI Corporation, USA; Shinkosha Co., Ltd, Japan). After been annealed in high vacuum environment at $5 \times 10^{-6}$ Torr, 800$^{o}$C, the transparent pristine sample becomes dark, which has been attributed to oxygen vacancies and some other defects [36], as shown in Fig. 6.2(a) and turns into a pale yellow color by subsequent air annealing in a furnace. (The transmission of the film treated under different conditions is shown in appendix 7) This process is highly repeatable. Silver paint got involved in the annealing in vacuum for better indication of the annealing temperature on the substrate. Before measuring the magnetic properties, silver paint was removed as much as possible.

The magnetic properties of the samples were measured by a SQUID magnetometer in the temperature range of 10-300 K. The applied measuring field during magnetic moment to temperature (MT) and magnetic moment to magnetic field (MH) processes was kept at 100 Oe. In-plane magnetic measurement was performed when the magnetic field was parallel to the sample surface while the out-of-plane measurement indicates the perpendicular of the magnetic field and the sample surface. The low temperature MH measurement was always performed after zero fields cooling (ZFC). In ZFC process, temperature was reduced without applying any field.

The transport properties were measured in four probes Van de Pauw configuration, where the passing direct current is kept the same during whole scanning temperatures. The charge carrier density and mobility were obtained from Hall effect measurement, in which, scanning field ranges of 18 Tesla (T) and straight line in the Hall resistance plot can be promised.

The existence of Ni in vacuum annealed $TiO_2$ crystal was observed by SIMS and RBS. The diffusion mechanism was mainly studied by RBS. In SIMS measurement, $Ar^+$ was used to etch the sample with beam size $100 \times 100$ $\mu m^2$, simultaneously, $Cs^+$ was used as the primary bombarding ions and the ejected secondary particles were collected and analyzed. The etching depth of the hole

is roughly 0.5 μm, which was measured by step profiler. All the interesting data can be found in this depth range. In RBS measurements, 2 MeV $He^+$ ions was used as the emission beam and a resolution of 15 KeV silicon surface barrier detector was placed at $160^o$ scattering angle geometry. The sample was mounted by using 4-axis goniometer.

The Ni valance states in $TiO_2$ were measured by XAS, where Ni L-edge was obtained in total electron yield acquisition mode by recording sample current as a function of photon energy of incident x-rays. The experiment was carried on in ultrahigh vacuum (UHV) chamber with a base pressure of $1\times10^{-10}$ mbar. To eliminate the fluctuation in the incident x-ray intensity, all the spectra were normalized by the incident x-ray intensity monitored by a refocusing mirror.

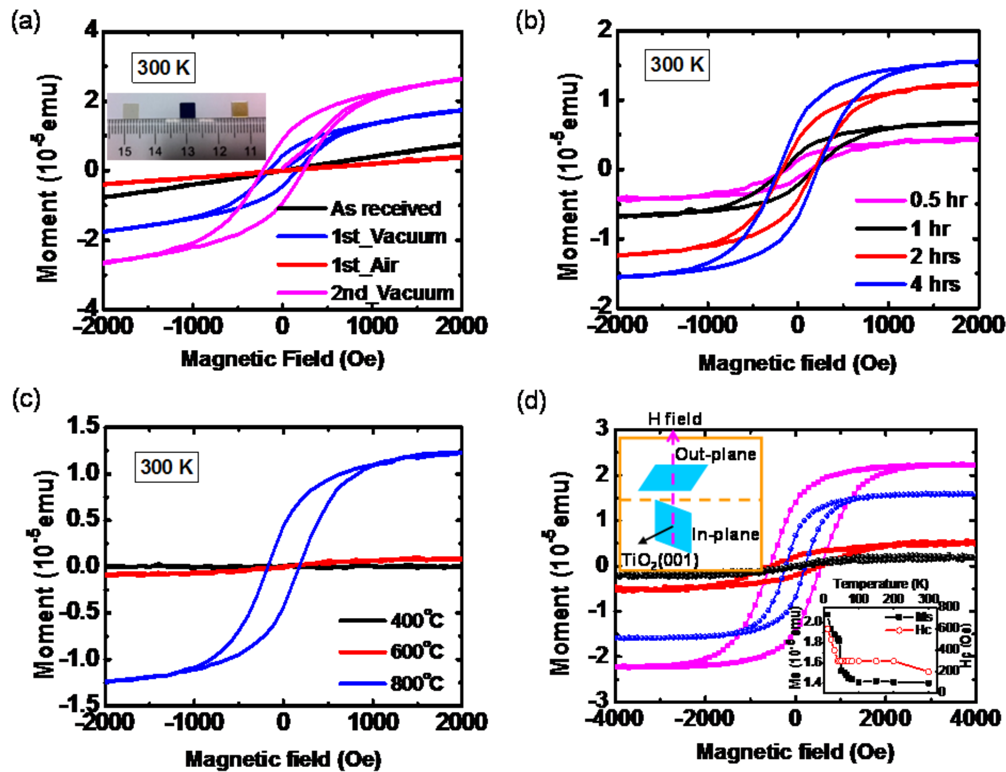


**Figure 6.2: (a) Magnetic moment versus field (MH) measurement of $TiO_2$ substrate at room temperature. The annealing temperature is 800°C and the annealing time is 2 hours. The vacuum level is kept at $5\times10^{-6}$ Torr. Inset shows the photo of pristine, vacuum annealed and subsequently air annealed samples. (b) Room temperature MH measurements of $TiO_2$ substrates vacuum annealed with 800°C for different times. Here paramagnetic part of the signal was deducted. (c) Room temperature MH measurements of $TiO_2$ substrates vacuum annealed for 2 hours with different temperatures. Only the ferromagnetism component is shown. (d) MH measurement at 10 K and room temperature of samples oriented in-plane and out-of-plane with magnetic field. Black and red colors indicate the out-of-plane plot at room temperature and 10 K. Blue and fuchsia colors indicate the in-plane plot at room temperature and 10 K respectively. Inset at the left corner shows the schematic graph of in-plane and out-of-plane configuration. Inset at the right corner shows the changes of saturation magnetization (magnetic moment at 4000 Oe in the main graph) and coercivity with temperature in the in-plane measurement.**

### 6.4 Results and discussions

As received $TiO_2$ substrate shows paramagnetic property, as shown in Fig. 6.2(a). After vacuum annealing for 2 hours (heating and cooling rates are 10 K/min, where this time was not considered), a ferromagnetic loop is seen. A subsequent air annealing for 2 hours turns the samples back into the paramagnetic state, and when the sample is annealed in vacuum again under the same condition, ferromagnetism returns and becomes even stronger. The

time dependence of the vacuum annealing of the substrates was studied and is shown in Fig. 6.2(b). By keeping the annealing temperature and pressure the same as in Fig. 6.2(a), it can be seen that the saturation magnetic moment ($M_s$) continuously increases with annealing time; however, the coercivity ($H_c$) remains constant. Temperature dependent vacuum annealing of the substrates are shown in Fig. 6.2(c), where it can be seen that below 600°C ferromagnetism cannot be turned on for the duration of time studied (2 hours). This temperature corresponds to 75 meV of thermal energy. In-plane and out-of-plane magnetic moment ($M$) to magnetic field ($H$) relation curve was plotted in Fig. 6.2(d), where the sample was annealed in vacuum for 4 hours and with temperature and pressures the same as in Fig. 6.2(a). By considering only the in-plane MH loop at different temperatures, it can be found that both $M_s$ and $H_c$ decrease with increasing measurement temperature. And it is similar for the out-of-plane case, where at room temperature $H_c$ disappears, as shown in the inset of Fig. 6.2(d). Generally, the $M_s$ measured in-plane is much larger than that measured out-of-plane. This indicates strong anisotropy of the ferromagnetism. The reversible ferromagnetism of $TiO_2$ substrate in (110) orientation was studied and shown in appendix 8.

Temperature dependent resistivity ($\rho$-$T$) of $TiO_2$ crystals annealed 2, 4 and 8 hours in vacuum were measured in the temperature range of 20 to 400 K, as shown in Fig. 6.3(a), where in this plot, two transitions can be observed around 40 and 280 K. Above 280 K, the resistivity decreases slowly with increasing temperature. Below 40 K, the decrease of resistivity with increasing temperature becomes more dramatic. In between 40 and 280 K, metallic behavior can be seen, where closer to 40 K regimes, resistivity changes much faster than that closer to 280 K regimes. The charge carrier density and the mobility between 20 and 360 K are plotted in Fig. 6.3(b). The charge carrier density increases with temperature until 40 K and then decreases with temperature until 100 K, after which, it shows increasing behavior again. In contrast, the mobility increases sharply with temperature between 20 and 40 K, and then decreases continuously. The differences in the resistivity, carrier density and mobility for the samples annealed in vacuum for different times (2, 4 and 8 hours) are relatively small.

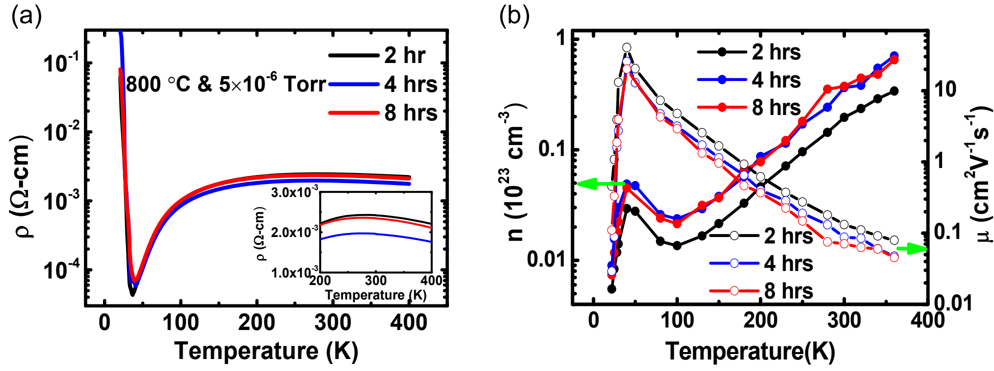


**Figure 6.3: (a) Temperature dependent resistivity measurement of $TiO_2$ samples vacuum annealed for 2, 4 and 8 hours. Thickness of 50 nm was used in the calculation. The curve near 300 K is expanded in the inset. (b) Hall effect measurement of the samples described in (a). The solid circles indicate the charge carrier density and the open circles represent mobility.**

To understand the nature of the above magnetic and electronic phenomena, the purity of the substrates was firstly checked by SIMS using calibrated standards as reference ($TiO_2$ thin films containing 1% Ni, 1% Fe, 1% Co, 1% Mn and 1% Cr on Si substrate). Ni is the dominant magnetic impurity at 100 ppm level in the as received sample. In contrast, the concentrations of other standard magnetic impurities are at least one to two orders of magnitude smaller. As shown in Fig. 6.4(a), around 10% Ni was observed in the sample after vacuum annealing with 800°C for 4 hours. Even after air annealing, around 1% Ni still can be detected. Hence one can speculate that the ferromagnetism of $TiO_2$ substrate comes dominantly from Ni impurity though more evidence is required to substantiate the claim. RBS was done in order to verify this argument. As shown in Fig. 6.4(b), in both as received and air annealed samples, Ni concentration was too low to be detected. However, in the vacuum annealed sample, a significant Ni peak can be seen. The Ni concentration is around 12% out of 100% Ti by considering the peak to peak values in the 4 hours vacuum annealed substrate, which is close to the value obtained by SIMS. As shown in Fig. 6.4(c), the RBS spectrum of vacuum annealed samples can be well fitted by Gaussian distribution, and the RBS random and channeled peaks of Ni overlap each other, which indicate that all the Ni atoms are in the interstitial locations. In addition, the surface peak of Ti is also quite large, which means that there is crystalline disorder near the surface. The

concentration of Ni in $TiO_2$ substrates which were vacuum annealed for 1, 2 and 4 hours was measured by RBS, as shown in Fig. 6.4(d). The intensity of the Ni peak increases with annealing time, which is consistent with the increasing behavior of the ferromagnetism. Interestingly, the Ni peaks are almost centered at the same position. The integrated Ni intensity ratio from RBS was plotted in the inset of Fig. 6.4(d), where the $M_s$ ratio of those samples was shown as well. Both Ni intensity and the $M_s$ increase with vacuum annealing time (t) as $t^{1/2}$ suggesting a diffusion process. As can be seen, the $M_s$ ratio increases faster than Ni intensity ratio, which suggests nonlinear ferromagnetic coupling with increasing Ni concentration. From thermodynamic point of view, the formation of Ni clusters is preferable under oxygen poor condition. As the bonding energy of Ni-O (373 $\pm$ 3 kJ/mol) is smaller than Ti-O (672.4 $\pm$ 9.2 kJ/mol) [138, 139], when oxygen escapes from $TiO_2$ due to vacuum annealing, Ti is more competitive with respect to Ni in forming bond with the left over oxygen. Hence Ni forms metallic clusters near the surface.

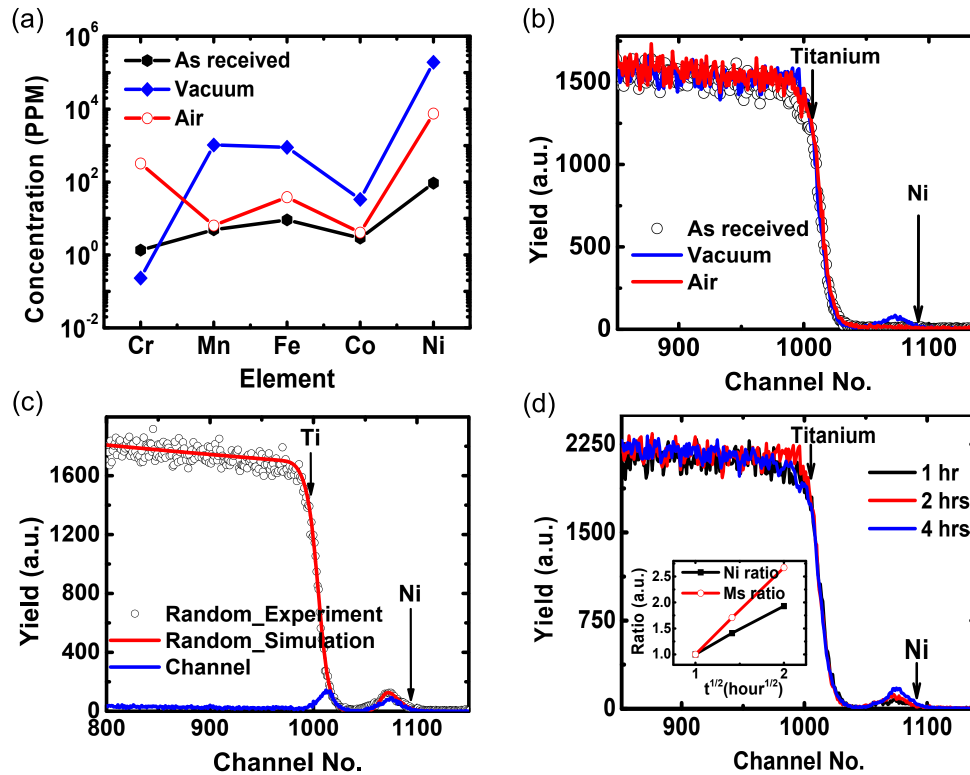


**Figure 6.4: (a) SIMS data of as received, vacuum annealed and air annealed $TiO_2$. The vacuum and air annealing time is 4 hours. (b) RBS random curve of as received, vacuum annealed and air annealed $TiO_2$ substrates as in (a). (c) RBS random, channeling and curve fit for the vacuum annealed sample in (a). (d) RBS random peak of $TiO_2$ samples vacuum annealed for 1, 2 and 4 hours. Inset shows Ni peak intensity ratio and $M_s$ ratio of the $TiO_2$ samples annealed in vacuum for different times. Ni peak intensity was calculated by integration of the Ni peak area.**

TEM equipped with EDX shows the existence of Ni clusters near the sample surface as well. As shown in Fig. 6.5(a), a HRTEM cross sectional image of the 4 hours vacuum annealed $TiO_2$ sample is seen. In Fig. 6.5(b), an element sensitive EDX scan of the same region is shown where it is seen that Ni is distributed densely within a 50 nm region close to the sample surface. As suggested by RBS channeling data, Ni may exist as interstitials or clusters. A higher resolution image shows such granular regions in the inset of Fig. 6.5(a). The granular Ni clusters in the ~ 50 nm $TiO_2$ surface layer may partly explain the transport behavior as well. If we assume all the electrons from room temperature to 40 K were contributed by Ni atoms spread within a 50 nm region near the sample surface, it can be deduced from Fig. 6.3(b) that the Ni concentration is about 10% in that region, which is a reasonable value. (If we

assume a Gaussian distribution the Ni density near the center of this region may be closer to 30% or more providing near percolation) [140]. Of course, Ti interstitials may contribute electrons as well [89]. Because Ni does not form a continuous sheet, rather clusters with a small separation (tunnel barriers); the transport is similar to a cermet structure. This explains the relatively flat resistivity from room temperature to 40 K with a value close to $10^{-3}$ Ω·cm, characteristic of a bad metal. At very low temperatures, the tunnel barrier causes the resistivity to diverge and the barrier energy is about 3.4 meV.

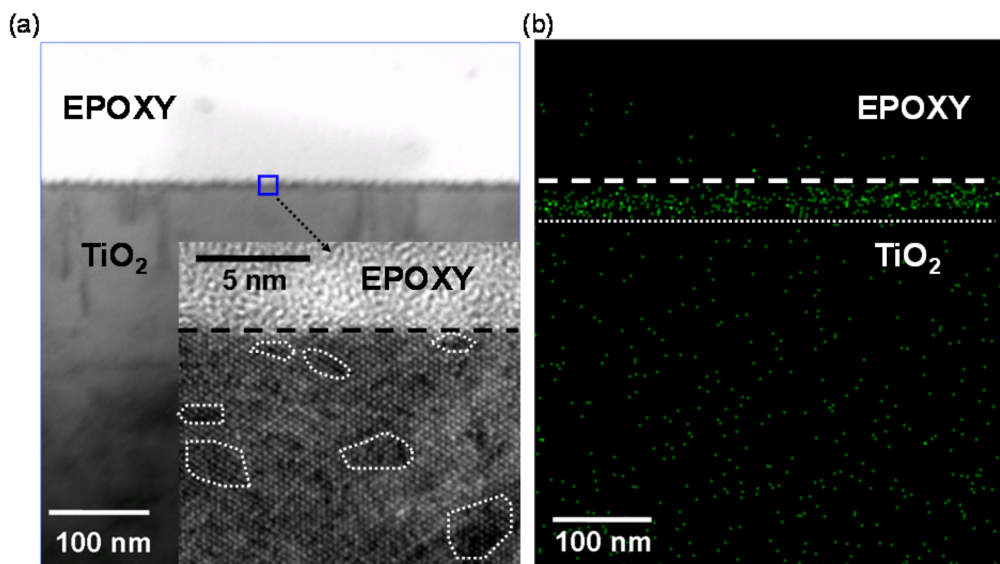


**Figure 6.5: (a) HRTEM image of $TiO_2$ crystal vacuum annealed at 800°C for 4 hours. The likely Ni rich areas are shown by white circles. (b) Elemental scan of the same area described in (a), where the two dash lines show the boundary of the Ni rich region.**

The Ni impurity may come from three sources. The first one is the silver paint which appeared in the vacuum annealing. To investigate its effect, a piece of $TiO_2$ substrate was annealed in vacuum ($5\times10^{-6}$ Torr) without using silver paint (heater temperature was set at 1000°C, as there is a gap between the heater and the sample, the actual temperature on the sample is unknown). Two hours' vacuum annealing gives the sample a comparable magnitude and shape of the hysteresis ferromagnetism curve with the one annealed under 800°C with silver paint. As a result, we can neglect the first source. The second source of Ni is the heater in the chamber. To study the possibility, $TiO_2$ substrate sandwiched by two pieces of LAO (001) substrates was annealed in vacuum with one LAO substrate attached to the heater. Ferromagnetism was

observed in $TiO_2$ substrate but not in LAO substrates. Hence most probably, Ni impurity is the parasite of $TiO_2$ substrate, which may come from the third source, vendors' substrate growth chamber.

For comparing the transport properties and the magnetic properties of vacuum annealed $TiO_2$, MT curves of the sample annealed in vacuum for 4 hours were measured and shown in Fig. 6.6(a), where the temperature range covers 10 to 300 K. In the ZFC curve, a maximum value is observable at around 40 K, which is identical to the temperature where resistivity reaches minimum while carrier density and mobility reach maximum. Different cooling fields modify the shape of the MT curve. With 40 Oe cooling field, the magnetic moment curve becomes flat below 40 K. XAS data shows the existence of Ni in vacuum annealed $TiO_2$ crystals as well. As shown in Fig. 6.6(b), Ni was not detected in the as-received sample. However, $Ni^{2+}$ and $Ni^{3+}$ peaks were obtained in both the vacuum annealed and air annealed samples, where the difference is that the $Ni^{3+}$ peak in air annealed sample is much enhanced and the $Ni^{2+}$ peak is much weakened comparing with the vacuum annealed one. As can be seen, for the vacuum annealed sample, $L_{2,3}$ edges of $Ni^{2+}$ locate at 854 eV and 873 eV separately. In addition, there is a shoulder located at 857 eV, which indicates the $L_2$ edge of $Ni^{3+}$. However, due to the limitation of the accuracy, $L_3$ edge of $Ni^{3+}$ cannot be separated clearly. The curve of the air annealed sample is not as that smooth as the vacuum annealed one, probably due to less Ni and the rough surface of the sample. Strangely, in the vacuum annealed sample, Ni was not observed in metal state. This might indicate that Ni exists only in oxidized states within the detection depth (around 20 nm to 30 nm from the surface).

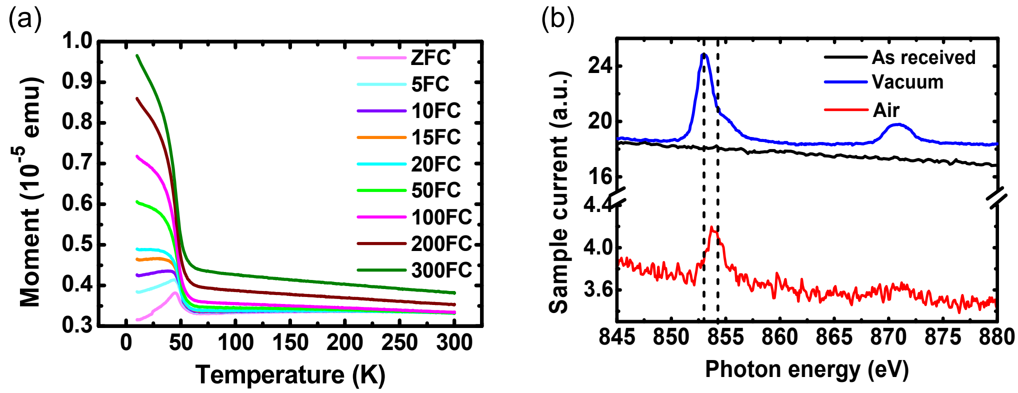


**Figure 6.6: (a) Magnetic moment of $TiO_2$ as function of the measuring temperature. In the legend, the number ahead of FC indicates the cooling field. For example, 50FC represents that the cooling field is 50 Oe. (b) XAS data of the as received, vacuum annealed and air annealed $TiO_2$ samples.**

As already shown in Fig. 6.6(a), magnetic moment reaches maximum around 40 K, which corresponds to the blocking temperature ($T_B$) of Ni cluster with radius ($r$) 4.1 nm. Here $r$ is calculated with the follow equation [141]:

$$r = \left( \frac{90 k_B}{4 \pi K_{eff}} \right)^{1/3} \tag{6.1}$$

where $K_{eff}$ is the anisotropy energy density, here taken as $5.7 \times 10^4$ $J \cdot m^{-3}$, which is the bulk value of Ni [142]. As the ferromagnetism of the vacuum annealed sample still exists at room temperature, by applying equation (6.1), the dominant Ni cluster size at 300 K can be calculated as 8.0 nm. However, it cannot be simply concluded that the Ni cluster size spreads between 4.1 and 8.0 nm. As shown in the inset of Fig. 6.2(d), $H_c$ decreases with temperature overall and keeps almost constant within 40 to 200 K, which indicates that the surface of the large size Ni cluster has already been oxidized at 40 K. Above this temperature, the outer oxide layer will protect the inside Ni cluster until at least 200 K. Hence, Ni might exist in $TiO_2$ crystals as Ni-NiO core shell structure, which is identical with the XAS result that only $Ni^{2+}$ and $Ni^{3+}$ states can be detected. The exchange coupling in such kind of core shell structure will increase the superparamagnetic limit, which is very important in recording media [143, 144].

Ni contribution to ferromagnetism in $TiO_2$ substrate was reported before, where Ni ions were intentionally ion implanted into $TiO_2$ crystal and the relationship of ferromagnetism with Ni concentration was studied [145].

However, in that work one observation could not be explained properly. The measured saturation magnetization was much larger than the expected value of $0.61\mu_B$/Ni. Hence current experimental result has given an answer to this controversy. In their case clearly in addition to the ion implanted Ni, there was impurity Ni dissolved in the substrate which segregated during the implantation annealing process adding to the Ni concentration at the surface.

**6.5 Summary**

In summary, vacuum annealed rutile $TiO_2$ crystal shows ferromagnetism, and we have shown that the magnetic source is Ni clusters segregated by Ni contaminants that exist as NiO at 100 ppm level in commercially available $TiO_2$ substrates. The segregation is thermally activated with a 75 meV barrier and under vacuum annealing, causes Ni to accumulate at the top surface and under subsequent air annealing Ni re-dissolves into the bulk. This segregated surface layer of Ni gives rise to the observed ferromagnetism and the surface conductance. The cermet structure of this layer leads to a bad metal which exhibits a tunneling behavior at low temperatures. Researchers in the field of DMS oxides are hence cautioned to not only check the level of magnetic impurities in the as received substrates (not limited to $TiO_2$, but also applied to others like $SrTiO_3$, ZnO, $Al_2O_3$, etc.) but also to double check the properties of the substrates under the film preparation conditions to minimize substrate interference in the film data.

## Chapter 7 Structural, electronic and optical properties of transparent conducting $SrNbO_3$ thin films

Conducting oxides are generally not suitable for photocatalytic experiment basically due to lack of internal electric field. However, recently a red metallic oxide $Sr_xNbO_3$ ($x < 1$) powders were found to be capable of light harvesting with application in photocatalytic water splitting [39]. To better understand the mechanism, we prepared epitaxial thin films and studied their structural, electronic and optical properties. We find that $SrNbO_{3+\delta}$ forms cubic perovskite structure on LAO substrate with lattice constant of around 4.10 Å. The optical bandgap of the film is near 4.0 eV. Surprisingly, transport studies reveal that such large bandgap oxide (prepared under pressure $1 \times 10^{-5}$ Torr) is found to be highly conducting, which is attributed to the large charge carrier density ($1.43 \times 10^{22}/cm^3$ at room temperature). In contrast, the mobility is only around 2.5 $cm^2/Vs$ at room temperature, which is questionable for substituting the function of internal electric field in photocatalytic experiment.

### 7.1 Introduction of the material

If stoichiometric $SrNbO_3$ can be prepared, it should be formed in cubic perovskite structure ($ABO_3$) with lattice constant of 4.11 Å [146] and it would be an archetypal $d^1$ oxide which might be expected to exhibit metallic conducting property based on DFT calculations [39, 147]. However, experimentally only non-stoichiometric $SrNbO_3$ was synthesized possibly because of a phase separation and instability of the stoichiometric structure [148]. The $Sr_xNbO_3$ compounds with $x < 1$ were firstly synthesized in 1955 [149]. It mostly formed in cubic perovskite structure with $0.70 < x < 0.95$ with the lattice constant increasing with strontium content [150]. For the samples with $0.60 < x < 0.70$, cubic perovskite and tetragonal phases coexisted [151]. Later in the 90s, the electronic and magnetic properties of the compounds with $0.70 < x < 0.95$ were studied [132]. The samples exhibited metallic conducting property and the one with $x = 0.80$ showed minimum resistivity at room temperature (~ $1 \times 10^{-3}$ Ω-cm). The color of the samples varied from blue-black to purple to red with increasing strontium content from 0.70 to 0.85 and to 0.95. In normal metallic systems, electron-hole pairs can be excited by photons, however, they are difficult to separate due to lack of internal field.

However, metallic $Sr_xNbO_3$ compounds formed with $0.8 < x < 0.9$, where shown to be capable of light harvesting with potential for photocatalytic water splitting [39]. The efficiency for water splitting was attributed to high carrier mobility which could facilitate carrier separation though no evidence was presented.

The thin film studies of $Sr_xNbO_3$ ($x < 1$) were performed by very few groups [152-154]. Tomio et al first deposited a mixture of (100) - and (110) – oriented $Sr_{0.95}NbO_3$ films on $SrTiO_3$ (100) substrates by PLD [152]. The films were prepared under high temperature (770° C) and low oxygen pressure ($10^{-5}$ Torr). They had purple red color and low resistivity (3 X 10-4 Ohm-cm) at room temperature. Balasubramaniam et al deposited $SrNbO_3$ films on STO, LAO and MgO substrates in nitrogen ambient with pressure in the range of $10^{-3}$ to $10^{-1}$ Torr. They only focused on the structural analysis of the films. It was shown that epitaxial (100) – oriented $SrNbO_3$ films could be formed on both STO (100) and LAO (100) substrates, but not on MgO. The depositions were all performed under high temperature (> 750 °C) in oxygen deficient environment. In such conditions, oxygen vacancies might be generated, which drastically reduced the resistivity of STO substrates [155]. Hence to obtain the transport properties of $Sr_xNbO_3$ films more accurately, non-conducting substrates must be used.

The band structure of $SrNbO_3$ was constructed by DFT calculations, where the Fermi level was shown to lie within conduction band and 1.18 - 1.21 eV above the conduction band edge [147, 156]. The bandgap (energy difference between the half-filled band and highest fully filled band) was calculated as 2.79 eV for direct type and 2.31 – 2.38 eV for indirect type. The energy difference between the Fermi level and the lowest empty band was calculated as 1.8 eV [39]. Of course one must keep in mind that DFT calculations consistently underestimate bandgaps. The band structures of bulk $Sr_xNbO_3$ ($0.8 < x < 0.9$) were experimentally studied by Isawa et al by using x-ray and ultraviolet photoelectron spectroscopy (XPS and UPS) [157]. The conduction (half filled) band and valence (highest fully filled) band were attributed to mainly Nb 4*d* with some hybridization with O 2*p* states and mainly O 2*p* with some hybridization with Nb 4*d* states respectively. The Fermi level was found to be

located in the conduction band, which was consistent with the metallic transport behavior of the films and was about 4 eV above the valence band edge (O 2*p* states).

The experimental data of electronic transport, band structure and optical properties of thin film $Sr_xNbO_3$ ($x \leq 1$) are not available even today. In our work we fill this gap by successfully preparing epitaxial thin films and obtaining their structural, electronic and optical properties.

### 7.2 Experimental section

$SrNbO_{3+\delta}$ target were prepared by solid reactions of $SrCO_3$ and $NbO_2$ powders, which were mixed with molar ratio of 1: 1 and ground for one hour before calcinations in 5% $H_2$ – Ar gas at a temperature of 1200°C. Subsequently, the powder mixtures were ground again for one hour, and then been pressed into a solid pellet, which was sintered in the same gas ambient at 1300°C. The films were deposited from the target on LAO (100) substrate by PLD at a temperature of 750°C, laser energy density of 2 J/cm$^2$ (5 Hz) and oxygen partial pressure of ~ $10^{-5}$ Torr. 130 nm thick films were made with half an hour deposition. The crystal structures of the films were studied by XRD and HRTEM. Elemental contents (Sr, Nb and O ratio) in the films were measured by particle induced x-ray emissions (PIXE). Optical bandgap of the films were measured by UV-vis spectroscopy and the electronic structures were studied by XPS and UPS. PPMS was used to measure the electronic transport properties.

### 7.3 Results and discussions

The crystal structures of the films deposited under oxygen partial pressure in the range of $1 \times 10^{-5}$ Torr to $6 \times 10^{-5}$ Torr are shown in Fig. 7.1. The substrate peaks overlap, but the film peaks are found to shift with oxygen partial pressure. The black, red, green and blue peaks labeled as SNO (200) corresponding to the lattice parameters (*d*/2, *d* is the lattice constant) of 2.055 Å, 2.047 Å, 2.013 Å and 2.010 Å respectively, are seen to reduce with oxygen partial pressure. The rocking curves of the films are shown in the inset, where the full width at half maximum (FWHM) are 1.12°, 1.45°, 1.47° and 1.53° respectively, which increase with oxygen partial pressure. The large FWHM is

reasonable as the lattice mismatch of $SrNbO_{3+\delta}$ film and LAO substrate is above 8%. The bright spots of the films obtained from D8 2D detector indicate the epitaxial growth of $SrNbO_{3+\delta}$ on LAO, as shown as the background figure.

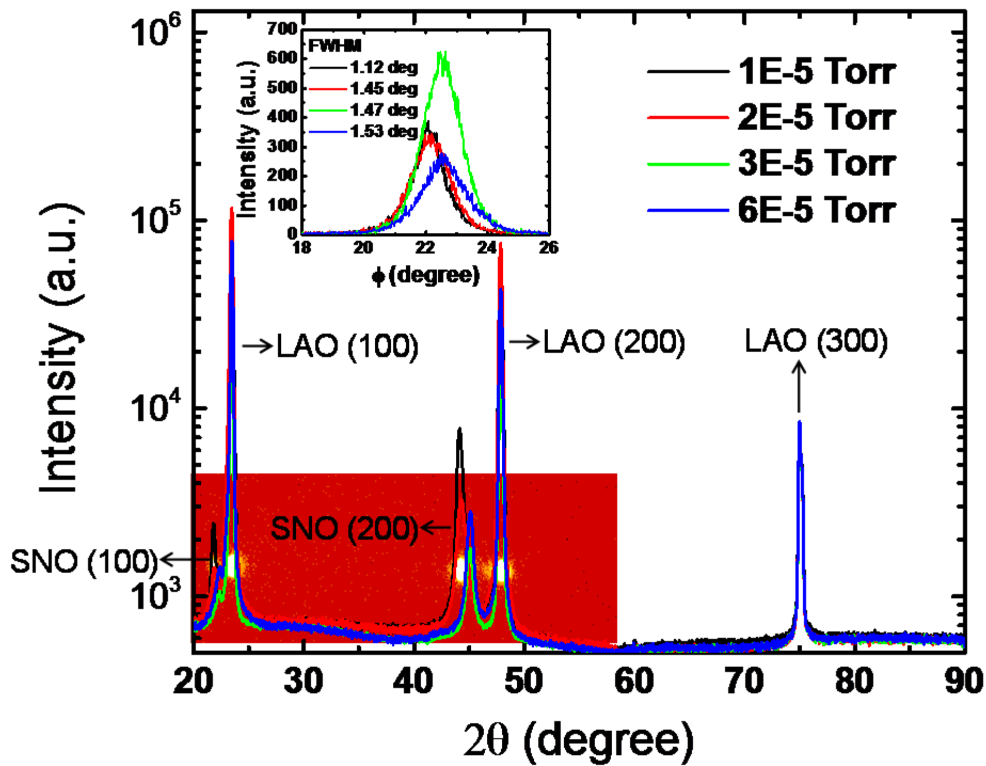


**Figure 7.1: XRD spectrum of $SrNbO_{3+\delta}$ films prepared at 750°C and different oxygen partial pressures. Labels LAO (*h*00) indicates the substrates' signal and SNO (*h*00) indicates the films' signal. Inset shows the rocking curve of the films at SNO (200) peaks. Background figure shows the 2D XRD patterns of SNO film on LAO substrate. The bright yellow spots are corresponding for particular peaks in 2θ plot.**

Fig. 7.2(a) shows the TEM image of $SrNbO_{3+\delta}$ film on LAO, where the film was deposited under $1 \times 10^{-5}$ Torr. The sharp interface clearly separates the film and the substrate. The atomic resolution images of $SrNbO_{3+\delta}$ and LAO are shown in (b) and (c). As Al and O atoms have low atomic weights, only La atom in the substrate can be imaged. In contrast, both Sr and Nb atoms can be imaged in the film, where the image indicates the (001) plane of the perovskite structure. The electron diffraction patterns of $SrNbO_{3+\delta}$ and LAO are shown in (d) and (e), where the lattice constant of the film and the substrate are measured as 4.09 ± 0.05 Å and 3.80 ± 0.05 Å respectively. Because of the large lattice mismatch between the film and the substrate, the out-of-plane (in-plane) lattice constant of the film is stretched (compressed) near the

interface and relaxes at the surface. However, the distortions are too small to be seen here. Hence the measured average lattice constant of LAO substrate is quite close to the actual value, and similarly the measured lattice constant of the film should be accurate.

The lattice parameters of $SrNbO_{3+\delta}$ obtained from XRD and TEM agree with each other. Hence we can conclude that $SrNbO_{3+\delta}$ thin films can form simple cubic perovskite structure on LAO substrate with the lattice parameter of around 4.10 Å, which decreases with oxygen partial pressure during deposition.

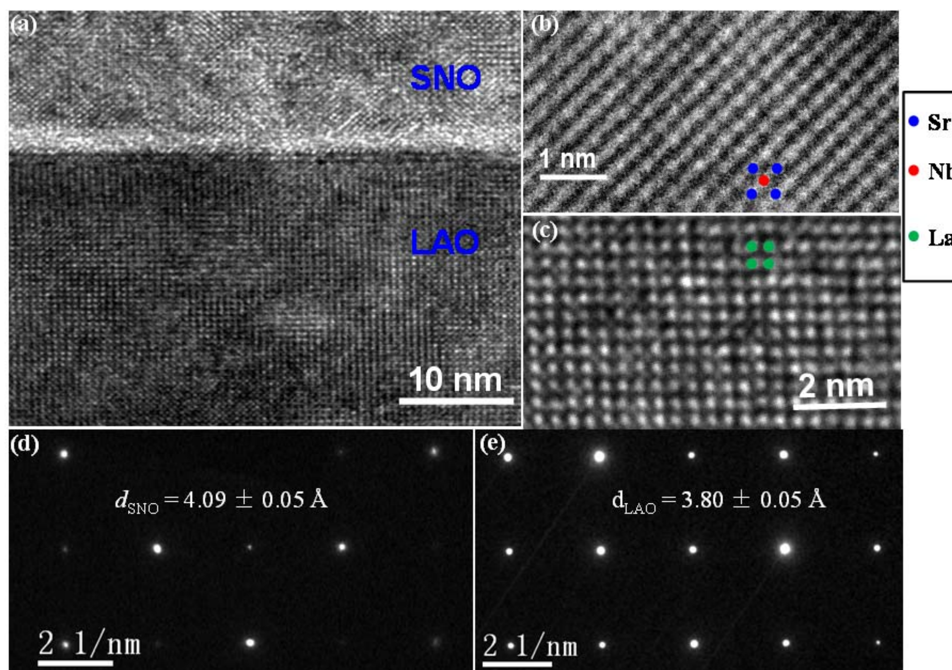


**Figure 7.2: (a) TEM image of $SrNbO_{3+\delta}$ film on LAO substrate. The film is prepared under 1 × $10^{-5}$ Torr. (b) Atomic resolution of $SrNbO_{3+\delta}$ film. (c) Atomic resolution of LAO substrate. (d) Electron diffraction pattern of $SrNbO_{3+\delta}$ film. (e) Electron diffraction pattern of LAO substrate.**

The UV- vis transmission spectrums of the films are shown in Fig. 7.3(a) and the corresponding Tauc plots with indirect band model are shown in Fig. 7.3(b). The absorption edges near 300 nm are almost overlapped, which indicates the optical bandgap of the samples does not depend upon the oxygen pressure. The transmission of the films increases with oxygen partial pressure when the wavelength is above 600 nm. The drop of the transmission with wavelength (above 600 nm) may be explained by the Drude model, which normally appears in metallic systems. The optical bandgaps of the films fitted from Tauc plot are between 3.8 eV and 4.0 eV, which are larger than the calculated energy difference of the Fermi level and the valence band edge. The deviation may come from the under estimation of the bandgaps by DFT calculations. Interestingly, the optical bandgap keeps decreasing with oxygen partial pressure, which may indicate the shifting of the Fermi level away from the vacuum level with increasing oxygen content. In that case, we should expect the drop of the resistivity with oxygen partial pressure and we could estimate the width of the half-filled band from that.

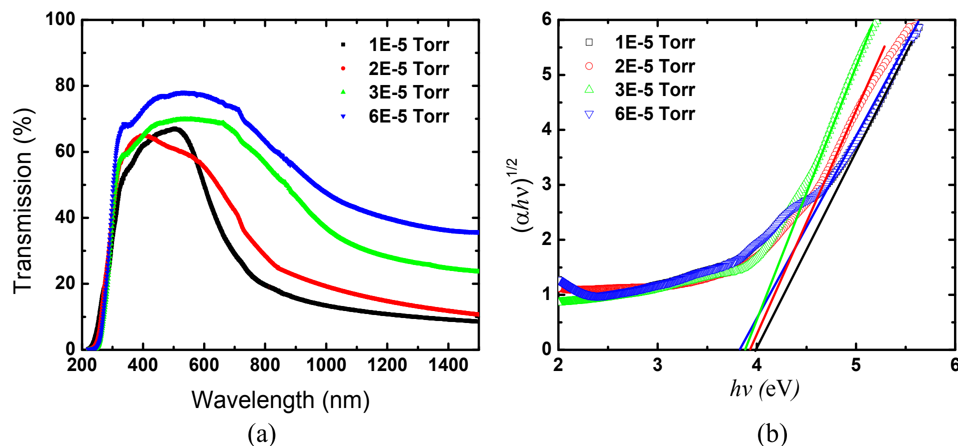


**Figure 7.3: (a) Transmission of the films prepared under 750°C and series of oxygen partial pressures. (b) Tauc plot of the spectrums in (a).**

The resistivity of $SrNbO_{3+\delta}$ film prepared under $1 \times 10^{-5}$ Torr and 750°C shows weak temperature dependence, as shown in Fig. 7.4, where metallic transport behavior is clearly visible. The resistivity at room temperature is around $1.8 \times 10^{-4}$ Ω-cm, which is comparable with that of commercial TCOs. The inset shows the resistivity of the films at room temperature, which indeed increases with oxygen partial pressure (the resistivity of the sample prepared

under 6 × $10^{-5}$ Torr overloads PPMS's capability, which should be above 100 Ω-cm). The sample prepared under 3 × $10^{-5}$ Torr shows semiconducting behavior (not shown here), which is due to the thermal excitation of electrons from donor states (Fermi level here) to the conduction band. Under the same condition, the optical bandgap of the sample decreases by about 0.2 eV. Assuming that the electronic bandgap is rigid, the changes of the optical bandgap should be totally attributed to the shifting of the Fermi level. Hence we can estimate that the half-filled band width of the sample prepared under 1 × $10^{-5}$ Torr is close to 0.2 eV.

The inset shows the pivotal role of oxygen partial pressure in producing conducting $SrNbO_{3+\delta}$, which resistivity can be reduced to $10^{-4}$ Ω-cm only when the oxygen partial pressure is below 2 × $10^{-5}$ Torr.

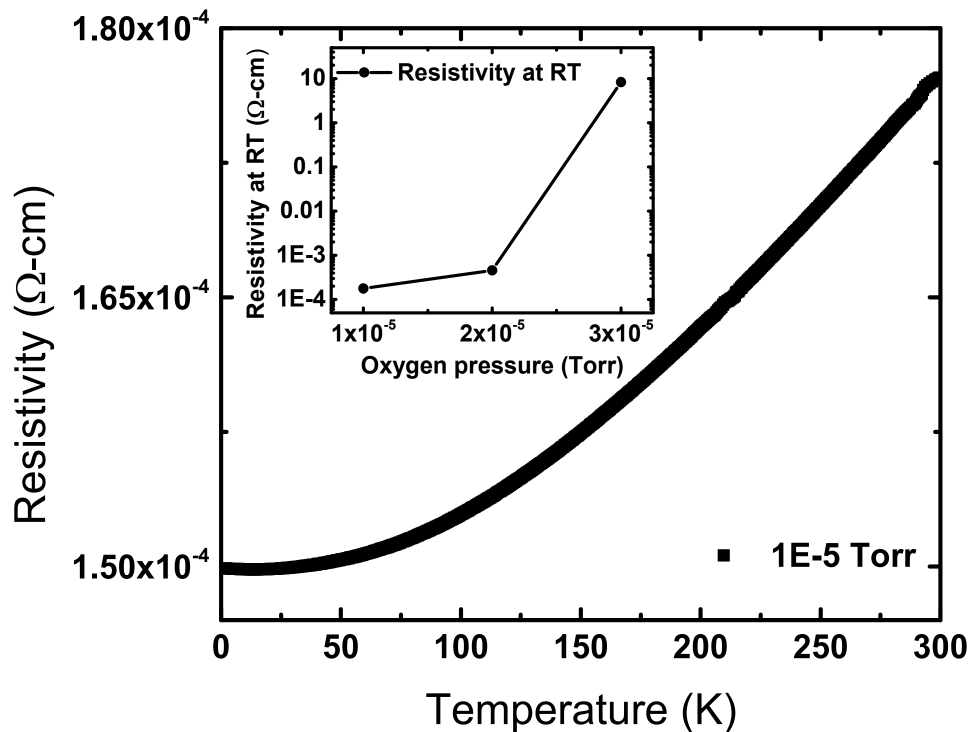


**Figure 7.4: Temperature dependent resistivity of the sample prepared under 750°C and 1 × $10^{-5}$ Torr. Inset shows the room temperature resistivity of the samples as a function of the oxygen partial pressures.**

The charge carrier density (*n*-type) and mobility of the sample prepared under 750°C and 1 × $10^{-5}$ Torr are shown in Fig. 7.5, both of which are weakly dependent on temperature. The carrier density reaches 1.43 × $10^{22}$/$cm^3$ at room temperature, where such large value is only observed in metallic oxide

systems [39, 158, 159]. The electronic configuration of Nb is [Kr]$5s^1 4d^4$. In $SrNbO_3$, each Nb atom donates four electrons to the neighboring six O atoms, leaving one electron in its 5*s* orbital. Assuming that the free charge carriers are all contributed by the left over 5*s* electrons, the theoretical carrier density of $SrNbO_3$ can be calculated as $1.45 \times 10^{22}/cm^3$. As the measured value has little discrepancy with the theoretical value, one can believe that most of Nb atoms are formed in $Nb^{5+}$ states and the discrepancy may come from a small number of $Nb^{4+}$ states (4 electrons are donated to O and the fifth electron is strongly bonded). The mobility is only around 2.5 $cm^2/Vs$ at room temperature, which may be not adequate to separate carriers generated by photons as proposed in ref. [39].

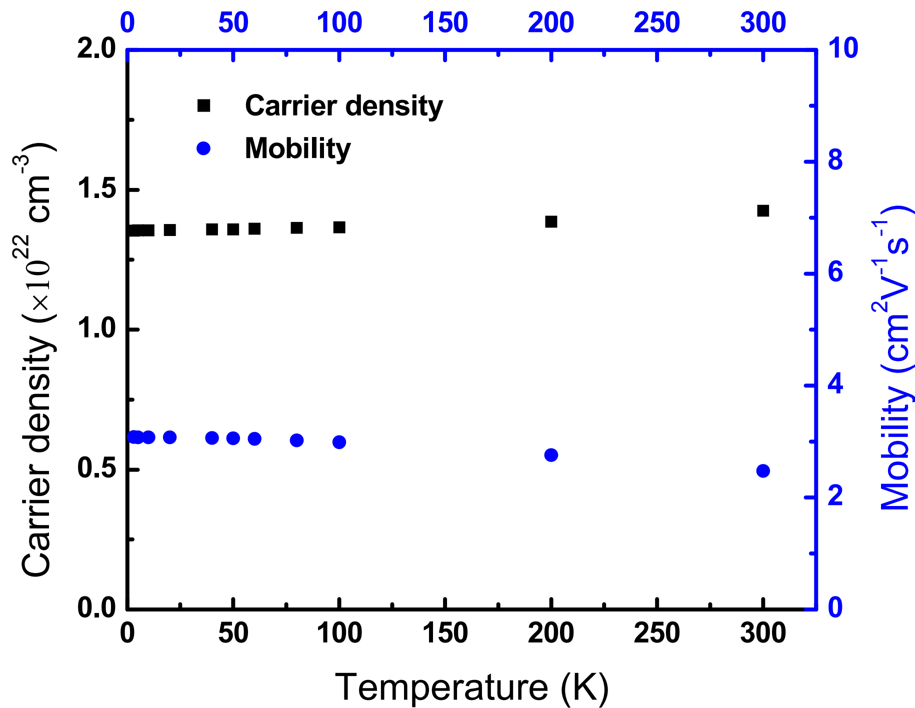


**Figure 7.5: Temperature dependent charge carrier density and mobility of $SrNbO_{3+\delta}$ film on LAO substrate. The film was deposited under $1 \times 10^{-5}$ Torr.**

The effective oxidation state of Nb at the surface of $SrNbO_{3+\delta}$ film deposited under $1 \times 10^{-5}$ Torr was measured by XPS, as shown in Fig. 7.6(a). The binding energies of Nb 3*d* states (referenced to the adventitious C 1*s* peak, i.e. 284.5 eV) could be simulated by superposition of two sets of envelopes, where the corresponding $3d_{5/2}$ peaks locate at 206.63 eV and 204.12 eV respectively. These values are very close to the observed binding energies of Nb $3d_{5/2}$ for

$Nb^{5+}$ and $Nb^{4+}$ by other researchers [157, 160]. The intensities of the peaks indicate the content of the corresponding items ($Nb^{5+}$:$Nb^{4+}$ = 6.4:1). Hence most of surface Nb atoms exist as $Nb^{5+}$, which is consistent with our previous expectation. To obtain the niobium's valence state in the bulk of $SrNbO_{3+\delta}$ film, XAS study is required. Fig. 7.6(b) and (c) show the work function and the energy difference between the Fermi level and the valence band edge as 3.73 eV and 3.80 eV respectively, where the latter is close to the measured optical bandgap of the film (4.0 eV), as expected.

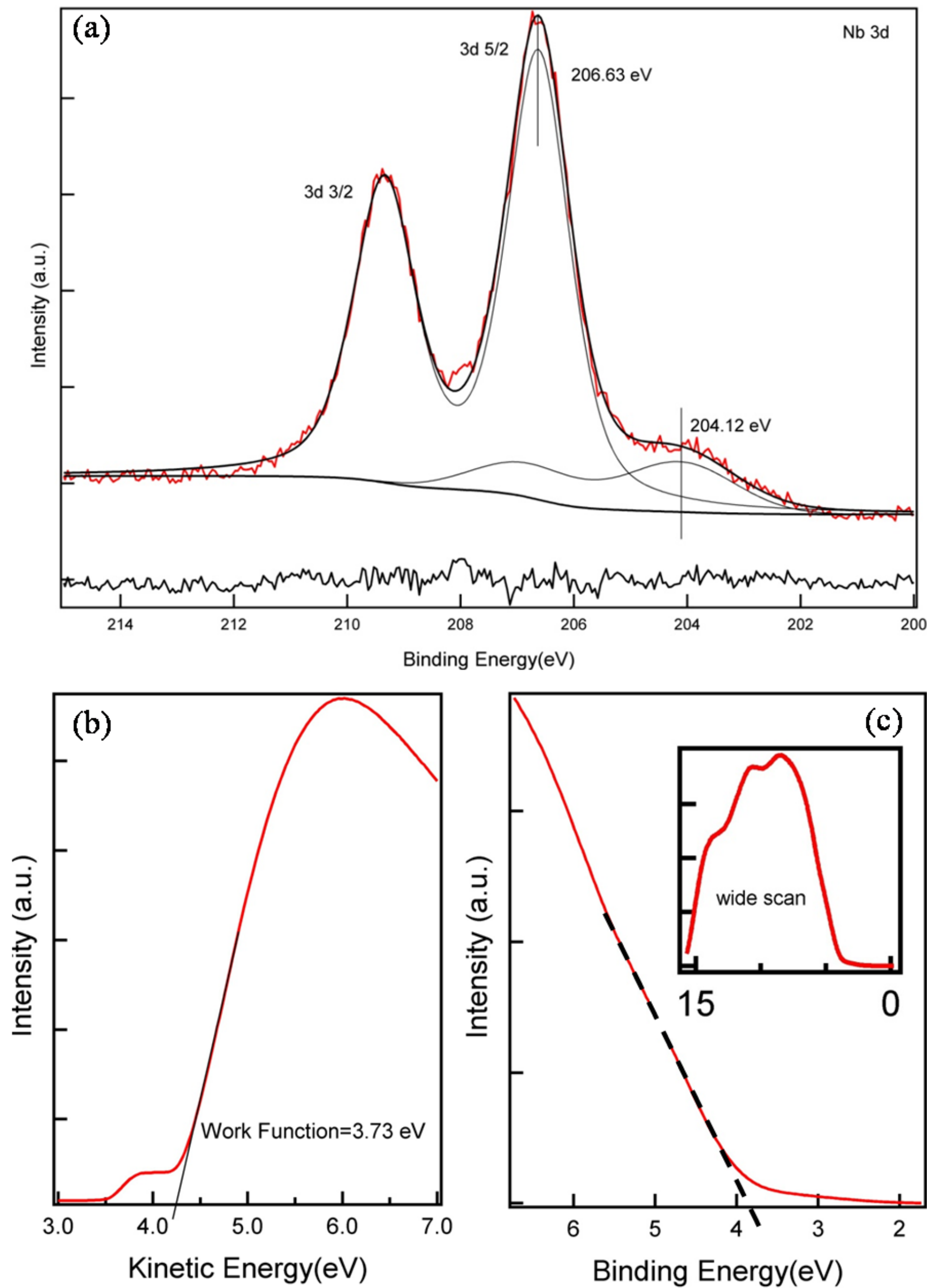


**Figure 7.6: (a) X–ray photoelectron spectroscopy of $SrNbO_{3+\delta}$ film prepared under 750°C and 1 × $10^{-5}$ Torr. The binding energies were referenced to the adventitious C 1*s* peak (284.5 eV). The spectrum is simulated by superposition of two sets of Nb 3*d* peaks where the $3d_{5/2}$ peaks for $Nb^{5+}$ and $Nb^{4+}$ are located at 206.63 eV and 204.12 eV respectively. The ratio of the peak area intensity of $Nb^{5+}$ and $Nb^{4+}$ is about 6.4:1. (b) Ultraviolet photoelectron spectroscopy of the film in (a). The beam energy is 21.2 eV. The work function of the electron analyzer was calibrated as 4.47 eV. 5 V bias was applied to the sample. Kinetic energy of the secondary edge was measured as 4.26 eV, as indicated by the black line cutting off the horizontal axis. (c) Energy difference between the Fermi level and valence band edge. Fermi level was calibrated as 0 binding energy. Inset shows the wide scan of the spectrum.**

The lattice constant, optical bandgap and transport properties of $SrNbO_{3+\delta}$ films are all dependent on the oxygen partial pressure during deposition. How are the atomic contents of Sr, Nb and O affected by the pressure? Fig. 7.7 shows the PIXE measurement of the films deposited under different oxygen partial pressures. The spectra overlap with each other which indicate the constant Sr to Nb atomic ratio with deposition pressure. Hence the different performances in crystal structural, optical and electronic properties of the films are entirely attributed to O content in $SrNbO_{3+\delta}$ film. Isawa observed the hybridization of Nb 4*d* and O 2*p* states in the conduction band of bulk $Sr_xNbO_3$ ($0.8 < x < 0.9$) [157]. We think it also happens in our current study. Increasing oxygen content may break this hybridization and localize the electrons.

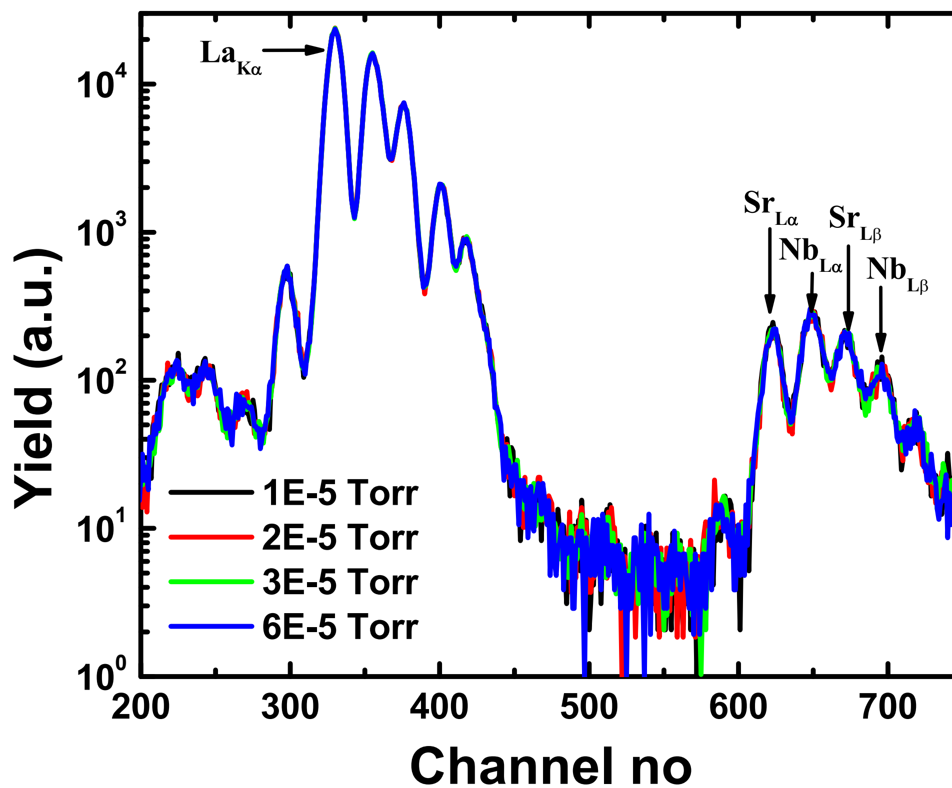


**Figure 7.7: Particle (proton) induced x-ray emission spectrum of $SrNbO_{3+\delta}$ films deposited on LAO substrate under different oxygen partial pressures. Peaks corresponding to particular element are labeled.**

### 7.4 Summary

Epitaxial $SrNbO_{3+\delta}$ films were deposited on LAO substrate at different oxygen partial pressures. It forms cubic perovskite structure with the lattice constant

of 4.10 Å. δ is strongly dependent on the preparation pressures and it was estimated to be close to zero at $1 \times 10^{-5}$ Torr. The optical bandgap of $SrNbO_{3+\delta}$ films was measured as close to 4.0 eV. The resistivity of the sample prepared at $1 \times 10^{-5}$ Torr was measured as close to $1.8 \times 10^{-4}$Ω-cm and it is weakly dependent of the measurement temperature. The low resistivity of the sample is attributed to the high charge carrier density, which reaches $1.43 \times 10^{22}/cm^3$ at room temperature. The mobility is only around 2.5 $cm^2/Vs$ at room temperature. XPS studies showed the niobium's valence state as close to 5+ near the surface and UPS studies verified the measured optical bandgap.

# Chapter 8 Summary and outlook

## 8.1 Summary

In this thesis some basic and well known properties of $TiO_2$ have been introduced and newly discovered properties in this thesis work, such as the shift of energy band levels with Ta concentration, metal to insulator transition and transition of transport mechanisms at low temperatures for $TiO_2$ thin film upon Ta doping have been described in detail. In addition, we have studied Ni impurity mediated reversible ferromagnetism in rutile $TiO_2$ substrate upon annealing. Besides $TiO_2$, we have studied another TCOs material $SrNbO_{3+\delta}$ which has optical bandgap close to 4 eV and also has potential application as photocatalyst in water splitting. The $TiO_2$ work is summarized in two parts here: transport properties of anatase films and magnetic properties of rutile substrate.

### 8.1.1Transport properties of anatase $TiO_2$ thin film

Pure anatase $TiO_2$ thin films (single crystal) were prepared by PLD technique onto LAO substrate. The samples showed semiconducting behavior in the whole measuring temperature range (2 K to 300 K) or a partial range (below 170 K) with different oxygen partial pressures during deposition. Near $1.4 \times 10^{-5}$ Torr, a resistivity minimum was found, which was attributed to the competition of donor (oxygen vacancies) and acceptor states (compensating defects). The transport property at low temperatures followed variable range hopping mechanism, which was caused by oxygen vacancy (participate in low oxygen pressure) induced random potentials. When the film was doped with Ta (0.1% to 0.4% atomic ratio), the crossover temperature (below which semiconducting trend was followed and above which metallic trend was followed) decreased with Ta concentration. Besides, weak localization became dominant in the doped samples while strong localization dominated in the pure $TiO_2$ films.

When the Ta doping concentration became larger (> 1%), completely metallic transport behavior of anatase film was obtained. It was shown that Ta incorporation pushed upwards both the conduction and valence band edges, with the effect stronger with the conduction band resulting in an increase in the bandgap. By measuring the energy level shifts with Ta concentration, it

was proposed that $TiO_2$ thin film should become degenerate when Ta concentration exceeds 0.8%, which was close to the measured experimental data (0.4%).

8.1.2 Ferromagnetism of rutile $TiO_2$ substrate induced by Nickel impurity

As received $TiO_2$ substrate was found to be insulating and paramagnetic. However, after annealing in vacuum ($5 \times 10^{-6}$ Torr) with temperature exceeding 600°C, it became ferromagnetic and conductive. After annealing in air, the same substrate returned to its initial state (insulating and paramagnetic). Verifying with several techniques (SIMS, RBS, TEM, XAS), it was shown that Ni clusters segregated to the surface of the sample when it was annealed in vacuum and dispersed back when it was annealed in air, consistent with the reversible behavior of the magnetic properties. As the substrates were provided by three vendors located at USA, Europe and Japan separately, it was highly suspected that this phenomenon was universal, at least for commercial $TiO_2$. Hence it is crucial for researchers to double check the magnetic impurity content in the substrate (not limited to $TiO_2$) processed at the same condition of the thin film preparation.

8.1.3 Structural, transport and optical properties of $SrNbO_3$

Strontium niobate, a large bandgap conducting oxide, was found to form in cubic perovskite structure on LAO substrate with the lattice constant close to 4.1 Å. The optical bandgap was measured to be 4.0 eV and it slightly decreased with oxygen partial pressure during deposition. An XPS study of the film was performed, where niobium's valence state was closer to 5+ rather than 4+. The resistivity ($\sim 1.8 \times 10^{-4} \Omega$-cm) at room temperature was comparable to commercial TCOs and was attributed to the large charge carrier density ($\sim 1.4 \times 10^{22} cm^{-3}$) despite the low mobility ($\sim 2.5. cm^2V^{-1}s^{-1}$) measured. Hence we question enhanced electron-hole separation in $Sr_xNbO_3$ ($0.8 < x < 0.95$) for photocatalytic water splitting on account of such low mobility [39].

## 8.2 Outlook

We have shown that the optical bandgap of $TiO_2$ film in anatase phase can be enlarged continuously by Ta incorporation (maximum 0.2 eV by 25% of Ta incorporation, Appendix 6), which may push its CB edge towards vacuum level. As $TiO_2$ plays a very important role in energy conversion process such

as DSC, water splitting and $CO_2$ reduction, and all of these processes are related to the CB edge of $TiO_2$, it is very interesting to setup experiments which will compare the efficiency and product types, for example in $CO_2$ reduction process, by using different Ta doped $TiO_2$ versus pure $TiO_2$ thin films. To implement this assumption, we are facing a big challenge. The entire conclusion we have obtained is based on the studies of single crystalline $TiO_2$ thin film in anatase phase. Whether it is applicable to bulk or Nano-size $TiO_2$ in rutile phase needs more investigations.

Besides, as Ta doped $TiO_2$ is an n type semiconductor, if somehow a p type $TiO_2$ can be prepared, the future of this material will be brighter. Up till now, some stable trivalent ($Al^{3+}$, $Ga^{3+}$, $La^{3+}$, $Er^{3+}$, $Ho^{3+}$, and $Nd^{3+}$) and divalent ($Cu^{2+}$) elements have been introduced into $TiO_2$ lattice in quest for p type conductivity. Unfortunately, none of them worked, possibly because none of them make a shallow acceptor level near the VB edge. In future, probably anionic doping like $N^{3-}$ can be explored.

Another important issue worth pursuing is the specific atom content in $SrNbO_3$ film and also the lattice locations of Sr and Nb which is difficult to be analyzed by RBS as the atomic weights of Sr and Nb are too close to be separated in the spectrum. When Sr is replaced by Ca or Ba, such problem can be solved beautifully. Hence it is important to study the corresponding properties of $CaNbO_3$ and $BaNbO_3$ epitaxial films.

# BIBLIOGRAPHY

1. Fujishima, A., T.N. Rao, and D.A. Tryk, *TiO(2) photocatalysts and diamond electrodes.* Electrochimica Acta, 2000. **45**(28): p. 4683-4690.

2. Chan, Y.C., J.N. Chen, and M.C. Lu, *Intermediate inhibition in the heterogeneous UV-catalysis using a TiO2 suspension system.* Chemosphere, 2001. **45**(1): p. 29-35.

3. Yu, J.C., et al., *Effects of F- doping on the photocatalytic activity and microstructures of nanocrystalline TiO2 powders.* Chemistry of Materials, 2002. **14**(9): p. 3808-3816.

4. Oregan, B. and M. Gratzel, *A Low-Cost, High-Efficiency Solar-Cell Based on Dye-Sensitized Colloidal Tio2 Films.* Nature, 1991. **353**(6346): p. 737-740.

5. Asahi, R., et al., *Visible-light photocatalysis in nitrogen-doped titanium oxides.* Science, 2001. **293**(5528): p. 269-271.

6. Yamashita, H., et al., *Degradation of propanol diluted in water under visible light irradiation using metal ion-implanted titanium dioxide photocatalysts.* Journal of Photochemistry and Photobiology a-Chemistry, 2002. **148**(1-3): p. 257-261.

7. Kato, H. and A. Kudo, *Visible-light-response and photocatalytic activities of TiO2 and SrTiO3 photocatalysts codoped with antimony and chromium.* Journal of Physical Chemistry B, 2002. **106**(19): p. 5029-5034.

8. Ruiz, A.M., et al., *Cr-doped TiO2 gas sensor for exhaust NO2 monitoring.* Sensors and Actuators B-Chemical, 2003. **93**(1-3): p. 509-518.

9. Wang, Y.M., et al., *Nanostructured sheets of Ti-O nanobelts for gas sensing and antibacterial applications.* Advanced Functional Materials, 2008. **18**(7): p. 1131-1137.

10. Chen, Y.W., et al., *Atomic layer-deposited tunnel oxide stabilizes silicon photoanodes for water oxidation.* Nature Materials, 2011. **10**(7): p. 539-544.

11. Albertin, K.F. and I. Pereyra, *Study of reactive sputtering titanium oxide for metal-oxide-semiconductor capacitors.* Thin Solid Films, 2009. **517**(16): p. 4548-4554.

12. Moriguchi, I., et al., *A mesoporous nanocomposite of TiO2 and carbon nanotubes as a high-rate Li-intercalation electrode material.* Advanced Materials, 2006. **18**(1): p. 69-73.

13. Dinh, N.N., et al., *Electrochromic properties of TiO2 anatase thin films prepared by a dipping sol-gel method.* Thin Solid Films, 2003. **423**(1): p. 70-76.

14. Matsunaga, T., et al., *Photoelectrochemical Sterilization of Microbial-Cells by Semiconductor Powders.* Fems Microbiology Letters, 1985.

**29**(1-2): p. 211-214.

15. Cai, R.X., et al., *Induction of Cytotoxicity by Photoexcited Tio2 Particles.* Cancer Research, 1992. **52**(8): p. 2346-2348.

16. Morikawa, T., et al., *Band-gap narrowing of titanium dioxide by nitrogen doping.* Japanese Journal of Applied Physics Part 2-Letters, 2001. **40**(6A): p. L561-L563.

17. Lindgren, T., et al., *Photoelectrochemical and optical properties of nitrogen doped titanium dioxide films prepared by reactive DC magnetron sputtering.* Journal of Physical Chemistry B, 2003. **107**(24): p. 5709-5716.

18. Diwald, O., et al., *Photochemical activity of nitrogen-doped rutile TiO2(111) in visible light.* Journal of Physical Chemistry B, 2004. **108**(19): p. 6004-6008.

19. Umebayashi, T., et al., *Band gap narrowing of titanium dioxide by sulfur doping.* Applied Physics Letters, 2002. **81**(3): p. 454-456.

20. Serpone, N., *Is the band gap of pristine TiO2 narrowed by anion- and cation-doping of titanium dioxide in second-generation photocatalysts?* Journal of Physical Chemistry B, 2006. **110**(48): p. 24287-24293.

21. Irie, H., Y. Watanabe, and K. Hashimoto, *Nitrogen-concentration dependence on photocatalytic activity of TiO2-xNx powders.* Journal of Physical Chemistry B, 2003. **107**(23): p. 5483-5486.

22. Di Valentin, C., G. Pacchioni, and A. Selloni, *Origin of the different photoactivity of N-doped anatase and rutile TiO2.* Physical Review B, 2004. **70**(8).

23. Sakthivel, S., M. Janczarek, and H. Kisch, *Visible light activity and photoelectrochemical properties of nitrogen-doped TiO2.* Journal of Physical Chemistry B, 2004. **108**(50): p. 19384-19387.

24. Nakamura, R., T. Tanaka, and Y. Nakato, *Mechanism for visible light responses in anodic photocurrents at N-doped TiO2 film electrodes.* Journal of Physical Chemistry B, 2004. **108**(30): p. 10617-10620.

25. Chen, H.Y., H.X. Jin, and B. Dong, *Preparation of magnetically supported chromium and sulfur co-doped TiO2 and use for photocatalysis under visible light.* Research on Chemical Intermediates, 2012. **38**(9): p. 2335-2342.

26. Zhao, Y.H., et al., *Electronic structure and electrocatalytic activity of cerium-doped tantalum oxide.* Journal of Electroanalytical Chemistry, 2012. **681**: p. 139-143.

27. Anpo, M., et al., *Design of unique titanium oxide photocatalysts by an advanced metal ion-implantation method and photocatalytic reactions under visible light irradiation.* Research on Chemical Intermediates, 1998. **24**(2): p.

143-149.

28. Anpo, M., et al., *Design and development of titanium oxide photocatalysts operating under visible and UV light irradiation. The applications of metal ion-implantation techniques to semiconducting TiO2 and Ti/zeolite catalysts.* Current Opinion in Solid State & Materials Science, 2002. **6**(5): p. 381-388.

29. Zhou, J.K., et al., *Enhancement of photocatalytic activity of P25TiO(2) by vanadium-ion implantation under visible light irradiation.* Journal of Colloid and Interface Science, 2007. **311**(2): p. 497-501.

30. Barman, A.R., et al., *Multifunctional Ti1-xTaxO2: Ta doping or alloying?* Applied Physics Letters, 2011. **98**(7).

31. Shinde, S.R., et al., *Co-occurrence of superparamagnetism and anomalous Hall effect in highly reduced cobalt-doped rutile TiO2-delta films.* Physical Review Letters, 2004. **92**(16).

32. Zhang, S.X., et al., *Magnetism and anomalous hall effect in Co-(La,Sr)TiO3.* Physical Review B, 2007. **76**(8).

33. Duhalde, S., et al., *Appearance of room-temperature ferromagnetism in Cu-doped TiO2-delta films.* Physical Review B, 2005. **72**(16).

34. Osorio-Guillen, J., S. Lany, and A. Zunger, *Atomic control of conductivity versus ferromagnetism in wide-gap oxides via selective doping: V, Nb, Ta in anatase TiO(2).* Physical Review Letters, 2008. **100**(3).

35. Durst, A.C., R.N. Bhatt, and P.A. Wolff, *Bound magnetic polaron interactions in insulating doped diluted magnetic semiconductors.* Physical Review B, 2002. **65**(23).

36. Diebold, U., *The surface science of titanium dioxide.* Surface Science Reports, 2003. **48**(5-8): p. 53-229.

37. Matsumoto, Y., et al., *Room-temperature ferromagnetism in transparent transition metal-doped titanium dioxide.* Science, 2001. **291**(5505): p. 854-856.

38. Yee, S.M.M., D.A. Crandles, and L.V. Goncharova, *Ferromagnetism on the unpolished surfaces of single crystal metal oxide substrates.* Journal of Applied Physics, 2011. **110**(3).

39. Xu, X.X., et al., *A red metallic oxide photocatalyst.* Nature Materials, 2012. **11**(7): p. 595-598.

40. Babu, V.S., *Solid State Devices And Technology*. 3 ed. 2010, Bangalore: Sanguine Technical Publishers.

41. Zhang, S., *Unusual electronic transport and magnetism in titanium oxide based semiconductors and metals*, in *Physics*. 2007, University of maryland.

42. Seeger, K., *Semiconductor Physics: An Introduction*. 9 ed. 2004, Berlin; New York: Springer-Verlag.

43. Grahn, H.T., *Introduction to Semiconductor Physics*. 1999, Singapore: World Scientific.

44. Grant, F.A., *Properties of Rutile (Titanium Dioxide).* Reviews of Modern Physics, 1959. **31**(3): p. 646-674.

45. Samsonov, G.V., *The Oxide Handbook*. 2nd ed. 1982, New York: IFI/Plenum Data Corp.

46. Howard, C.J., T.M. Sabine, and F. Dickson, *Structural and Thermal Parameters for Rutile and Anatase.* Acta Crystallographica Section B-Structural Science, 1991. **47**: p. 462-468.

47. Burdett, J.K., et al., *Structural Electronic Relationships in Inorganic Solids - Powder Neutron-Diffraction Studies of the Rutile and Anatase Polymorphs of Titanium-Dioxide at 15 and 295-K.* Journal of the American Chemical Society, 1987. **109**(12): p. 3639-3646.

48. Mo, S.D. and W.Y. Ching, *Electronic and Optical-Properties of 3 Phases of Titanium-Dioxide - Rutile, Anatase, and Brookite.* Physical Review B, 1995. **51**(19): p. 13023-13032.

49. Muscat, J., V. Swamy, and N.M. Harrison, *First-principles calculations of the phase stability of TiO2.* Physical Review B, 2002. **65**(22).

50. Kim, J.H., S. Lee, and H.S. Im, *The effect of target density and its morphology on TiO2 thin films grown on Si(100) by PLD.* Applied Surface Science, 1999. **151**(1-2): p. 6-16.

51. Hanaor, D.A.H. and C.C. Sorrell, *Review of the anatase to rutile phase transformation.* Journal of Materials Science, 2011. **46**(4): p. 855-874.

52. Lotnyk, A., S. Senz, and D. Hesse, *Formation of BaTiO3 thin films from (110) TiO2 rutile single crystals and BaCO3 by solid state reactions.* Solid State Ionics, 2006. **177**(5-6): p. 429-436.

53. Wang, H. and J.P. Lewis, *Second-generation photocatalytic materials: anion-doped TiO2.* Journal of Physics-Condensed Matter, 2006. **18**(2): p. 421-434.

54. Fulde, P., *Electron Correlations in Molecules and Solids*. 1995, Berlin; New York: Springer-Verlag.

55. Tang, H., et al., *Photoluminescence in Tio2 Anatase Single-Crystals.* Solid State Communications, 1993. **87**(9): p. 847-850.

56. Pascual, J., J. Camassel, and H. Mathieu, *Fine-Structure in the Intrinsic Absorption-Edge of Tio2.* Physical Review B, 1978. **18**(10): p. 5606-5614.

57. Zhang, S.X., et al., *Niobium doped TiO2: Intrinsic transparent metallic anatase versus highly resistive rutile phase.* Journal of Applied Physics, 2007. **102**(1).

58. Forro, L., et al., *High-Mobility N-Type Charge-Carriers in Large Single-Crystals of Anatase (Tio2).* Journal of Applied Physics, 1994. **75**(1): p. 633-635.

59. Jennings, J.R., et al., *Dye-sensitized solar cells based on oriented TiO2 nanotube arrays: Transport, trapping, and transfer of electrons.* Journal of the American Chemical Society, 2008. **130**(40): p. 13364-13372.

60. Gesenhues, U., *Al-doped TiO(2) pigments: influence of doping on the photocatalytic degradation of alkyd resins.* Journal of Photochemistry and Photobiology a-Chemistry, 2001. **139**(2-3): p. 243-251.

61. Minami, T., *Transparent conducting oxide semiconductors for transparent electrodes.* Semiconductor Science and Technology, 2005. **20**(4): p. S35-S44.

62. Exarhos, G.J. and X.D. Zhou, *Discovery-based design of transparent conducting oxide films.* Thin Solid Films, 2007. **515**(18): p. 7025-7052.

63. Furubayashi, Y., et al., *A transparent metal: Nb-doped anatase TiO2.* Applied Physics Letters, 2005. **86**(25).

64. Hitosugi, T., et al., *Ta-doped anatase TiO2 epitaxial film as transparent conducting oxide.* Japanese Journal of Applied Physics Part 2-Letters & Express Letters, 2005. **44**(33-36): p. L1063-L1065.

65. Fujishima, A. and K. Honda, *Electrochemical Photolysis of Water at a Semiconductor Electrode.* Nature, 1972. **238**(5358): p. 37-+.

66. Zou, Z.G., et al., *Direct splitting of water under visible light irradiation with an oxide semiconductor photocatalyst.* Nature, 2001. **414**(6864): p. 625-627.

67. van de Krol, R., Y.Q. Liang, and J. Schoonman, *Solar hydrogen production with nanostructured metal oxides.* Journal of Materials Chemistry, 2008. **18**(20): p. 2311-2320.

68. W.C. Chu, J.W.M., Marc.A.Nicolet, ed. *Backscattering Spectroscopy*. 1978, Academica Press: Florida.

69. Mayer, M., *Rutherford Backscattering Spectrometry (RBS)*, in *Workshop on Nuclear Data for Science and Technology Materials Analysis*. 2003, Euratom Association: Germany.

70. Bierwagen, O., et al., *Causes of incorrect carrier-type identification in van der Pauw-Hall measurements.* Applied Physics Letters, 2008. **93**(24).

71. Josephson, B.D., *Possible New Effects in Superconductive Tunnelling.* Physics Letters, 1962. **1**(7): p. 251-253.

72. Jaklevic, R.C., et al., *Quantum Interference Effects in Josephson Tunneling.* Physical Review Letters, 1964. **12**(7): p. 159-&.

73. Clarke, J. and A.I. Braginski, *The SQUID Handbook: Applications of SQUIDs and SQUID Systems*. 2006, Weinheim, Germany: Wiley-VCH.

74. Yano, J. and V.K. Yachandra, *X-ray absorption spectroscopy.* Photosynthesis Research, 2009. **102**(2-3): p. 241-254.

75. Zhao, Y.L., et al., *Variable range hopping in TiO2 insulating layers for oxide electronic devices.* Aip Advances, 2012. **2**(1).

76. Holstein, T., *Hall Effect in Impurity Conduction.* Physical Review, 1961. **124**(5): p. 1329-&.

77. Mott, N.F., *Conduction in Non-Crystalline Materials*. 2nd ed. 1993, Oxford: Clarendon Press.

78. Feng, D. and G. Jin, *Introduction to Condensed Matter Physics: Volume 1*. Vol. 1. 2005, Singapore: World Scientific.

79. Shklovskii, B.I. and A.L. Efros, *Electronic Properties of Doped Semiconductors*. 1984, Berlin; New York: Springer-Verlag.

80. Hornung, M., et al., *Analysis of variable-range hopping conductivity in Si : P.* Physica Status Solidi B-Basic Research, 2000. **218**(1): p. 75-81.

81. Su, T.I., et al., *Magnetoresistance of Al70Pd22.5Re7.5 quasicrystals in the variable-range hopping regime.* Physical Review B, 2002. **66**(5).

82. Koon, D.W. and T.G. Castner, *Variable-Range Hopping and the Hall-Coefficient in Si-As.* Solid State Communications, 1987. **64**(1): p. 11-14.

83. Gruenewald, M., et al., *The Hopping Hall-Mobility - a Percolation Approach.* Solid State Communications, 1981. **38**(11): p. 1011-1014.

84. Mikoshiba, N., *Strong-Field Magnetoresistance of Impurity Conduction in N-Type Germanium.* Physical Review, 1962. **127**(6): p. 1962-&.

85. Malinowski, A., M.Z. Cieplak, and M. Berkowski, *Variable range hopping in the spin-glass phase of La2-xSrxCuO4.* Journal of Physics-Condensed Matter, 2008. **20**(8).

86. Hill, R.M., *Observation of Variable Range Hopping.* Physica Status Solidi a-Applied Research, 1976. **35**(1): p. K29-K34.

87. Zabrodskii, A.G. and K.N. Zinoveva, *Conductivity in the Metal-Dielectric Transition Range and Its Application in Wide-Range Low-Temperature Converters.* Fizika Nizkikh Temperatur, 1984. **10**(11): p. 1151-1159.

88. Kitada, A., et al., *Highly Reduced Anatase TiO2-delta Thin Films Obtained via Low-Temperature Reduction.* Applied Physics Express, 2011.

**4**(3).

89. Hasiguti, R.R. and E. Yagi, *Electrical-Conductivity Below 3-K of Slightly Reduced Oxygen-Deficient Rutile Tio(2-X).* Physical Review B, 1994. **49**(11): p. 7251-7256.

90. Edwards, P.P. and M.J. Sienko, *Universality Aspects of Metal-Nonmetal Transition in Condensed Media.* Physical Review B, 1978. **17**(6): p. 2575-2581.

91. Kurita, D., et al., *Carrier generation and transport properties of heavily Nb-doped anatase TiO2 epitaxial films at high temperatures.* Journal of Applied Physics, 2006. **100**(9).

92. Yan, Y. and S.H. Wei, *Doping asymmetry in wide-bandgap semiconductors: Origins and solutions.* Physica Status Solidi B-Basic Solid State Physics, 2008. **245**(4): p. 641-652.

93. Nguyen, V.L., B.Z. Spivak, and B.I. Shklovskii, *Aaronov-Bohm Oscillations with Normal and Superconducting Flux Quanta in Hopping Conductivity.* Jetp Letters, 1985. **41**(1): p. 42-45.

94. Sivan, U., O. Entinwohlman, and Y. Imry, *Orbital Magnetoconductance in the Variable-Range-Hopping Regime.* Physical Review Letters, 1988. **60**(15): p. 1566-1569.

95. Faran, O. and Z. Ovadyahu, *Magnetoconductance in the Variable-Range-Hopping Regime Due to a Quantum-Interference Mechanism.* Physical Review B, 1988. **38**(8): p. 5457-5465.

96. Essaleh, L., S.M. Wasim, and J. Galibert, *Effect of impurity band conduction on the electrical characteristics of n-type CuInSe2.* Journal of Applied Physics, 2001. **90**(8): p. 3993-3997.

97. Tauc, J., *Optical Properties and Electronic Structure of Amorphous.* Materials Research Bulletin, 1968. **3**(1): p. 37-&.

98. Burstein, E., *Anomalous Optical Absorption Limit in Insb.* Physical Review, 1954. **93**(3): p. 632-633.

99. Moss, T.S., *The Interpretation of the Properties of Indium Antimonide.* Proceedings of the Physical Society of London Section B, 1954. **67**(418): p. 775-782.

100. Bard, A.J., et al., *The Concept of Fermi Level Pinning at Semiconductor-Liquid Junctions - Consequences for Energy-Conversion Efficiency and Selection of Useful Solution Redox Couples in Solar Devices.* Journal of the American Chemical Society, 1980. **102**(11): p. 3671-3677.

101. Cardon, F. and W.P. Gomes, *Determination of Flat-Band Potential of a Semiconductor in Contact with a Metal or an Electrolyte from Mott-Schottky Plot.* Journal of Physics D-Applied Physics, 1978. **11**(4): p. L63-L67.

102. Sukhotin, A.M., M.S. Grilikhes, and E.V. Lisovaya, *The Influence of Passivation on the Kinetics of the Dissolution of Iron .1. Outer Layer of the Passivating Film as a Heavy Doped Thin Semiconductor and Mott-Schottky Equation.* Electrochimica Acta, 1989. **34**(2): p. 109-112.

103. Mayer, M., *Ion beam analysis of rough thin films.* Nuclear Instruments and Methods in Physics Research Section B: Beam Interactions with Materials and Atoms, 2002. **194**(2): p. 177-186.

104. Bisquert, J., et al., *Anomalous transport effects in the impedance of porous film electrodes.* Electrochemistry Communications, 1999. **1**(9): p. 429-435.

105. Bisquert, J., *Influence of the boundaries in the impedance of porous film electrodes.* Physical Chemistry Chemical Physics, 2000. **2**(18): p. 4185-4192.

106. Hsu, C.H. and F. Mansfeld, *Technical note: Concerning the conversion of the constant phase element parameter Y-0 into a capacitance.* Corrosion, 2001. **57**(9): p. 747-748.

107. Hassanzadeh, A., M.H. Habibi, and A. Zeini-Isfahani, *Study of electronic structure of tin-doped In2O3 (ITO) film deposited on glass.* Acta Chimica Slovenica, 2004. **51**(3): p. 507-527.

108. Eucken, A. and A. Buchner, *The dielectrical constants of weak polar crystals and their dependency on temperature.* Zeitschrift Fur Physikalische Chemie-Abteilung B-Chemie Der Elementarprozesse Aufbau Der Materie, 1934. **27**(5/6): p. 321-349.

109. Roberts, S., *Dielectric Constants and Polarizabilities of Ions in Simple Crystals and Barium Titanate.* Physical Review, 1949. **76**(8): p. 1215-1220.

110.Kresse, G. and J. Hafner, *Ab-Initio Molecular-Dynamics Simulation of the Liquid-Metal Amorphous-Semiconductor Transition in Germanium.* Physical Review B, 1994. **49**(20): p. 14251-14269.

111.Kresse, G. and J. Furthmuller, *Efficient iterative schemes for ab initio total-energy calculations using a plane-wave basis set.* Physical Review B, 1996. **54**(16): p. 11169-11186.

112.Perdew, J.P., et al., *Atoms, Molecules, Solids, and Surfaces - Applications of the Generalized Gradient Approximation for Exchange and Correlation.* Physical Review B, 1992. **46**(11): p. 6671-6687.

113.Blochl, P.E., *Projector Augmented-Wave Method.* Physical Review B, 1994. **50**(24): p. 17953-17979.

114.Imada, M., A. Fujimori, and Y. Tokura, *Metal-insulator transitions.* Reviews of Modern Physics, 1998. **70**(4): p. 1039-1263.

115.Muraoka, Y. and Z. Hiroi, *Metal-insulator transition of VO2 thin films grown on TiO2 (001) and (110) substrates.* Applied Physics Letters, 2002. **80**(4): p. 583-585.

116.Kondo, J., *Resistance Minimum in Dilute Magnetic Alloys.* Progress of Theoretical Physics, 1964. **32**(1): p. 37-&.

117.Bergmann, G., *Weak Localization in Thin-Films - a Time-of-Flight Experiment with Conduction Electrons.* Physics Reports-Review Section of Physics Letters, 1984. **107**(1): p. 1-58.

118.Taylor, P.L. and O. Heinonen, *A Quantum Approach to Condensed Matter Physics*. 2002, Cambridge: Cambridge U. P.

119.Kouwenhoven, L. and L. Glazman, *Revival of the Kondo effect.* Physics World, 2001. **14**(1): p. 33-38.

120. Goldhaber-Gordon, D., et al., *From the Kondo regime to the mixed-valence regime in a single-electron transistor.* Physical Review Letters, 1998. **81**(23): p. 5225-5228.

121. Nozieres, P., *Fermi-Liquid Description of Kondo Problem at Low Temperatures.* Journal of Low Temperature Physics, 1974. **17**(1-2): p. 31-42.

122. Sekitani, T., M. Naito, and N. Miura, *Kondo effect in underdoped n-type superconductors.* Physical Review B, 2003. **67**(17).

123. Shon, N.H. and H.N. Nazareno, *Influence of Quantum-Interference Effects on Hole Mobility in Superlattices.* Physical Review B, 1994. **50**(12): p. 8577-8583.

124. Datta, S., *Electronic Transport in Mesoscopic Systems*. 1995, Cambridge: Cambridge U. P.

125. Kramer, B. and A. Mackinnon, *Localization - Theory and Experiment.* Reports on Progress in Physics, 1993. **56**(12): p. 1469-1564.

126. Galperin, Y.M., *"Quantum Transport" Lecture Notes*. 1998: Lund University.

127. Zhang, S.X., et al., *Electronic Manifestation of Cation-Vacancy-Induced Magnetic Moments in a Transparent Oxide Semiconductor: Anatase Nb:TiO2.* Advanced Materials, 2009. **21**(22): p. 2282-+.

128. Li, G.X., et al., *Spin valve sensors for ultrasensitive detection of superparamagnetic nanoparticles for biological applications.* Sensors and Actuators a-Physical, 2006. **126**(1): p. 98-106.

129. Freitas, P.P., et al., *Magnetoresistive sensors.* Journal of Physics-Condensed Matter, 2007. **19**(16).

130. Ohno, H., *Making nonmagnetic semiconductors ferromagnetic.* Science, 1998. **281**(5379): p. 951-956.

131. Jungwirth, T., Q. Niu, and A.H. MacDonald, *Anomalous Hall effect in ferromagnetic semiconductors.* Physical Review Letters, 2002. **88**(20).

132. Ogale, S.B., *Dilute Doping, Defects, and Ferromagnetism in Metal Oxide Systems.* Advanced Materials, 2010. **22**(29): p. 3125-3155.

133. Ruderman, M.A. and C. Kittel, *Indirect Exchange Coupling of Nuclear Magnetic Moments by Conduction Electrons.* Physical Review, 1954. **96**(1): p. 99-102.

134. Kasuya, T., *A Theory of Metallic Ferromagnetism and Antiferromagnetism on Zeners Model.* Progress of Theoretical Physics, 1956. **16**(1): p. 45-57.

135. Yosida, K., *Magnetic Properties of Cu-Mn Alloys.* Physical Review, 1957. **106**(5): p. 893-898.

136. Kaminski, A. and S. Das Sarma, *Polaron percolation in diluted magnetic semiconductors.* Physical Review Letters, 2002. **88**(24).

137. Calderon, M.J. and S.D. Sarma, *Theory of carrier mediated ferromagnetism in dilute magnetic oxides.* Annals of Physics, 2007. **322**(11): p. 2618-2634.

138. Watson, L.R., et al., *High-Temperature Mass-Spectrometric Studies of the Bond-Energies of Gas-Phase Zno, Nio, and Cuo.* Journal of Physical Chemistry, 1993. **97**(21): p. 5577-5580.

139. De Buysser, K., et al., *Study of negative thermal expansion and shift in phase transition temperature in Ti4+- and Sn4+-substituted ZrW2O8 materials.* Inorganic Chemistry, 2008. **47**(2): p. 736-741.

140. Kirkpatr.S, *Percolation and Conduction.* Reviews of Modern Physics, 1973. **45**(4): p. 574-588.

141. Wang, J.Q., Z.D. Zhao, and S.L. Whittenburg, *Thickness dependence of magnetic blocking in granular thin films with interacting magnetic particles.* Journal of Applied Physics, 2003. **93**(11): p. 9208-9211.

142. Zhou, S.Q., et al., *Crystallographically oriented Fe nanocrystals formed in Fe-implanted TiO(2).* Journal of Applied Physics, 2008. **103**(8).

143. Skumryev, V., et al., *Beating the superparamagnetic limit with exchange bias.* Nature, 2003. **423**(6942): p. 850-853.

144. Yuan, C.L., *Room-Temperature Coercivity of Ni/NiO Core/Shell Nanoparticles Fabricated by Pulsed Laser Deposition.* Journal of Physical Chemistry C, 2010. **114**(5): p. 2124-2126.

145. Ding, B.F., Y.P. Li, and L.M. Wang, *Structural and Magnetic Properties of Ni-Implanted Rutile Single Crystals.* Chinese Physics Letters, 2011. **28**(10).

146. Wunderlich, W., H. Ohta, and K. Koumoto, *Enhanced effective mass in doped SrTiO3 and related perovskites.* Physica B-Condensed Matter, 2009. **404**(16): p. 2202-2212.

147. Shein, I.R., V.L. Kozhevnikov, and A. Ivanovskii, *First-principles calculations of the elastic and electronic properties of the cubic perovskites SrMO3 (M = Ti, V, Zr and Nb) in comparison with SrSnO3.* Solid State Sciences, 2008. **10**(2): p. 217-225.

148. Peng, N.H., J.T.S. Irvine, and A.G. Fitzgerald, *Synthesis and crystal structure of the distorted perovskite Sr0.97NbO3 determined by high resolution powder neutron diffraction.* Journal of Materials Chemistry, 1998. **8**(4): p. 1033-1038.

149. Ridgley, D. and R. Ward, *The Preparation of a Strontium-Niobium Bronze with the Perovskite Structure.* Journal of the American Chemical Society, 1955. **77**(23): p. 6132-6136.

150. Hessen, B., et al., *Crystallization of Reduced Strontium and Barium Niobate Perovskites from Borate Fluxes.* Materials Research Bulletin, 1991. **26**(1): p. 85-90.

151. Nguyen, N., J. Choisnet, and B. Raveau, *New Niobium Bronzes with Tetragonal Structure.* Comptes Rendus Hebdomadaires Des Seances De L Academie Des Sciences Serie C, 1976. **282**(6): p. 303-306.

152. Tomio, T., et al., *Control of Electrical-Conductivity in Laser-Deposited Srtio3 Thin-Films with Nb Doping.* Journal of Applied Physics, 1994. **76**(10): p. 5886-5890.

153. Takeno, S., et al., *Novel compositional accommodation mechanism in SrNbO3 epitaxial thin films revealed by analytical electron microscopy.* Surface and Interface Analysis, 2003. **35**(1): p. 29-35.

154. Balasubramaniam, K.R., et al., *Phase and structural characterization of Sr2Nb2O7 and SrNbO3 thin films grown via pulsed laser ablation in O-2 or N-2 atmospheres.* Journal of Solid State Chemistry, 2008. **181**(4): p. 705-714.

155. Kalabukhov, A., et al., *Effect of oxygen vacancies in the SrTiO3 substrate on the electrical properties of the LaAlO3/SrTiO3 interface.* Physical Review B, 2007. **75**(12).

156. Turzhevsky, S.A., et al., *Electronic-Structure and Crystal-Chemistry of Niobium Oxide Phases.* Physical Review B, 1994. **50**(5): p. 3200-3208.

157. Isawa, K., et al., *Photoelectron Spectroscopic Study of Srxnbo3.* Physical Review B, 1994. **49**(5): p. 3534-3538.

158. Pan, H.C., C.C. Chou, and H.L. Tsai, *Low-temperature processing of sol-gel derived La0.5Sr0.5MnO3 buffer electrode and PbZr0.52Ti0.48O3 films using CO2 laser annealing.* Applied Physics Letters, 2003. **83**(15): p. 3156-3158.

159. Tiwari, A., et al., *Rectifying electrical characteristics of La0.7Sr0.3MnO3/ZnO heterostructure.* Applied Physics Letters, 2003. **83**(9): p. 1773-1775.

160. C. D. Wagner, et al., *Handbook of X-Ray Photoelectron Spectroscopy*. 1979, Eden Prairie, MN: Perkin-Elmer.

161. Sasaki, J., N.L. Peterson, and K. Hoshino, *Tracer Impurity Diffusion in Single-Crystal Rutile (Tio2-X).* Journal of Physics and Chemistry of Solids, 1985. **46**(11): p. 1267-1283.

## Appendices

### Appendix 1 Derivation of equation (3.7) from equation (3.6)

$$\rho = \rho_0 \cdot exp\left[\left(\frac{T_0}{T}\right)^v\right]$$

$$w(T) = -\frac{dln\rho}{dlnT} = -\frac{dln\rho}{d\rho} \cdot \frac{d\rho}{dT} \cdot \frac{dT}{dlnT}$$

$$\frac{dln\rho}{d\rho} = \frac{1}{\rho}$$

$$\frac{d\rho}{dT} = \frac{d\left\{\rho_0 \cdot exp\left[\left(\frac{T_0}{T}\right)^v\right]\right\}}{dT} = \rho_0 \cdot exp\left[\left(\frac{T_0}{T}\right)^v\right] \cdot (-v) \cdot \frac{1}{T} \cdot \left(\frac{T_0}{T}\right)^v$$

$$= \rho \cdot (-v) \cdot \frac{1}{T} \cdot \left(\frac{T_0}{T}\right)^v$$

$$\frac{dT}{dlnT} = T$$

$$w(T) = -\frac{dln\rho}{d\rho} \cdot \frac{d\rho}{dT} \cdot \frac{dT}{dlnT} = \frac{1}{\rho} \cdot \rho \cdot (-v) \cdot \frac{1}{T} \cdot \left(\frac{T_0}{T}\right)^v \cdot T = v \cdot \left(\frac{T_0}{T}\right)^v$$

Then the value of $v$ can be obtained as:

$$\frac{dln[w(T)]}{dlnT} = \frac{dln[w(T)]}{dT} \cdot \frac{dT}{dlnT} = \frac{1}{w(T)} \cdot v \cdot \left(\frac{T_0}{T}\right)^v \cdot (-v) \cdot \frac{1}{T} \cdot T = -v$$

### Appendix 2 Values of the constants in equation (3.8)

$$\rho = A \cdot T^5 + B \cdot T + C \cdot \exp\left[\left(\frac{T_0}{T}\right)^{1/4}\right] + D$$

$A = 1.815 \times 10^{-9}$

$B = 16.8$

$C = 958.563$

$D = 2.041 \times 10^{-3}$

$T_0 = 4582.397$

## Appendix 3 Fitting details of Figure 3.5 (a)

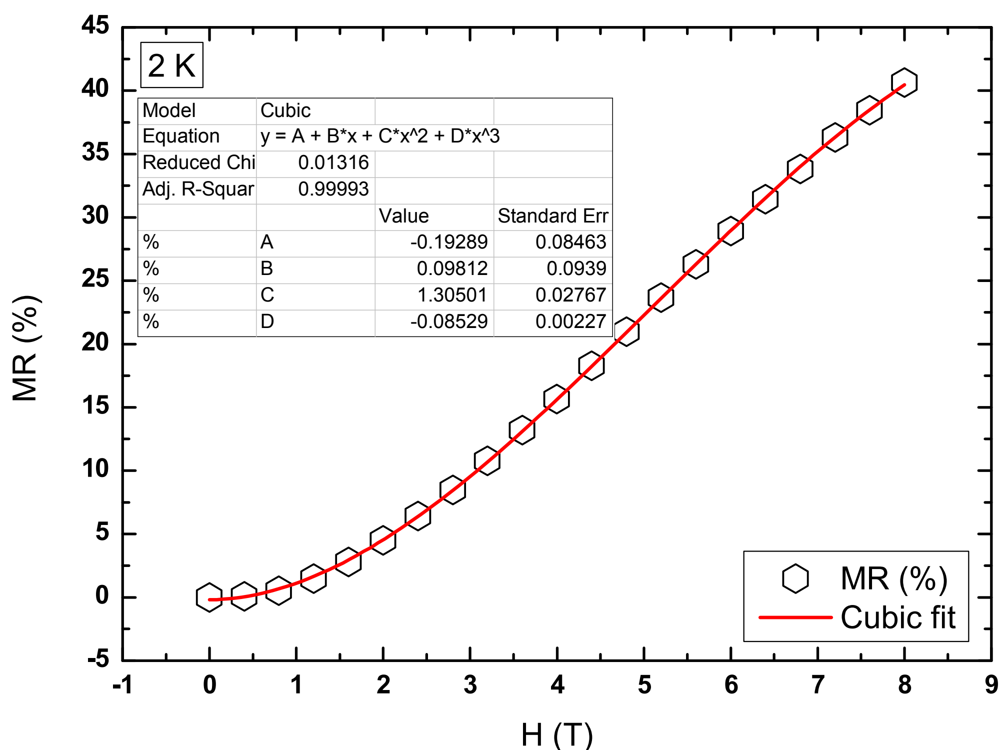


**AppFig 3.1: Cubic polynomial fitting of the MR at 2 K.**

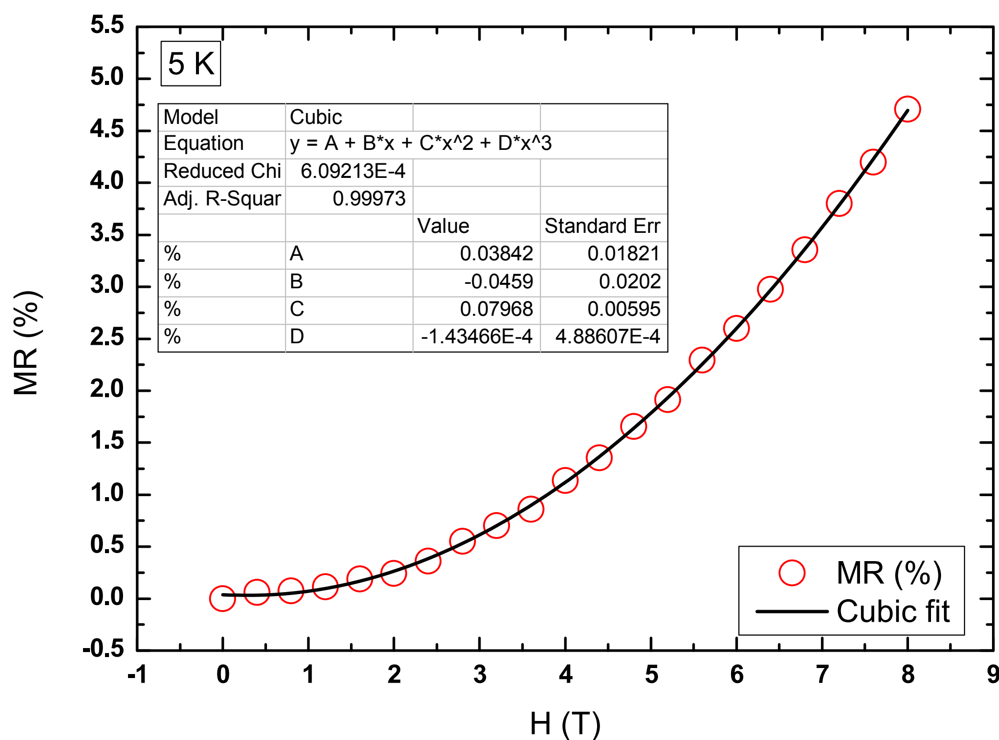


**AppFig 3.2: Cubic polynomial fitting of the MR at 5 K.**

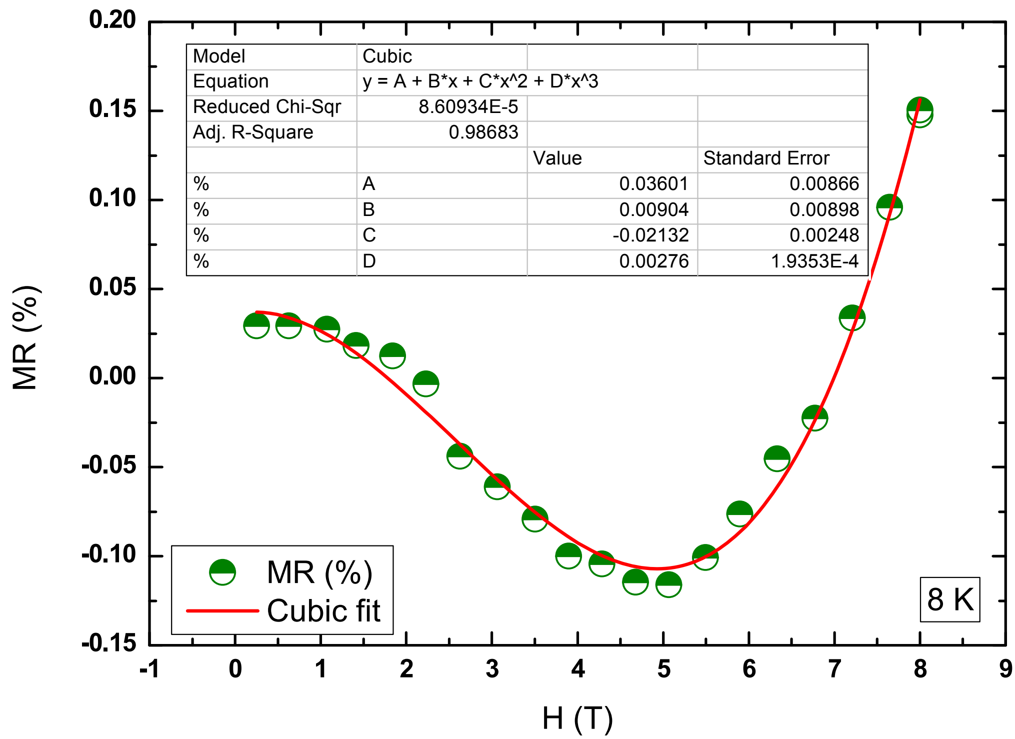


**AppFig 3.3: Cubic polynomial fitting of the MR at 8 K.**

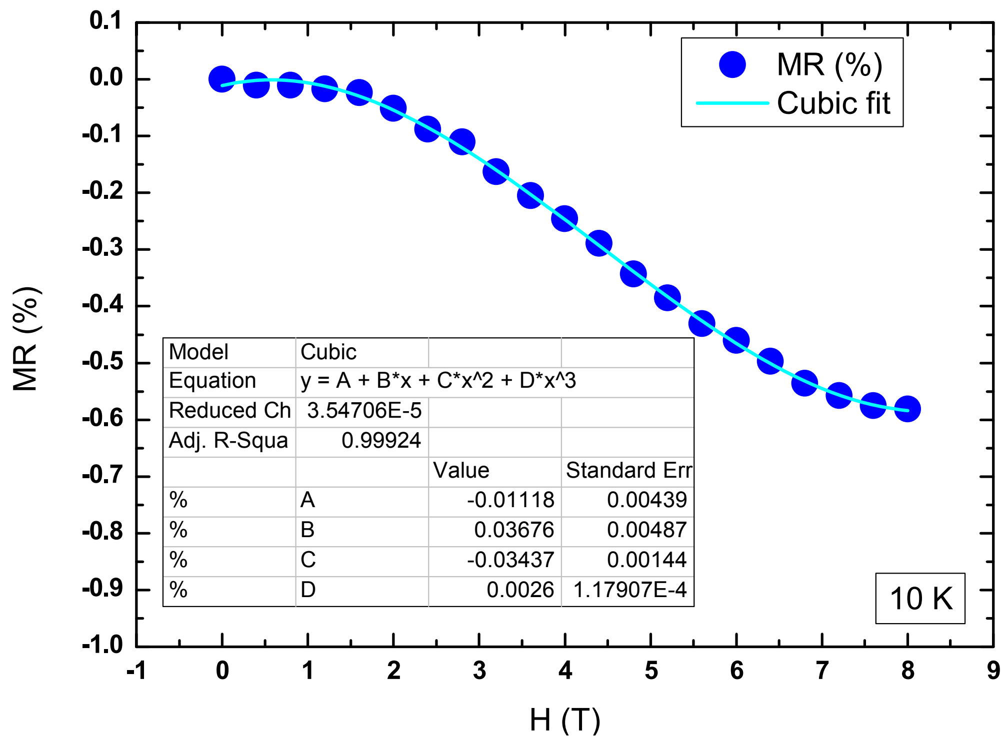


**AppFig 3.4: Cubic polynomial fitting of the MR at 10 K.**

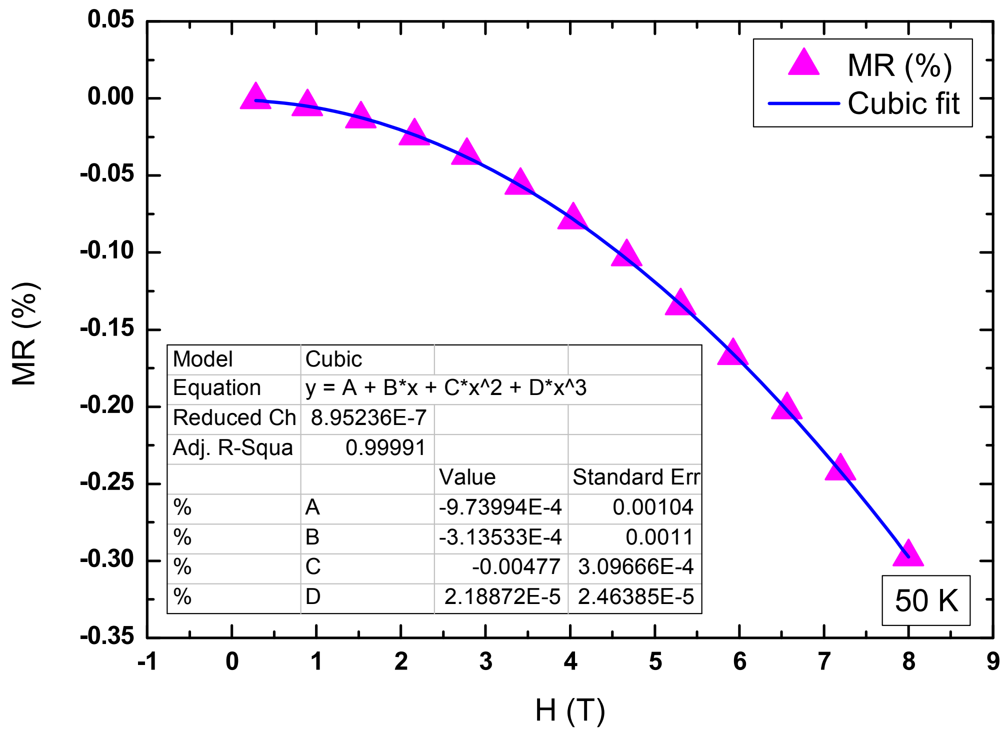


**AppFig 3.5: Cubic polynomial fitting of the MR at 50 K.**

Cubic polynomial is the minimum order for simulating all the five curves. Some of them are been fitted by lower order, e.g. MR at 5 K and 50 K are been fitted by quadratic equation.

**Appendix 4 The impedance spectra of 3.5%, 6.4% and 8.9% Ta-$TiO_2$ films**

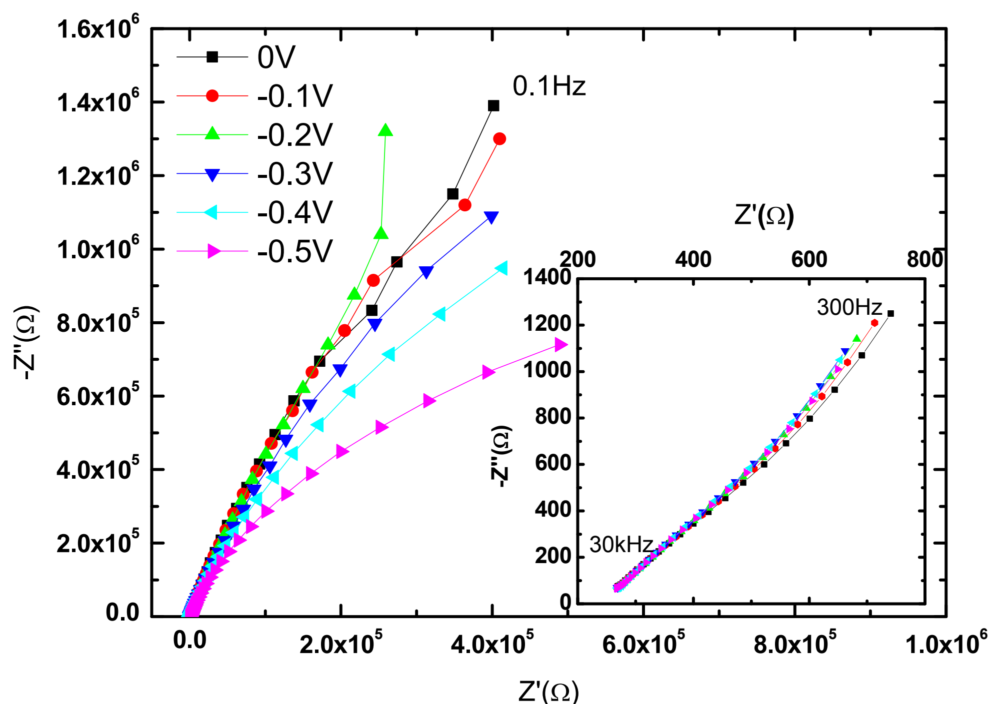


**AppFig 4.1: Nyquist plots of 3.5% Ta incorporated $TiO_2$ without Al buffer contact layer. The frequency range shown here is from 0.1 Hz to 30 kHz. The inset graph is the expanded scale of the high frequency data.**

Comparing with the spectra of 1.5% Ta-$TiO_2$, the semi-circle at high frequency in the plot here becomes less obvious. When the sample becomes more conductive, the fluctuation of the impedance spectroscopy becomes more significant, which introduces more error to the experiment. Anyhow, by repeating the measurement many times, acceptable data still can be obtained.

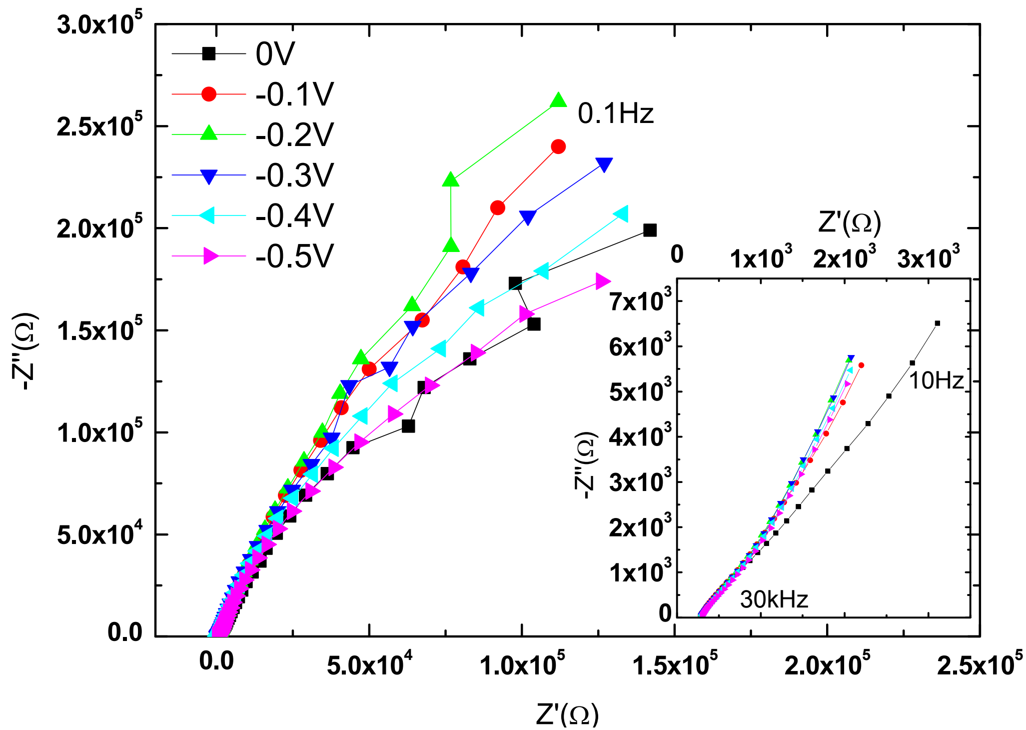


**AppFig 4.2: Nyquist plots of 6.4% Ta incorporated $TiO_2$ without Al buffer contact layer. The frequency range shown here is from 0.1 Hz to 30 kHz. The inset graph is the expanded scale of the high frequency data.**

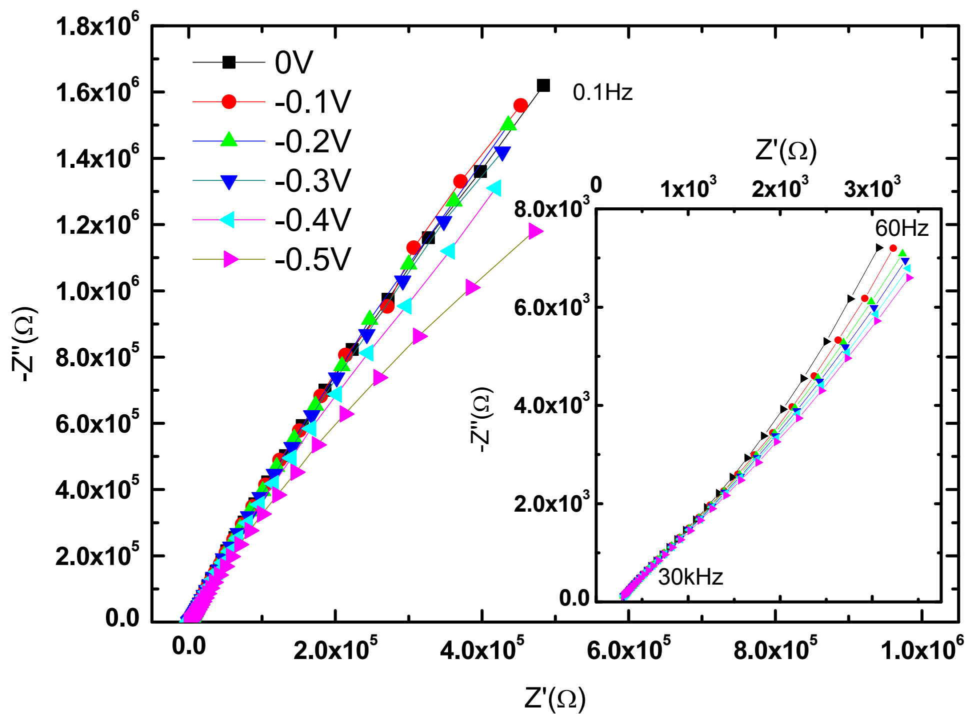


**AppFig 4.3: Nyquist plots of 8.9% Ta incorporated $TiO_2$ without Al buffer contact layer. The frequency range shown here is from 0.1 Hz to 30 kHz. The inset graph is the expanded scale of the high frequency data.**

**Appendix 5 Zeview fitting parameters of R, R’, $T_{CPE}$, $P_{CPE}$, $\omega''_{max}$ for the equivalent circuit in Fig.4.6 (c)**

| | Voltage(V) | R(Ω) | R'(Ω) | $T_{CPE}$ | $P_{CPE}$ | $\omega''_{max}$ |
|---|---|---|---|---|---|---|
| Pure $TiO_2$ | 0 | 3.67E+06 | 6.76E+07 | 5.59E-08 | 0.92 | 0.030 |
| | -0.1 | 3.21E+06 | 8.19E+07 | 5.90E-08 | 0.91 | 0.030 |
| | -0.2 | 3.07E+06 | 8.79E+07 | 6.16E-08 | 0.91 | 0.030 |
| | -0.3 | 2.91E+06 | 8.96E+07 | 6.49E-08 | 0.91 | 0.030 |
| | -0.4 | 2.82E+06 | 8.05E+07 | 6.76E-08 | 0.90 | 0.030 |
| | -0.5 | 2.71E+06 | 8.59E+07 | 7.13E-08 | 0.90 | 0.030 |
| 1.5% Ta-$TiO_2$ | 0 | 1.32E+03 | 1.34E+07 | 5.06E-07 | 0.92 | 0.010 |
| | -0.1 | 1.27E+03 | 1.42E+07 | 5.00E-07 | 0.91 | 0.010 |
| | -0.2 | 1.50E+03 | 1.32E+07 | 4.93E-07 | 0.90 | 0.010 |
| | -0.3 | 1.43E+03 | 1.28E+07 | 5.05E-07 | 0.89 | 0.010 |
| | -0.4 | 1.13E+03 | 1.22E+07 | 5.42E-07 | 0.89 | 0.010 |
| | -0.5 | 1.10E+03 | 6.37E+06 | 5.68E-07 | 0.89 | 0.010 |
| 3.5% Ta-$TiO_2$ | 0 | 2.57E+02 | 6.67E+06 | 5.93E-07 | 0.92 | 0.006 |
| | -0.1 | 2.88E+02 | 6.41E+06 | 5.94E-07 | 0.92 | 0.006 |
| | -0.2 | 3.01E+02 | 6.86E+06 | 6.07E-07 | 0.92 | 0.006 |
| | -0.3 | 2.88E+02 | 4.06E+06 | 6.16E-07 | 0.91 | 0.006 |
| | -0.4 | 2.77E+02 | 3.86E+06 | 6.28E-07 | 0.90 | 0.006 |
| | -0.5 | 2.59E+02 | 2.68E+06 | 6.58E-07 | 0.90 | 0.006 |
| 6.4% Ta-$TiO_2$ | 0 | 1.42E+02 | 4.05E+05 | 7.41E-07 | 0.93 | 0.005 |
| | -0.1 | 1.18E+02 | 7.69E+05 | 7.14E-07 | 0.92 | 0.005 |
| | -0.2 | 1.13E+02 | 7.97E+05 | 7.12E-07 | 0.91 | 0.005 |
| | -0.3 | 1.17E+02 | 6.70E+05 | 7.21E-07 | 0.90 | 0.005 |
| | -0.4 | 1.15E+02 | 5.65E+05 | 7.50E-07 | 0.90 | 0.005 |
| | -0.5 | 1.10E+02 | 4.49E+05 | 8.02E-07 | 0.90 | 0.005 |
| 8.9% Ta-$TiO_2$ | 0 | 2.35E+02 | 9.89E+06 | 6.27E-07 | 0.87 | 0.006 |
| | -0.1 | 2.23E+02 | 9.72E+06 | 5.73E-07 | 0.86 | 0.006 |
| | -0.2 | 1.68E+02 | 9.82E+06 | 6.21E-07 | 0.87 | 0.006 |
| | -0.3 | 1.45E+02 | 9.57E+06 | 6.50E-07 | 0.87 | 0.006 |
| | -0.4 | 1.24E+02 | 8.38E+06 | 6.17E-07 | 0.85 | 0.006 |
| | -0.5 | 1.05E+02 | 5.93E+06 | 6.28E-07 | 0.85 | 0.006 |

**Appendix 6 Transport and optical properties of $Ta_xTi_{1-x}O_2$ films with Ta concentration (x) between 20% and 30%**

Ta incorporated $TiO_2$ films with Ta concentration between 20% and 30% were prepared to investigate the maximum Ta concentration that anatase $TiO_2$ lattice can sustain. Ta incorporated $TiO_2$ films in anatase phase with Ta concentration 20% and 25% are metallic in the measurement temperature range of 2 K to 300 K. However, when Ta concentration was increased to 30%, the resistivity and charge carrier density of the film show semiconducting behavior at low temperatures. The optical bandgap of the films keeps increasing with Ta concentration, until which reaching 25%, it becomes saturating. Hence 25% is concluded as the maximum concentration that Ta can exist in anatase $TiO_2$ crystal lattice.

$Ta_xTi_{1-x}O_2$ films ($x$ = 0.2, 0.25 and 0.3, which are the nominal concentrations of Ta in the targets) were prepared by PLD with the setup same as described in chapter 3. The base pressure was kept at $5\times10^{-7}$ Torr. The films were prepared at 700°C under oxygen partial pressure of $1.4 \times 10^{-5}$ Torr. The laser energy density was 2 J/cm$^2$ and 5 Hz was used as its frequency. The thickness of the films was measured as around 100 nm, which took half an hour deposition. The crystal structure of the films is measured as anatase form, which is same as in Fig. 3.1. When Ta concentration exceeds 30%, it is difficult to obtain single phase of anatase $TiO_2$ film.

Temperature dependent resistivity and the corresponding charge carrier density and mobility of the samples were measured and shown in AppFig 6.1. The films with Ta concentration of 20% and 25% show entirely metallic behavior in the measurement temperature range (AppFig 6.1(a)). In contrast, the film with Ta concentration of 30% shows a resistivity minimum near 60 K, which indicates a semiconducting behavior below this temperature. The resistivity at the same temperature keeps increasing with Ta concentration, which follows the argument about the existence of an optimum Ta concentration (6.4% in Fig. 4.5) that makes the anatase $TiO_2$ film most conductive. The resistivity of the film with 30% of Ta shows logarithmic temperature dependence below 60 K, which suggests weak localization as the mechanism. The mobility (AppFig 6.1(b)) of all three films decreases with

increasing temperature, which is due to the enhanced electron-phonon scattering at higher temperature. However, the charge carrier density (*n* type) of the films with Ta concentration of 20% and 25% deviates from normal metallic system where it should be independent of temperature. I have limited knowledge to understand this deviation. Below 60 K, charge carrier density changes with temperature in different manners for the films with different Ta concentrations: for the film with 20% of Ta, charge carrier density decreases with temperature; for the film with 25% of Ta, charge carrier density is independent of temperature; and for the film with 30% of Ta, charge carrier density increases with temperature. Hence 25% of Ta is a boundary to separate the temperature dependent charge carrier density of the films below 60 K.

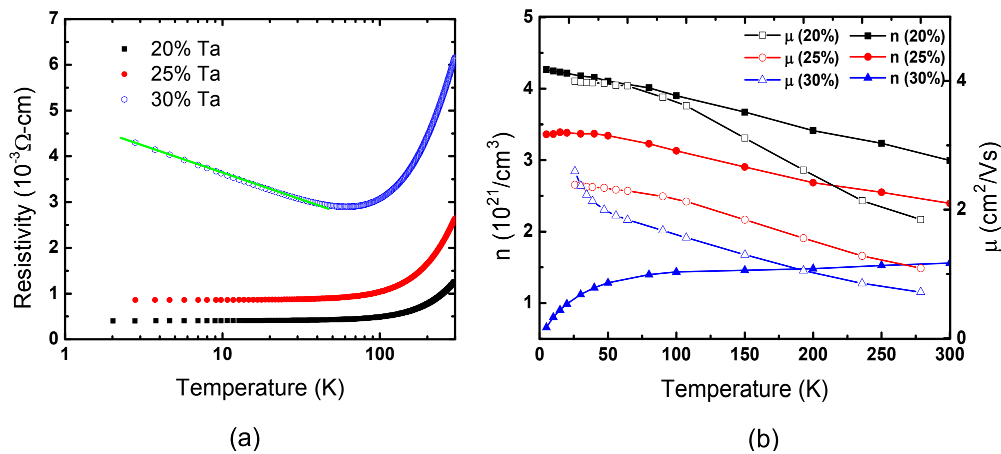


**AppFig 6.1: (a) Temperature dependent resistivity of Ta-$TiO_2$ films with different Ta concentrations. (b) Temperature dependent charge carrier density (left axis) and mobility (right axis) of the films in (a).**

The transmission and the corresponding Tauc plots for obtaining the optical bandgaps of the films are shown in AppFig 6.2. The absorption edge (AppFig 6.2(a)) near 300 nm shows a slightly shift with Ta concentration. The corresponding Tauc plots (AppFig 6.2(b)) indicate a blue shift of optical bandgap of Ta-$TiO_2$ films with Ta concentration. The optical bandgap keeps increasing with Ta concentration until 25%, after which, it starts to saturate. The maximum optical bandgap of Ta incorporated $TiO_2$ films in anatase phase is around 3.55 eV, which is around 0.2 eV larger than that of pure anatase $TiO_2$ film. We have discussed the shift of the bandgap edges with Ta incorporation in chapter 4. As that shift is related to the blue shift of the optical bandgap, it is interesting to know how much the conduction band edge has been pushed

toward vacuum level with Ta concentration of 25%. It may have important applications in photocatalytic experiments like water splitting and $CO_2$ reduction. Hence it will be investigated in details in future.

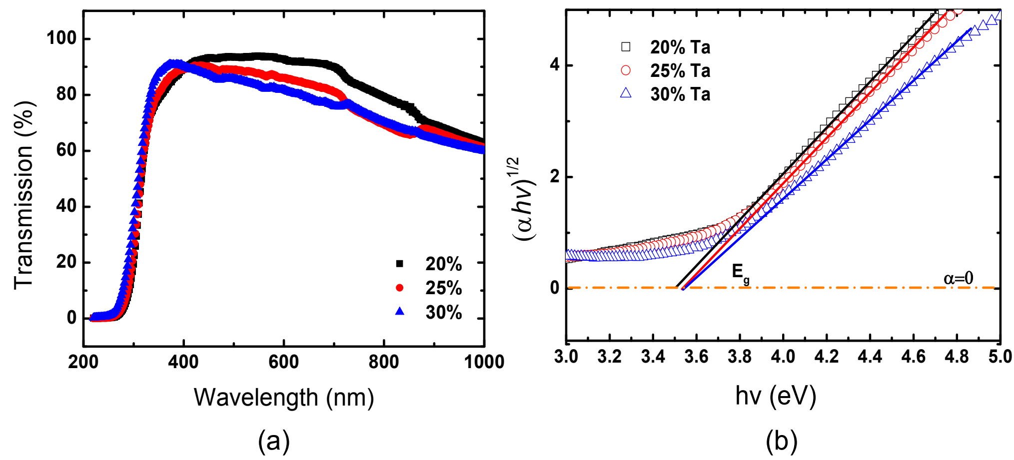


**AppFig 6.2: (a) Transmission of Ta incorporated $TiO_2$ films in anatase phase with Ta concentrations of 20%, 25% and 30%. (b) The corresponding Tauc plot of the films in (a). Indirect bandgap model is applied in Tauc plot.**

**Appendix 7 Transmittance spectrum of (001) $TiO_2$ substrate treated under different conditions**

The absorption edge of the sample treated under different conditions locates at the same wavelength, corresponding to the bandgap of 3.0 eV. The continuous drop of the transmittance above 500 nm for the vacuum annealed sample is related to the free electron excitations (Drude model), which is discussed as mainly coming from ionized nickel impurities. For the sample subsequently anealed in air after in vacuum, the transimittance curve between 410 nm and 600 nm is shallower comparing with the as received sample. This may be the result of the silver paste at the backside as it is tough to be removed completely when the sample is annealed in air with high temperature.

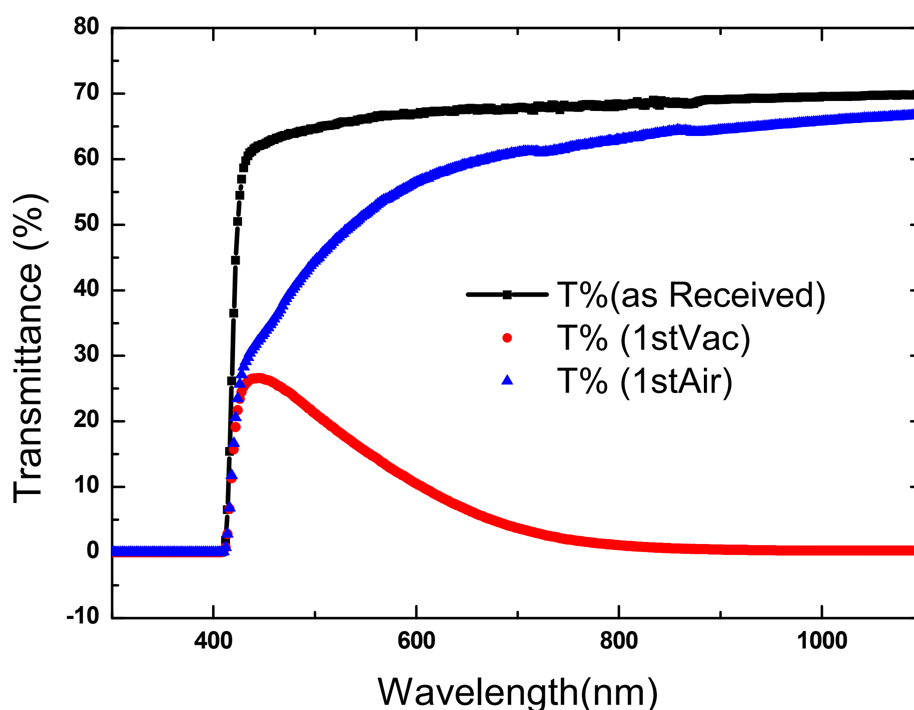


**AppFig 7: Transmittance spectrum of (001) $TiO_2$ substrate treated under different conditions: as received (black); annealed in vacuum ($5\times10^{-6}$ Torr) with 800 °C (red) for 4 hours; and subsequently annealed in air with 800 °C (blue) for 2 hours.**

**Appendix 8 Comparison the magnetic property of $TiO_2$ substrates with (001) and (110) orientations annealed in the same vacuum condition**

Two pieces of $TiO_2$ substrates with (001) and (110) orientations are attached side by side onto the heater and annealed in vacuum ($5\times10^{-6}$ Torr) with 800 °C for 2 hours. Obviously, at the same measurement temperature, the magnetic loop of the (001) surface is broader than the one of the (110) surface, which is due to the easier diffusion of nickel impurity in the former case [161]. The annealing temperature and time dependent of the ferromagnetism of $TiO_2$ substrate with (110) orientation is just similar as the one with (001) orientation.

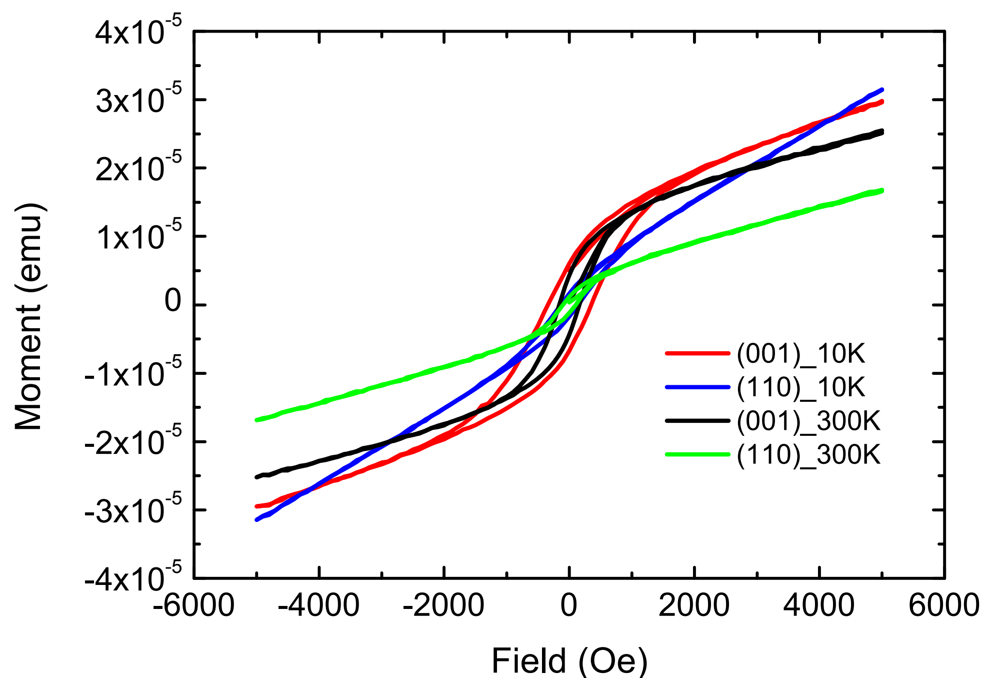


**AppFig 8: Magnetic moment versus field (MH) measurement of $TiO_2$ substrate with different orientations. The annealing temperature is 800°C and the annealing time is 2hours.**